DISSERTATION

PLASMA FLOW FIELD MEASUREMENTS DOWNSTREAM

OF A HOLLOW CATHODE

Submitted by

Casey Coffman Farnell

Department of Mechanical Engineering

In partial fulfillment of the requirements

For the Degree of Doctor of Philosophy

Colorado State University

Fort Collins, Colorado

Fall 2007

UMI Number: 3299754

INFORMATION TO USERS

The quality of this reproduction is dependent upon the quality of the copy submitted. Broken or indistinct print, colored or poor quality illustrations and photographs, print bleed-through, substandard margins, and improper alignment can adversely affect reproduction.

In the unlikely event that the author did not send a complete manuscript and there are missing pages, these will be noted. Also, if unauthorized copyright material had to be removed, a note will indicate the deletion.

UMI®

UMI Microform 3299754
Copyright 2008 by ProQuest LLC.
All rights reserved. This microform edition is protected against unauthorized copying under Title 17, United States Code.

COLORADO STATE UNIVERSITY

October 29, 2007

WE HEREBY RECOMMEND THAT THE DISSERTATION PREPARED UNDER OUR SUPERVISION BY CASEY C. FARNELL ENTITLED PLASMA FLOW FIELD MEASUREMENTS DOWNSTREAM OF A HOLLOW CATHODE BE ACCEPTED AS FULFILLING IN PART REQUIREMENTS FOR THE DEGREE OF DOCTOR OF PHILOSOPHY.

Committee on Graduate Work

_____
John D. Williams – Adviser
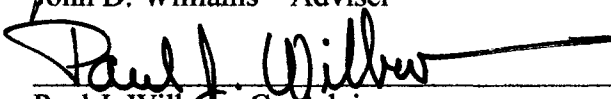
_____
Paul J. Wilbur – Co-Adviser
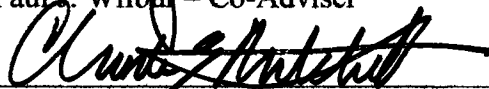
_____
Charles E. Mitchell
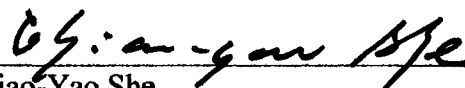
_____
Chiao-Yao She
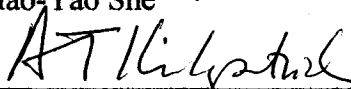
_____
Allan T. Kirkpatrick – Department Head

ii

ABSTRACT OF DISSERTATION

PLASMA FLOW FIELD MEASUREMENTS DOWNSTREAM

OF A HOLLOW CATHODE

The focus of the research described herein is to investigate and characterize the plasma produced downstream of a hollow cathode with the goal of identifying groups of ions and possible mechanisms of their formation within a plasma discharge that might cause erosion, especially with respect to the hollow cathode assembly. In space applications, hollow cathodes are used in electrostatic propulsion devices, especially in ion thrusters and Hall thrusters, to provide electrons to sustain the plasma discharge and neutralize the ion beam. This research is considered important based upon previous thruster life tests that have found erosion occurring on hollow cathode, keeper, and ion optics surfaces exposed to the discharge plasma. This erosion has the potential to limit the life of the thruster, especially during ambitious missions that require ultra long periods of thruster operation.

Results are presented from two discharge chamber configurations that produced very different plasma environments. Four types of diagnostics are described that were used to probe the plasma including an emissive probe, a triple Langmuir probe, a remotely located electrostatic analyzer (ESA), and an ExB probe attached to the ESA. In addition, a simulation model was created that correlates the measurements from the direct and remotely located probes.

Casey C. Farnell
Department of Mechanical Engineering
Colorado State University
Fort Collins, CO 80523
Fall 2007

iii

ACKNOWLEDGEMENTS

I would like to thank my principle advisors, Dr. Paul Wilbur and Dr. John Williams, for sharing their expertise, leadership, and encouragement to reach this point in my research. I would also like to thank my family and friends for their positive and continual support.

TABLE OF CONTENTS

1

1 Introduction

1.1 Research Goal

In space applications, hollow cathodes are used in electrostatic propulsion devices, especially in ion thrusters and Hall thrusters, to provide electrons to sustain the plasma discharge and neutralize the ion beam. Hollow cathodes can also be used as plasma contactors on spacecraft to manage spacecraft charging. In addition, hollow cathodes are used in many ground based ion and plasma sources, which are used for plasma processing applications including ion beam sputtering and deposition. The focus of this research is to investigate and characterize the plasma produced downstream of a hollow cathode. The primary goal is to identify groups of ions and possible mechanisms responsible for their formation within a plasma discharge that might cause erosion, especially with respect to the hollow cathode assembly. This research is considered important based upon previous ion thruster life tests that have shown erosion to occur on cathode and keeper potential surfaces in contact with the discharge plasma (e.g., the hollow cathode, heater, heater radiation shielding, keeper, and screen grid). The erosion has the potential to limit the life of the thruster, especially during ambitious missions that require ultra long periods of thruster operation or high discharge plasma currents.

4

1.2 Nomenclature

Symbol	Units	Description
A	m^2	Area
B	G	Magnetic field strength
σ	m^2	Electron-ion cross section
λ_D	m	Debye length
e	C	Electron charge, $1.602x10^{-19}\ C$
E	J or eV	Energy
$\overline{E}$	V/m	Electric field
F	N	Force
I, J	A	Current
k_B	J/K	Boltzmann constant, $1.38065x10^{-23}\ J/K$
m_e	kg	Electron mass, $9.109x10^{-31}\ kg$
m_i	kg	Ion mass
$\dot{m}$	sccm	Propellant flow rate
n_e, n_i	#/m^3	Electron and ion density
P_t	Torr	Vacuum tank pressure
ϕ, V	V	Voltage potential
q	C	Ion charge
T_e, T_i	K or eV	Electron temperature, ion temperature
v	m/s	Velocity

5

1.3 Electric Propulsion

1.3.1 Electric Propulsion Background

The main goal of any space propulsion system is to generate thrust to propel a spacecraft, whether by chemical (rocket) or electrical (electric propulsion) means[1,2]. In an electrostatic ion thruster, the thrust, T, is generated by expelling mass from the spacecraft at a given rate, $\dot{m}$, at an average velocity, $\overline{U}$:

$$T = \dot{m} \cdot \overline{U}$$

Eq. 1.1

Given a spacecraft mission, there is an associated change in velocity, called the characteristic velocity, ΔV, which is necessary to achieve the desired objectives of the mission (e.g., a final destination, station keeping for a given duration, rendezvous at various locations, sample and return, etc.). More ambitious missions require higher velocity changes. The velocity change can be related to exhaust velocity by the rocket equation:

$$\Delta V = n_u \cdot \overline{U} \cdot \ln\left(\frac{m_{initial}}{m_{final}}\right)$$

Eq. 1.2

Here, $m_{initial}$ and m_{final} are the initial and final spacecraft masses and n_u is the propellant utilization efficiency. For missions where the ΔV is large, a higher exhaust velocity allows for a larger fraction of the initial mass to be retained at the end of the mission. Or in other words, the propellant mass, $m_p = m_{initial} - m_{final}$, required by the mission is a smaller fraction of the total spacecraft mass. The exhaust velocity for a given mission can be optimized based on the characteristic velocity, power supply specific mass, propellant usage, and time of flight considerations[3]. For most ambitious missions considered within the range of the solar system, the optimal exhaust velocity is in the

6

10,000 to 100,000 m/s range[1]. Electric propulsion devices can achieve these exhaust velocities while chemical rockets can not. As a result, electric propulsion can perform some of these missions with lower initial mass depending upon the amount of mass required for the power supply system.

Ion thrusters operate with high overall efficiency ($n_t \sim 60$ to 80 %), with much of the available power going into accelerating the ions to the desired exhaust velocity. The overall thruster efficiency, n_t, is defined using the thrust, T, propellant flow rate, $\dot{m}_p$, and input power, P, as[4]:

$$n_t = \frac{T^2}{2 \cdot \dot{m}_p \cdot P}$$

Eq. 1.3

Due to limitations on the power available to most spacecraft, the mass flow rate to an ion thruster is relatively low, resulting in low overall thrust. Consequently, to achieve large spacecraft velocity changes, ion thrusters must operate for very long periods of time (on the order of years) in either continuous or periodic (on/off) modes.

1.3.2 Ion Thruster Considerations

There are three types of electric propulsion thrusters[2]: 1) electrothermal, 2) electromagnetic, and 3) electrostatic. Electrothermal propulsion involves the process of electrically heating the propellant and then expanding the propellant through a nozzle to produce thrust. These types of thrusters include resistojets, arcjets, and inductively and radiatively heated devices. Electromagnetic propulsion utilizes a combination of electric and magnetic fields to produce thrust efficiently. Examples include magnetoplasmadynamic (MPD), Hall-current, and pulsed plasma thrusters. Electrostatic propulsion devices, ion thrusters, use electric fields to accelerate ionized particles to

7

produce thrust. This research will focus on hollow cathodes used in ion thrusters (more specifically the electron bombardment ion thruster), although hollow cathodes are also used in Hall-current thrusters for the same purpose.

A schematic of the ion thruster is shown in Figure 1.1. The ion thruster works by ionizing propellant to create a plasma and then accelerating the charged particles to high velocities to create thrust[4,5].
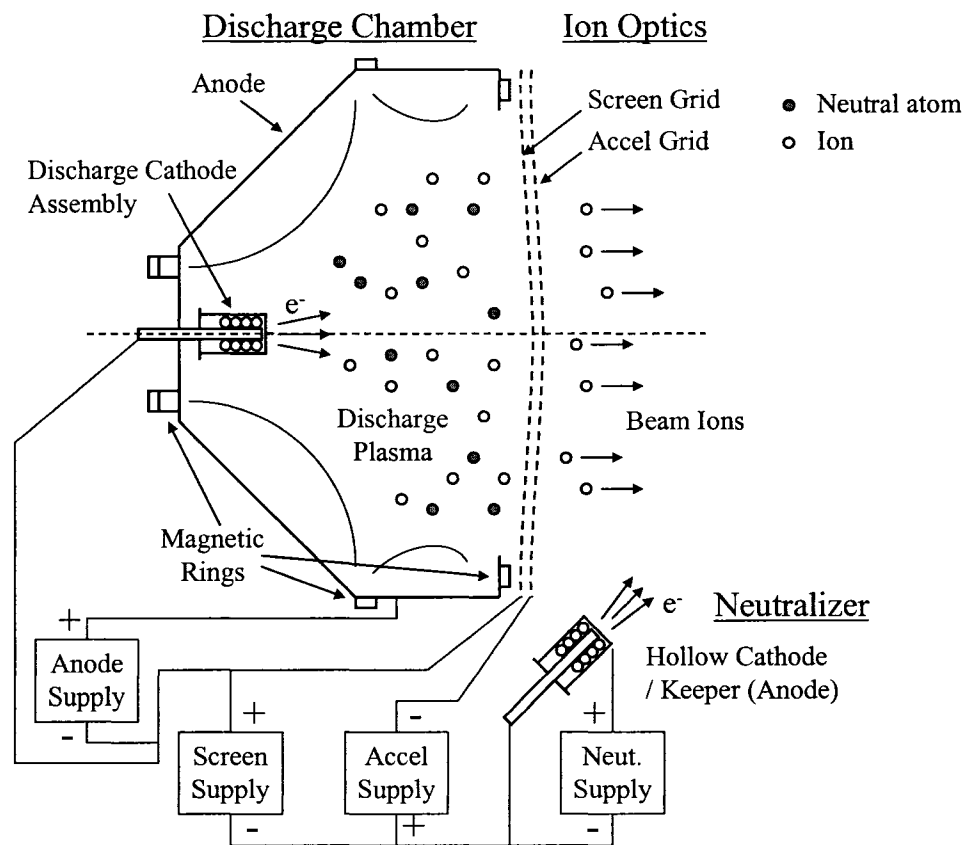
Figure 1.1   Ion thruster schematic. The ionized particles generated in the discharge chamber are accelerated by the ion optics to create thrust. An equal amount of electrons are ejected from the thruster neutralizer to maintain charge neutrality.

The plasma is created within the discharge chamber by first drawing electrons from the hollow cathode. The hollow cathode works by heating a low work function insert to emit electrons from the surface. The anode is biased positive of the cathode so

8

that electrons from the cathode gain energy and collide with the neutral propellant. A fraction of the atoms introduced into the discharge chamber through the plenum and cathode are ionized to form the plasma. A magnetic field is used to confine the electrons to increase the probability of ionization of neutral atoms.

Some of the ions that are created in the discharge plasma drift toward the ion optics system. Often the ion optics system is comprised of two grids: the screen grid and accelerator (or accel) grid. The accelerator grid is biased negative of the screen grid and plasma so that the ions are accelerated as they pass through the ion optics system. An example ion optics system is shown in Figure 1.2 along with a schematic of ions being drawn from the discharge plasma and accelerated from the thruster. The maximum amount of ion current that can be drawn through each "beamlet" (one screen-accel hole pair) is determined using the Child-Langmuir law or perveance equation, which takes into account space charge limitations[2,6]:

$$j_{b\_max} = \frac{4 \cdot \varepsilon_o}{9} \sqrt{\frac{2 \cdot q}{m_i}} \cdot \frac{V_T^{3/2}}{d^2}$$

Eq. 1.4

Where ε_o is the permittivity of free space, q is the electric charge, m_i is the ion mass, V_T is the total voltage applied to the grids, and d is the effective distance between the grids. To maintain charge neutrality on the spacecraft, an equal number of electrons must be ejected for each beam ion. This is accomplished using a second electron source, also a hollow cathode, called the neutralizer that is placed near the ion optics system.

9

Screen Grid —

Accel Grid —

Direction of
ion travel
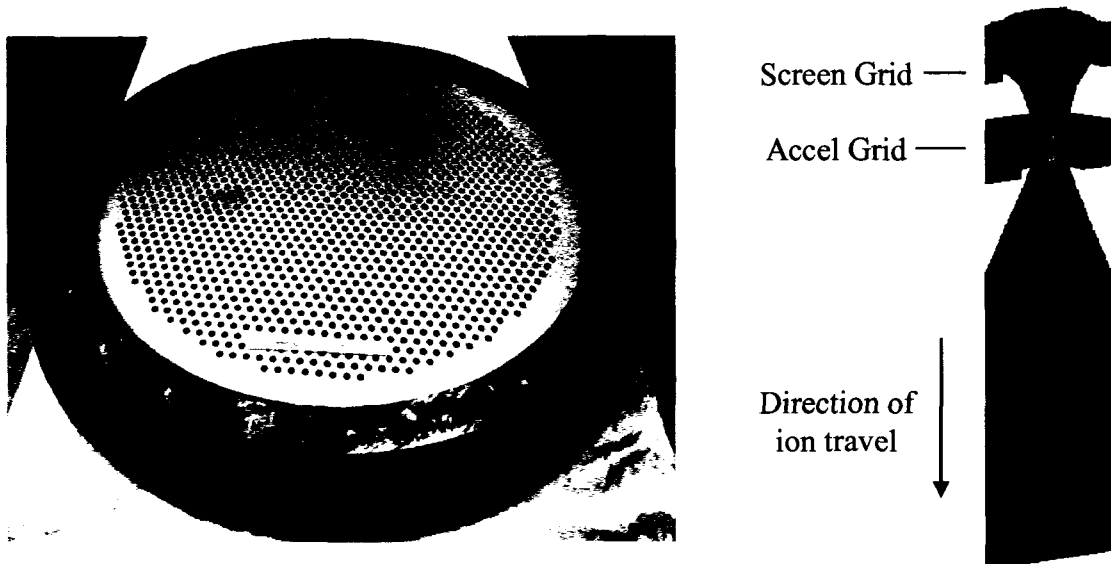
Figure 1.2 Photograph of an ion thruster grid set[7]. The ion optics consists of many small apertures (or "beamlets") through which the ions are accelerated to very high velocities[6].

1.4 Hollow Cathodes

In space applications, hollow cathodes are used in electrostatic propulsion devices, especially in ion thrusters and Hall thrusters, to provide electrons to sustain the plasma discharge and neutralize the ion beam. Hollow cathodes can also be used as plasma contactors on spacecraft to reduce spacecraft charging. Also, hollow cathodes are used in many ground-based ion sources, which are used for processing applications including ion beam sputtering and deposition.

The purpose of the hollow cathode in an ion thruster is to readily emit a steady current of electrons over a long period of time. The hollow cathode assembly consists of the cathode tube, low work function insert, heater, and keeper as shown in Figure 1.3. A plasma is generated within the hollow cathode by flowing propellant through the cathode tube and heating the low work function insert to thermionically emit electrons off the surface. The electrons collide with the neutral atoms within the tube to excite and ionize

10

a fraction of the propellant to create the plasma. The keeper is biased positive of the cathode to draw electrons from within the cathode and into the main discharge chamber.

The mechanism of electrons being emitted from the insert surface is called field-enhanced thermionic emission. The cathode generally operates around 1000 degrees Celsius to ensure sufficient electron emission from the low work function insert[8]. During cathode startup, the required ignition temperature is reached using a heater that is coiled around the cathode tube. Once the discharge is initiated, the cathode and insert temperatures are maintained through surface heating from the intense plasma produced within the cathode tube and the heater power can be turned 'off'. In addition to heating the cathode insert, the intense plasma forms a thin sheath just above the insert surface that results in a strong electric field. The field enhancement process serves to further lower the effective work function and ensure that the insert surface can emit the demanded electron current.

In a conventional hollow cathode, the electron insert consists of a porous tungsten tube that is impregnated with a mixture of barium calcium aluminate (BaO, CaO, and Al_2O_3). Ba and BaO from the impregnate rise to the insert surface and coat it resulting in a dramatically lower work function compared to the work function of a porous tungsten surface. Two standard impregnate mixtures used most often to fill the pores in the tungsten insert are $Ba_4CaAl_2O_8$ and $Ba_6CaAl_4O_{13}$, also known as 411 and 612, respectively, because of their relative molar ratios [i.e., 4(BaO), 1(CaO), and 1(Al_2O_3) and 6(BaO), 1(CaO), and 2(Al_2O_3)]. Newer impregnate combinations and insert materials being used and considered for cathode inserts include barium scandate, tungsten-iridium, and lanthanum hexaboride (LaB_6)[9].

11

There are a few failure modes that have been identified for the hollow cathode assembly. They include erosion to the orifice and surfaces, insufficient supply rate of barium, insert poisoning, and tungsten transport to undesired regions[10]. The focus of this research is to investigate hollow cathode sputter erosion, which is thought to be primarily caused by ions generated downstream of the hollow cathode in the discharge plasma.
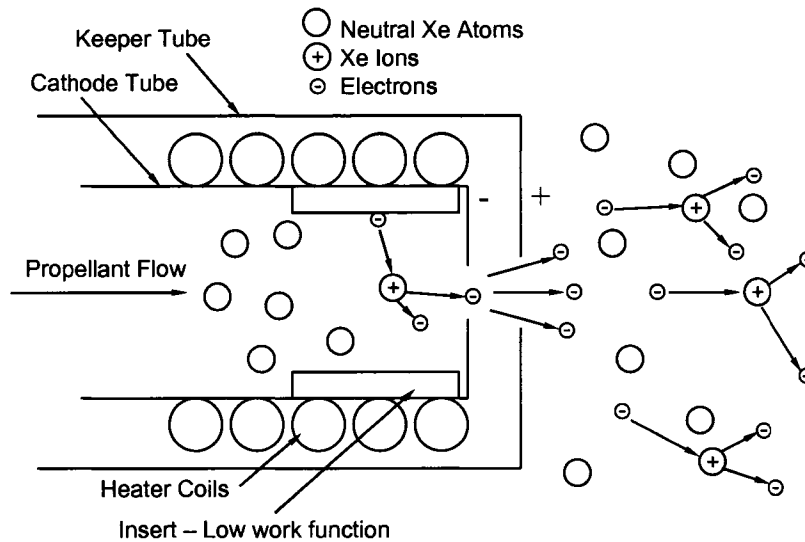
Figure 1.3a Diagram of the hollow cathode. Electrons are emitted from the low work function insert to sustain the plasma.
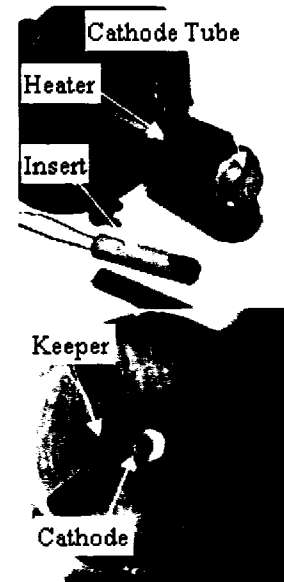
Figure 1.3b Hollow cathode, insert, and front view with the enclosed keeper.

1.5 Cathode Erosion and Engineering Solutions

1.5.1 Importance of Hollow Cathode Erosion

Discharge cathode erosion has been identified as one source of life limiting failure of ion thrusters in space missions[11,12]. As missions become more ambitious, thruster lifetime requirements increase based on the time to thrust to achieve the desired change in velocity, ΔV. Extensive ground and in-space testing has been performed on the NSTAR ion thruster, which demonstrated an in-space firing sequence of 16265 hours in duration.

12

Ground based tests on the NSTAR thrusters and similar derivatives have consisted of operational periods of 1000 hours, 8200 hours, and an extended life test that ran for over 30000 hours. Cathode erosion was observed in all of these life tests. Other high current cathode validation tests have shown much more severe erosion to the cathode assembly after shorter periods of operation (500 to 2000 hours)[13,14,15]. Figure 1.4 shows erosion that occurred to the hollow cathode keeper on an NSTAR thruster during the extended life test[16].

| 0 hrs | 4693 hrs | 10451 hrs | 21306 hrs | 30352 hrs |
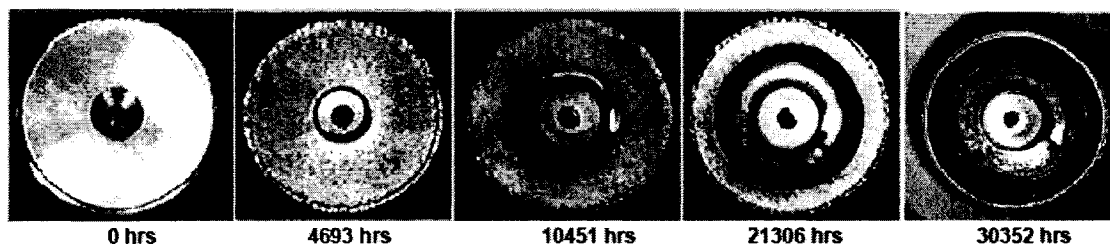
Figure 1.4 Pictures of the discharge cathode assembly at different times on the NSTAR extended life test thruster. The keeper orifice enlarged over time, presumably from ion bombardment from ions produced in the plasma downstream of the cathode orifice[16].

With ion bombardment from the plasma, the keeper, cathode, and eventually heater eroded due to sputtering[16]. In time, the heater could erode to the point where the heater filament opens. Once this occurs, the discharge cathode could no longer be started because the temperature (~1000 degrees Celsius) required to re-start the cathode could not be achieved.

1.5.2 Engineering Solutions

The effects of erosion to a hollow cathode assembly can be mitigated in several ways. One engineering solution to reduce cathode orifice plate erosion was to add an enclosed keeper[11]. The orifice plate of the enclosed keeper structure acts to shield the cathode and heater from direct bombardment from plasma ions. The enclosed keeper

13

allows for longer lifetimes because the keeper acts mostly as a sacrificial element once the cathode is operating. An increased lifetime could come from a thicker keeper plate as long as the potential profiles (temporal and spatial) around the cathode are not adversely affected.

Another engineering solution to increase cathode lifetimes is to modify the cathode assembly materials so that they are more resistant to sputtering. Similar to material selection for ion thruster optics design, carbon/graphite has been considered as an improvement to molybdenum based on lower sputter yield rate predictions of graphite[7]. Tantalum is another material that has been considered for keeper use due to low sputter yield characteristics in comparison to molybdenum[16].

A more useful (however more difficult) solution would be to modify the plasma characteristics near the hollow cathode, since cathode erosion is most likely caused by sputtering from ions, sometimes highly energetic, that are produced within the discharge plasma[17]. This is the focus of the research presented herein. There are a few ways erosion could be reduced including 1) reduction of the local plasma potentials and thereby energy of the ions produced near the cathode and/or reduction of the production rate of multiply charged ions near the cathode, 2) reduction of the plasma density produced near the cathode, or 3) re-direction of ions that are produced nearby the cathode to regions away from the cathode. All of the above (if possible) may involve a combination of changes to the ion thruster such as the discharge chamber geometry, cathode geometry, keeper geometry, magnetic field strength and geometry, cathode flow rate, main discharge flow rate, keeper current, discharge current, etc.

14

1.5.3 Sputtering

The erosion of the cathode assembly is based upon the relationship between the plasma properties and how ions from the plasma impact the cathode. Sputtering is an extensive field of study and has many applications outside of electric propulsion. The largest field is in material processing, such as semiconductors, where ion beams are used to sputter, implant, and etch the surface of materials to achieve desired surface qualities and material coatings.

Sputtering, which is an area of interest in regard to hollow cathodes and this research, involves the process of removing material from a surface as a result of particle impact[18]. When an energetic ion hits a surface there is a certain probability that atoms will be ejected, or sputtered, from the surface. The total sputter yield, Y, is defined as the number of atoms ejected from the surface per incoming ion. Major factors that affect the sputter yield are the ion energy, ion species, incidence angle, and the target species and surface properties. An example sputter yield curve is shown in Figure 1.5 for xenon atoms striking a molybdenum target at an incidence angle of 0 degrees[19]. The sputter yield increases as the ion energy impacting the surface is increased. From knowledge of the plasma properties and surface variables, the erosion rate could be calculated. The erosion rate gives an estimate for how long a material, such as a keeper plate or cathode, would last when exposed to the plasma.
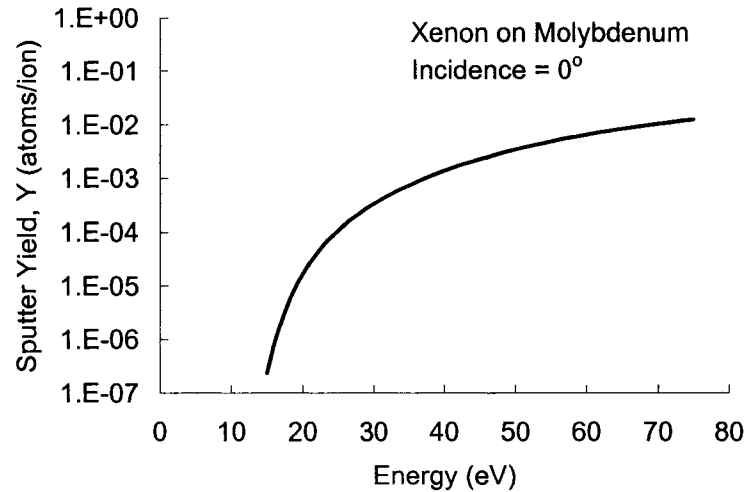
Figure 1.5 Example sputter yield curve for xenon atoms striking a molybdenum target at an incidence angle of 0 degrees (curve fit of data from ref. 19).

1.6 Proposed Mechanisms for Accelerated Erosion

Ions that are created in a plasma can sputter erode the surfaces of the cathode assembly[11,15]. The erosion rate of the cathode and keeper could increase if the energy of the incoming ions is increased or if the flux of ions is increased. Therefore, it is of interest to not only investigate how the cathode components are eroded, but to investigate possible mechanisms which cause the higher than anticipated erosion rates that are observed in some tests. The following sub-sections describe possible mechanisms that could cause increased erosion of the hollow cathode/keeper assembly.

1.6.1 Potential Hill Model

The potential hill theory was proposed to explain how ions could be created that have the ability to quickly erode materials within the discharge chamber, especially near the hollow cathode. The idea is that a steady (DC) potential hill could be formed just downstream of a hollow cathode that would serve to generate energetic ions (once they

16

fall from their point of origin to a cathode and keeper surface). Various research, such as that from Friedly[17], Williams and Wilbur[20], Kameyama and Wilbur[21], Crofton and Boyd[22], and Katz et al.[23], have proposed that such a potential hill could exist given the relative speeds and densities of electrons and ions that are created in the high density plasma. The size and shape of the potential hill, and therefore the resulting energies of ions from the region, would change depending on the discharge chamber geometry, flow rate, discharge voltage, and discharge current. Other areas of research have also looked at potential hills. One example is Hantzsche[24] who discussed a model for hydrodynamic drag in vacuum arcs in which a potential hump (or hill) exists near the cathode arc point. In this model, forces from electric fields, pressure gradients, and electron-ion friction were considered to act on the ions and electrons.

1.6.2 Magnetohydrodynamic Effect – MHD Effect

The MHD theory involves the effects of electron currents flowing through the hollow cathode orifice. The idea is that the electron flow from the cathode produces a self-induced magnetic field, which then yields a Lorentz force. However, Kameyama[25] indicated the energy gain from the force would be relatively small for the cathodes considered (~ 0 to 1 eV), indicating that this effect would not cause significantly higher ion energies to be produced near the cathode.

1.6.3 Orifice Causes (Orifice Wall Kinetic Energy Collisions)

Foster and Patterson[26] investigated ion energy distribution functions in a hollow cathode discharge plasma environment similar to research performed at Colorado State University. Electrostatic analyzer (ESA) measurements of the discharge plasma showed

17

ion energy distribution functions with a wide spread of energies including energetic ion tails. One idea proposed by Foster and Patterson was that energetic ions could be produced within the hollow cathode orifice by multiple ionization reactions occurring within the orifice combined with finite fractions of left-over kinetic energy from glancing wall neutralization events. This theory does not agree well with experimental measurements because large numbers of energetic ions are observed at large off-centerline angles, and because erosion is detected on the downstream surface of the keeper orifice plate.

1.6.4 Multiply Charged Ions / Potential Wells (Directed Ions)

Both Domonkos and Williams[11,27] and Herman and Gallimore[28] compared measured erosion rates from the 1000 hour and 8200 hour tests of the NSTAR discharge chamber to simple sputtering models. The models used values for the ion energies, ion current densities, and ion incidence angles that were derived from experimental measurements, and an assumed fraction of doubly charged ions (5 to 20 %) that might exist near the hollow cathode. The estimated erosion rate came close to the observed erosion rate considering the uncertainties in sputter yields at low energies. Since the doubly charged ions were observed to cause nearly all of the cathode erosion, this theory implies that ions with energies above the cathode to anode potential do not play a significant role in cathode erosion, especially for the conditions found within the NSTAR discharge chamber. In addition to the researchers mentioned above, recent work from Herman and Gallimore[29], Goebel et al.[30], and Martin et al.[31], have measured DC potential wells directly in front of the hollow cathode. Ions produced within the potential well would be channeled toward the cathode assembly if a low potential path existed from the

18

potential well region to the cathode. However, unless these ions were multiply charged, they would not strike the cathode assembly surfaces with significant energy to sputter.

1.6.5 Potential Well (Charge Exchange)

Katz et al.[32] have proposed a possible mechanism for the formation of energetic ions that involves charge exchange neutralization near the hollow cathode. The idea is that ions will alternately gain kinetic energy and then potential energy by going through a charge exchange process within a potential well that exists near the hollow cathode. In addition to the DC potential well, this idea can be combined with potential structure oscillations to produce ions with energies higher than the cathode-to-anode voltage difference. Calculations of potential profiles and estimates of plasma properties were made to combine the theory with RPA measurements made at remote axial and radial locations from a hollow cathode experiment. Although this work is promising, Katz et al.[32] point out that most of the ions would not be directed toward the cathode assembly and therefore might not be critical in affecting cathode erosion.

1.6.6 Oscillations / Turbulent Ion Acoustic Waves

In a discharge, it is common to have plasma oscillations due to the counter streaming currents of ions and electrons and due to steep gradients in plasma production rates. Oscillations based on these processes have been observed in Hall type thrusters as well as in ion thrusters[33]. For example, noteworthy discharge voltage oscillations of about 5 to 10 V peak-to-peak were measured in an NSTAR-like discharge by Domonkos and Williams[11] compared to the DC discharge voltage which was around 25 V. Oscillations of this magnitude can be present in the discharge plasma flow fields as well,

19

especially for operation at high discharge current, high discharge voltage, or low flow rate conditions. As an example, large amplitude plasma potential oscillations (~ ±20 V) were observed nearby a hollow cathode at some operating conditions by Goebel et al.[30] that could produce ions with energies well above the cathode-to-anode voltage. These large amplitude oscillations appeared to be present especially for lower magnitude magnetic field strengths. The presence of potential oscillations could increase sputter rates of cathode components, due to increased bombarding ion energies from ions created at higher potentials. Mikellides et al.[16] estimated an erosion rate of the keeper surface from the 8200 hour NSTAR Life Demonstration Test considering the effects of plasma potential oscillations. Assuming that singly charged ions sputter eroded the surface of the cathode (i.e., no doubly charged ions were assumed to be present), Mikellides et al. found better agreement with the experimental measurements when including the effects of high potential oscillations that would accelerate ions to higher energies and induce higher sputter erosion rates.

1.7 Investigation Summary

In view of the cathode life tests which showed erosion to the cathode assembly as well as the proposed models that identify possible mechanisms of erosion to the cathode assembly, the focus is to further investigate and characterize the plasma produced downstream of a hollow cathode. Measurements using a variety of diagnostic tools in different discharge configurations will help to identify important ion groups and formation regions for investigation of cathode erosion mechanisms.

20

2 Experimental Setup and Diagnostic Tools

This section describes the vacuum facility, discharge chamber configurations, and diagnostic tools that were used to probe plasmas. Two discharge chamber configurations were used that had different geometries, which resulted in very different plasma environments. In both cases, the same hollow cathode was used to produce and sustain the plasma. Four types of diagnostics were utilized to probe the plasma; an emissive probe, a triple Langmuir probe, a remotely located electrostatic analyzer (ESA), and an ExB probe (or Wein filter) attached to the ESA.

2.1 Vacuum Facility

All tests were performed in a 1.2 m diameter by 4.6 m long stainless steel vacuum chamber that was pumped with a 0.9-m diameter, 20-kW diffusion pump. The base pressure of this facility with no flow was 1×10^{-6} Torr after a 2 hr pump down time. The vacuum pressure was in the low to mid 10^{-5} Torr range at typical xenon flow rates of 3 to 15 sccm.

2.2 Case 1: Open Cathode (Zero Magnetic Field) Configuration

A picture of the open cathode configuration is shown in Figure 2.1. The cathode assembly was set up in the center of a stainless steel ring anode. Here, electrons were drawn from the cathode assembly to the ring anode without any other discharge chamber structure present. No magnet rings were used in this configuration. The anode was 19.5 cm in diameter and 9 cm in length. This configuration was beneficial in that the plasma was easily accessible by both emissive and triple Langmuir probes (for direct measurement) and by the remotely located ESA and ExB probes.

21
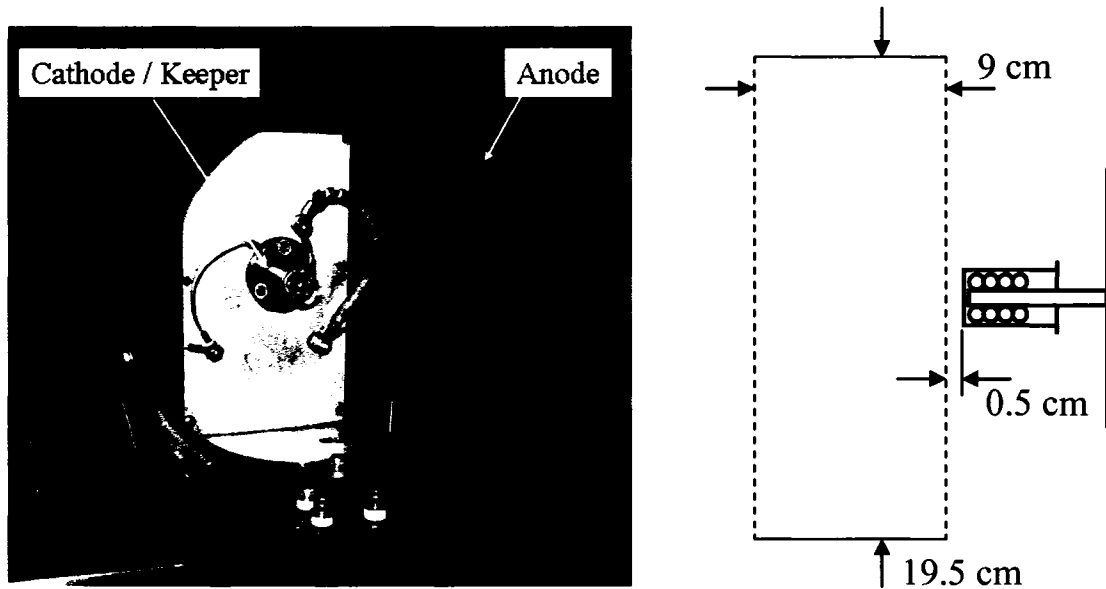
Figure 2.1 Open cathode (zero magnetic field) configuration. The anode was 19.5 cm in diameter and 9 cm in length.

2.3 Case 2: Prototype NSTAR Discharge Chamber Configuration

The second experimental setup consisted of a hollow cathode mounted within a discharge chamber as seen in Figure 2.2. The discharge chamber had a 30-cm diameter cylindrical section attached to a conical central section which was capped by a back plate and was, therefore, similar in size, shape, and magnetic field geometry to the NSTAR thruster[34,35,36,37,38]. The discharge chamber was made from sheet aluminum with an inner stainless steel lining and three magnet (samarium cobalt) rings. The first ring was located near the exit of the source (where the ion optics would be located on an actual NSTAR ion engine) at one end of the cylindrical sidewall section, the second was placed at the intersection of the cylindrical and conical anode sections, and the third behind the cathode on the back plate. A more detailed layout of the magnetic field and relative field strengths is discussed in Appendix A. A pseudo-screen grid fabricated from stainless steel and biased to cathode potential was used to simulate the neutral flow restricting

22

behavior of an actual ion optics system. Ions produced in the plasma were allowed to flow directly from the discharge chamber through a 6 mm wide slot cut in the side wall of the discharge chamber and pseudo-screen grid so they could be sensed by remotely located probes. The discharge chamber/hollow cathode system was mounted within a fixture so that it could be rotated about an axis centered at the cathode orifice thereby enabling measurements at angles from 0° to 90° with respect to the cathode centerline. This was done to investigate the size and shape of the dense plasma region produced near the hollow cathode orifice.
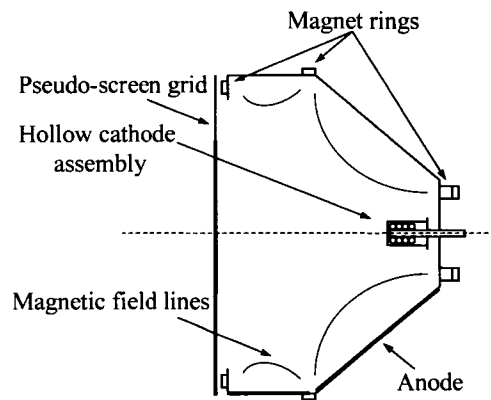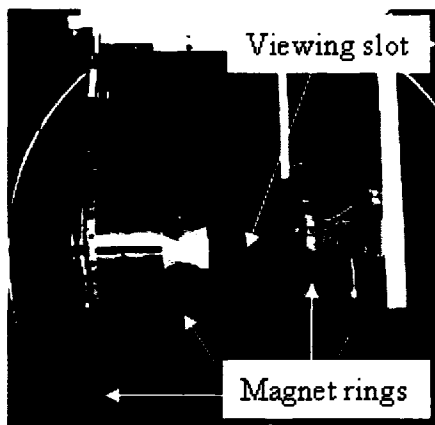

Figure 2.2a Side view of the prototype NSTAR discharge chamber.

Figure 2.2b Discharge chamber schematic.

2.4 Cathode/Keeper Assembly

The cathode/keeper assembly is shown in a side view and in a view along the cathode axis looking down the orifice in Figure 2.3. The same cathode and keeper was used in both case 1 and case 2 configurations. The hollow cathode was a 6.3 mm diameter tube that contained a low-work-function impregnated, sintered tungsten insert. The hollow cathode tube was capped with an orifice plate that had a 0.55 mm diameter orifice on its centerline. The cathode tube and insert were heated by a resistive coil

23

wrapped around the outside of the tube, which was insulated by a multiple-layer, tantalum-foil radiation shield. The enclosed keeper used with the cathode was equipped with an orifice plate fabricated from 0.635 mm thick tantalum. The keeper orifice plate had a 2.54 mm diameter orifice positioned about 0.5 mm downstream of the cathode orifice plate. It is noted that the cathode and keeper orifice diameters were similar to but not exactly the same as the discharge cathode and keeper features used in the NSTAR ion thruster. All of the xenon propellant required to operate the cathode and the discharge chamber plasma were supplied through the cathode. In case 2, because high voltages were not applied to extract ions and propellant was lost only through the relatively small slot in the chamber side-wall and the pseudo-grid surface, the flow through the cathode was sufficient to produce NSTAR-like neutral densities throughout the discharge plasma.

Figure 2.3 Cathode and keeper assembly with close-up front view of the keeper and cathode orifices.

2.5 Remote Probes – ESA, ExB

2.5.1 Electrostatic Analyzer (ESA)

A Comstock model AC-901 electrostatic analyzer (ESA), shown in Figure 2.4, was used to measure the energy of the plasma ions[39]. The ESA consisted of two

24

spherical sector plates fabricated in a 160° arc. Two collimators were used at each end of the arc to limit the field of view of the device. Both collimators were comprised of a set of two disks with 2 mm holes aligned with each other and separated by 1 cm. A nickel mesh was placed in front of the entrance aperture to shield the ESA from ambient plasma electrons that might penetrate the collimator assembly and flow around the spherical sectors to the collector electrode. The collector electrode was located downstream of the exit collimator and was well isolated from the plasma to ensure accurate current measurements. In order to collect all of the ions that passed through the ESA on the proper trajectories, a small negative DC bias was applied to the collector electrode to draw those ions to it. A computer was used to control a Keithley 617 programmable electrometer that applied both the desired potentials to the spherical plates through a resistive voltage divider circuit relative to the entrance and exit collimators and measured the ion current flowing to the collector. The voltage difference on the spherical plates was converted to ion energy (actually ion energy per charge state, E/z) using Eq. 2.1[39]:

$$\frac{E}{z} = \frac{\Delta\phi}{\frac{r_2}{r_1} - \frac{r_1}{r_2}} \quad \text{or, for the ESA geometry used:} \quad \frac{E}{z} = 2.254 * \Delta\phi \qquad \text{Eq. 2.1}$$

In Eq. 2.1, E represents the ion energy, z the ion charge state (i.e. z = 1 for singly charged ions, z = 2 for doubly charged ions, etc.), r_1 and r_2 the inner and outer radii of the ESA spherical segments, and $\Delta\phi$ the voltage difference applied between r_1 and r_2. Note that the ESA detected only the energy to charge ratio, E/z, so a singly charged ion and a doubly charged ion that went through a potential ΔV_p would be measured at the same $\Delta\phi$. Once the voltages were applied to the segments, a picoammeter built into the Keithley electrometer was used to measure the ion current that flowed to the collector electrode.

25
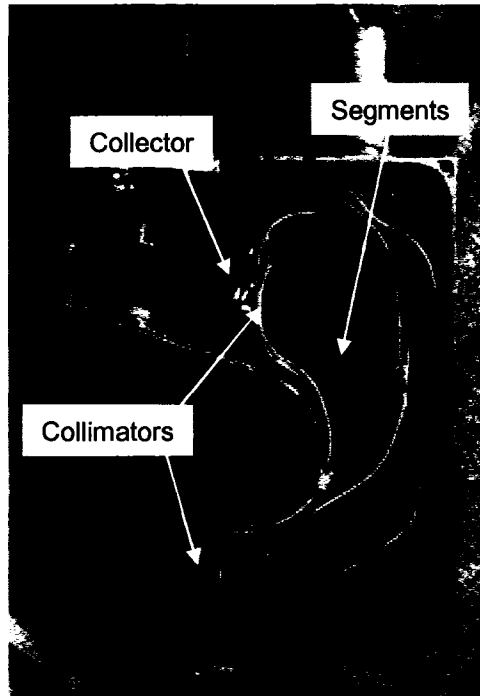
Figure 2.4a Picture of the ESA with the Figure 2.4b Diagram of the ESA.
top cover removed.
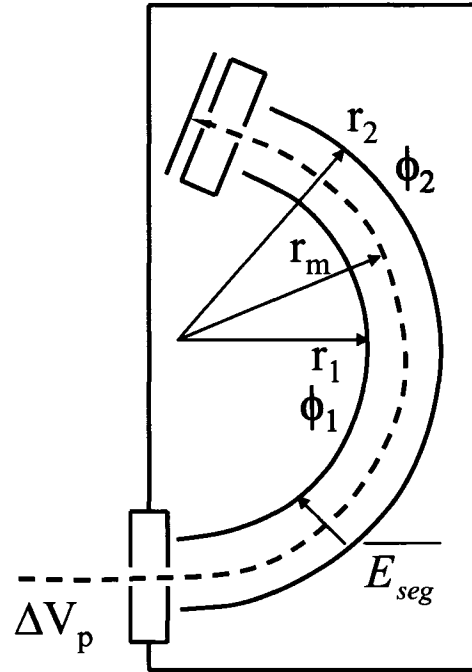
There are two modes of ESA operation that can be used to measure an ion energy distribution function (IEDF); the variable transmission energy mode (or sector field sweep mode) and the constant transmission energy mode[39]. While both modes of operation were used in this work, it was decided that the constant transmission energy mode was more suitable. When presenting data obtained with the ESA, the reader can assume that the constant transmission mode was used unless otherwise noted. In the constant transmission mode, a constant $\Delta\phi$ was applied between the segments, and the entrance and exit collimators were swept (along with the segments) with respect to the vacuum facility ground to yield the ion energy distribution function. Figure 2.5 shows an example ion energy distribution function generated with the ESA. The current to the collector plate was recorded as a function of the bias voltages, which determined the selected ion energy to charge ratio (E/z). Appendix B discusses the ESA modes of

26

operation in further detail as well as the governing equations for the relationship between the ESA geometry and the measured ion energies. For both case 1 and 2 configurations, the cathode was grounded to the vacuum test facility wall.
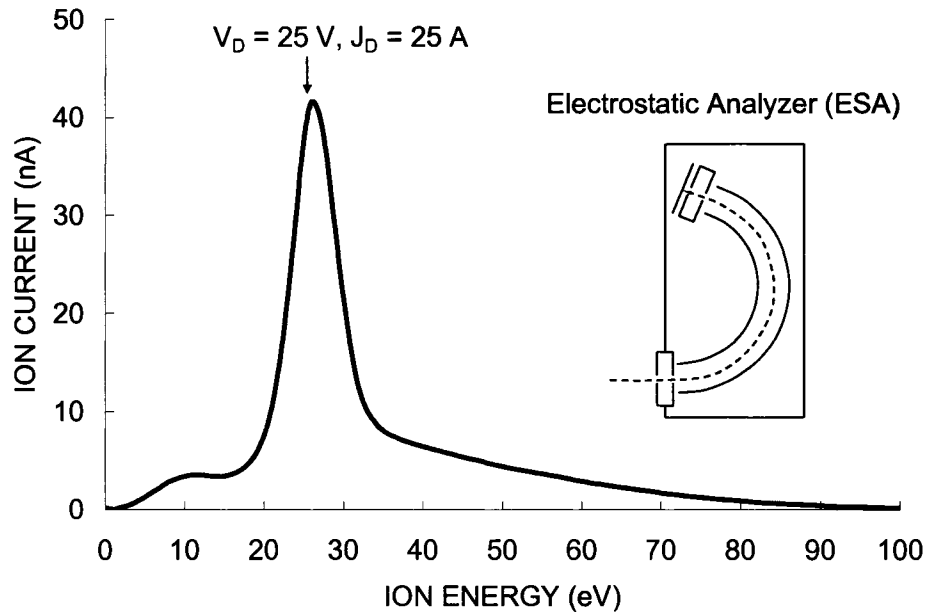

Figure 2.5 Example ion energy distribution function (IEDF) measured with the ESA.

2.5.2 Combined ESA_ExB Probe

The combined ESA and ExB probe was used to measure the energy and charge state of the plasma ions. The probe consisted of an ExB stage mounted onto the exit stage of the Comstock model AC-901 ESA[39], as shown in Figure 2.6. With this setup, an ESA trace could be taken to obtain an ion energy distribution function (E/z) by using the ExB probe collimator as an ion collector plate. Alternately, the ExB probe could be used to measure the charge state distribution when the ESA was set to transmit a given ion energy.

27
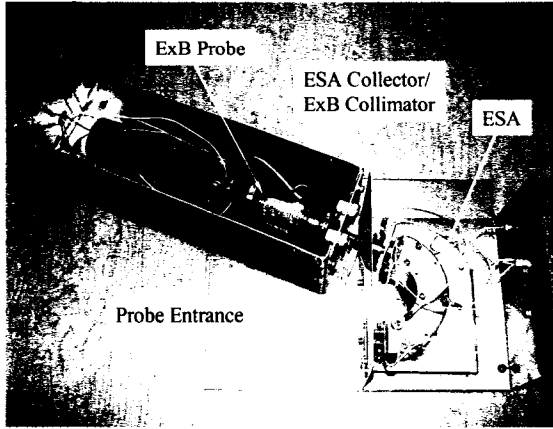
Figure 2.6a Combined ESA_ExB probe. The ESA section is used to select ions according to their energy to charge ratio (E/z) and the ExB section is used to separate ions of different charge (z).
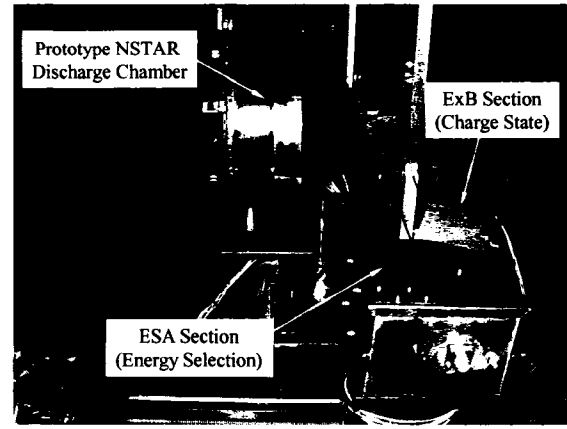
Figure 2.6b ESA_ExB probe looking toward the prototype NSTAR discharge chamber (case 2) at a zenith angle of 90 degrees.

The ExB probe (or Wein filter) is used to measure the charge state of the ions via crossed magnetic and electric fields that separate the ions[41,42]. The ExB probe schematic is shown in Figure 2.7. Ions that are able to pass through the collimator enter the separation region where they feel a force from both the electric and magnetic fields according to the Lorentz force equation:

$$\overline{F} = q \cdot (\overline{E} + \overline{v} \times \overline{B})$$ Eq. 2.2

In Eq. 2.2, F represents the force on the ion, q the electronic charge, E the electric field strength, v the ion velocity, and B the magnetic field strength. In order to pass through the probe to the collector plate, the net force on the ions must be near zero so that the ions are not pushed off the drift axis. The resulting equation for the ions that are measured by the ExB probe is:

$$\Delta V_P = \frac{m \cdot \Delta \phi^2}{2 \cdot z \cdot q \cdot d^2 \cdot B^2}$$ Eq. 2.3

28

In Eq. 2.3, ΔV_p represents the potential difference between the ion creation potential in the plasma and the probe in Volts, m the mass of the ion species in kg, $\Delta\phi$ the voltage difference between the plates in Volts, z the charge state of the ion (1, 2, etc), q the electronic charge in Coulombs, d the separation distance between the electrodes in meters, and B the magnetic field strength in Gauss. The derivation of the equations used in the ExB probe can be found in Appendix C.
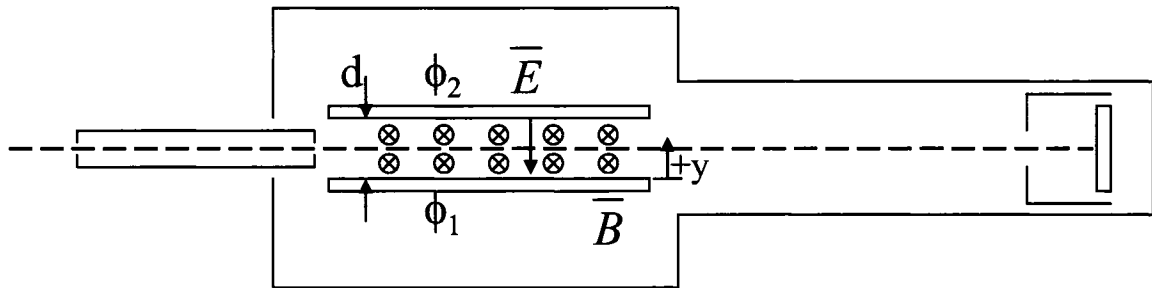

Figure 2.7 ExB probe schematic showing the electric field and magnetic field separation section. The direction change of the ion depends on its entrance energy and the applied electric and magnetic field strengths.

To differentiate the charge state of the incoming ions, $\Delta\phi$ is swept while keeping the other variables constant. For a given ΔV_p and ion mass, ions with charge z = 1 will show up at a given $\Delta\phi_1$, and ions with charge z = 2 will show up at $\sqrt{2} \cdot \Delta\phi_1$. An example plot is shown in Figure 2.8 for ions being passed through the ExB section of the combined ESA_ExB probe. The singly charged ions were measured at a plate voltage difference of about 5.1 V and the doubly charged ions were measured at a plate voltage difference of about $\sqrt{2} \cdot 5.1 = 7.2$ V. The doubles-to-singles current ratio was found by dividing the integrated area under the doubles curve by the integrated area under the singles curve. Note that no triply charged xenon ions were detected in any of the operating conditions presented herein.

29
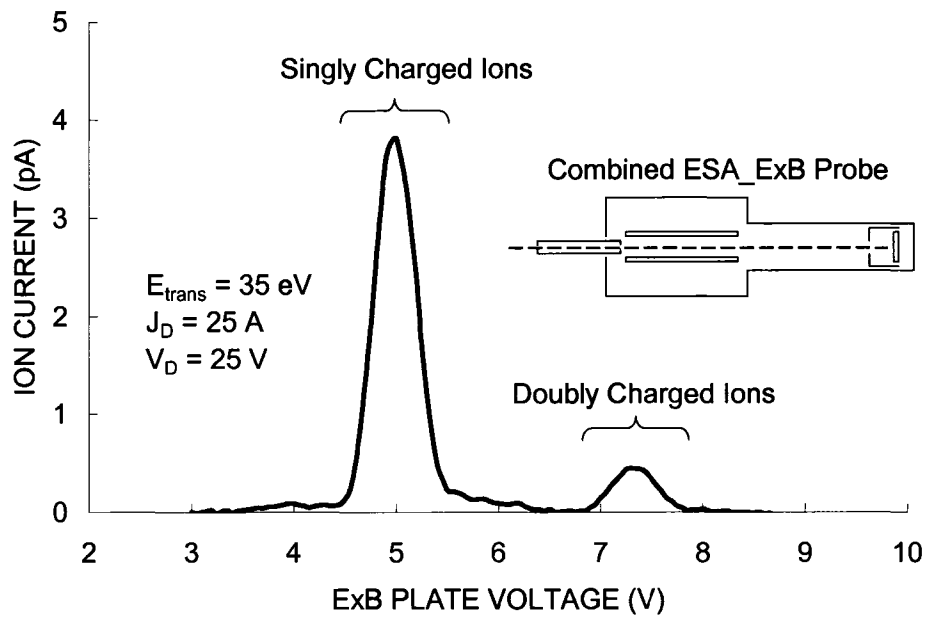
Figure 2.8 Example plot of ion current recorded at the exit of the ExB section of the combined ESA_ExB probe. The ExB probe could be used to measure charge state distributions when the ESA was set to transmit a given ion energy. At this operating condition and selected ion energy (E/z = 35 eV), the measured doubles-to-singles ratio was about 17 %.

2.6 Direct Probes – Emissive, Triple Langmuir

2.6.1 Langmuir Probes

Langmuir probes consist of conducting electrodes (single, double, or triple) placed in the plasma to collect ion and electron currents. Based on measurements of voltages and currents on the probe, discharge properties such as the plasma density, electron temperature, and plasma potential can be determined[43,44,45].

A single Langmuir probe is used by placing it into a plasma and biasing the probe over a range of potentials while simultaneously recording the current flowing to the probe. A schematic of the resulting current versus voltage (I-V) curve is shown in Figure 2.9. When the probe is biased sufficiently negative of the plasma, electrons from

30

the plasma are repelled and the probe collects ions. This is called the ion saturation region. As the probe is biased more and more positive, the probe begins to collect electrons as well as ions. This is called the electron retarding region. As the probe is biased above plasma potential, ions are repelled from the probe and electrons are collected. This is called the electron saturation region.

For a Maxwellian electron distribution, the electron temperature can be determined using Eq. 2.4 from the exponential slope of the curve in the electron retarding region[43,44]:

$$\frac{k_B \cdot T_e}{e} = \frac{1}{\left(\dfrac{d \ln(I_p)}{dV} \right)} \qquad \text{Eq. 2.4}$$

Once the electron temperature is determined, the electron density can be found ($n_i \cong n_e$) using the ion saturation current to the probe[43,44]:

$$n_e = \frac{I_{ion\_sat}}{e^{-\frac{1}{2}} \cdot q \cdot A_p \cdot \sqrt{\dfrac{k_B \cdot T_e}{m_i}}} \qquad \text{Eq. 2.5}$$

The plasma potential is determined by finding the knee in the curve between the electron retarding and electron saturation regions.

There are sources of error and difficulties with determining plasma properties from a Langmuir probe trace. The probe can perturb the local plasma with the applied bias voltages. The plasma can be non-Maxwellian (e.g., primary electrons from the cathode). The knee of the curve can be difficult to determine as well as the proper ion saturation current because of probe sheath changes with applied voltage.

31

Also, the probe must be sized properly and the measurements must be checked to determine if the probe is operating in the thin sheath or thick sheath regimes, which require different analysis techniques[45]. The thin sheath regime is generally preferred and applicable in high plasma density regions where the ratio of the probe radius to the Debye length is large. The Debye length is a measure of charge separation distances within the plasma. In the types of plasmas studied here, the equation for the Debye length is:

$$\lambda_D = \sqrt{\frac{\varepsilon_0 \cdot k_B \cdot T_e}{n_e \cdot q^2}}$$

Eq. 2.6

In Eq. 2.6, ε_0 represents the permittivity of free space, k_B Boltzmann's constant, T_e the electron temperature, n_e the electron density, and q the charge of an electron. In the thin sheath regime, the effects of the probe sheath can be neglected. In the thick sheath regime, when the ratio of the probe radius to the Debye length is lass than 3, the sheath size is significant and of its effects on charged particles collection must be considered[45].
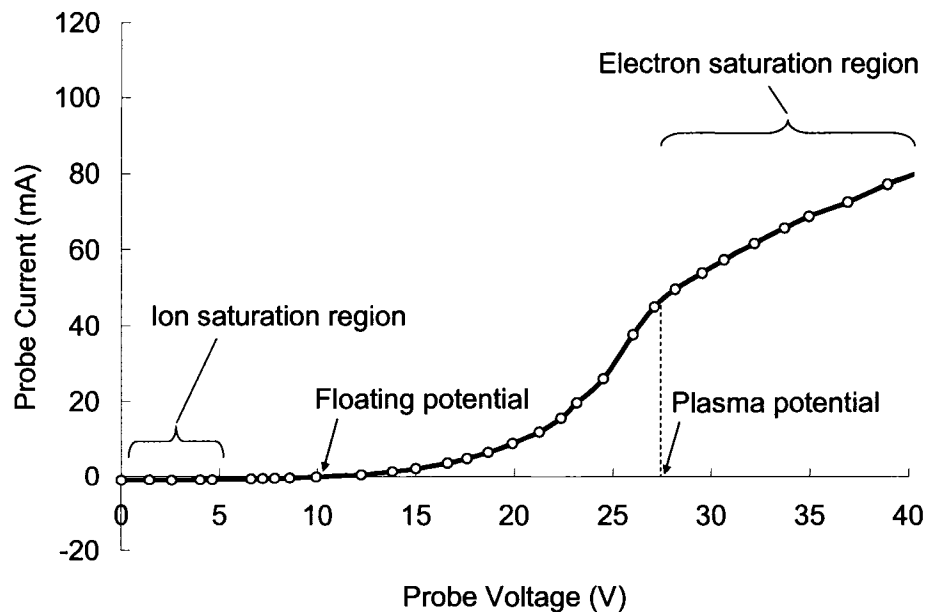

Figure 2.9 Example single Langmuir probe sweep which can yield estimates for the plasma potential, electron temperature, and electron density.

32

2.6.2 Triple Langmuir Probes

The triple Langmuir probe uses the same principles as the single Langmuir probe but has three electrodes instead of just one. The main advantages of this probe are that estimates of the plasma potential, electron density, and electron temperature can be obtained relatively quickly and without the need for a voltage sweep[46,47,48]. A diagram of the triple probe is shown in Figure 2.10. Three tantalum electrodes with a diameter of 0.381 mm were used in this study. The electrodes were housed in ceramic aluminum oxide tubing with a separation distance of 1.0 mm. With this probe configuration, four voltages were recorded. Specifically, the floating potential was measured on one of the three electrodes while the other two electrodes were biased with respect to the third electrode using a power supply to measure ion and electron currents. The bias voltage, V_4, was held constant. The negatively biased electrode collected ions while the positively biased electrode collected an equal current of electrons. The floating feature of the triple probe helps to reduce plasma perturbations because a net current of zero is drawn from the plasma.

33
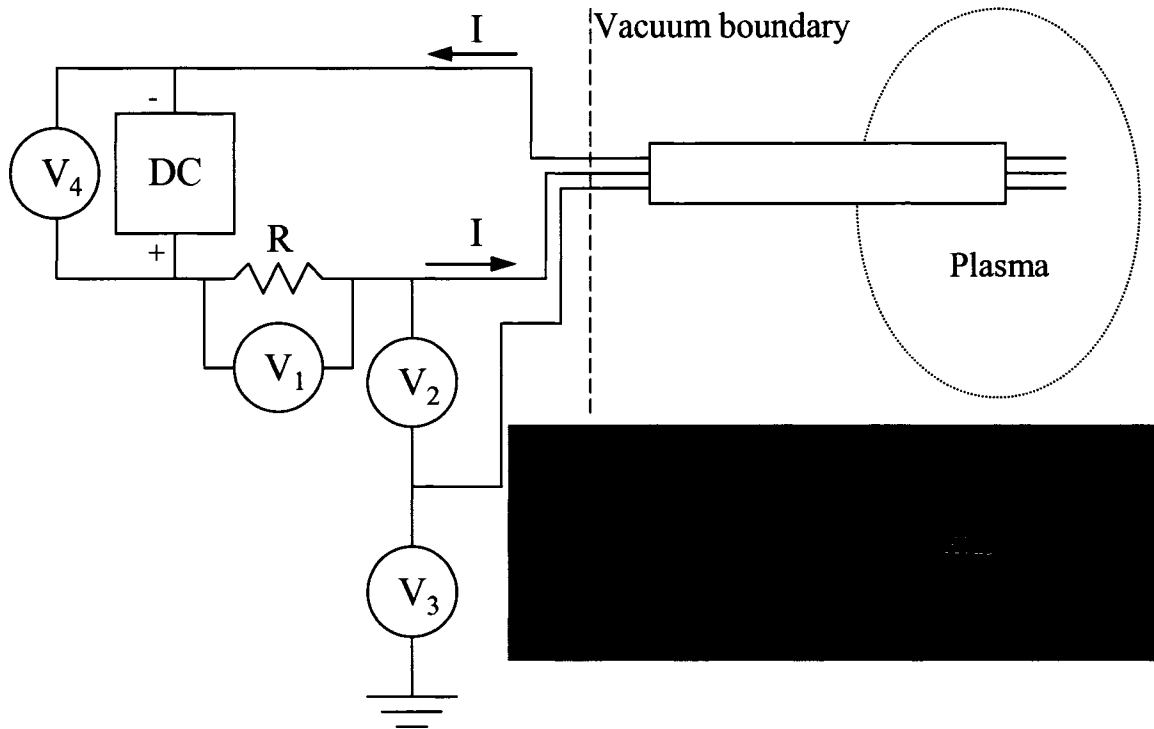
Figure 2.10 Triple Langmuir probe. Three tantalum electrodes having a radius of 0.381 mm and length of 3.3 mm were used.

From the measured current and voltages, the electron temperature, plasma potential, and electron density can be estimated. The method of Beal[43] was followed for the triple probe analysis. First, the electron temperature is found from the measurements of V_2 and V_4 [43,46]:

$$T_e = \frac{V_2}{\ln\left(\dfrac{2}{1+e^{\left(\frac{-V_4}{T_e}\right)}}\right)}$$

Eq. 2.7

In Eq. 2.7, T_e represents the electron temperature in eV. Next, the plasma potential can be found by equating the electron and ion currents to the floating electrode and from the floating potential, V_3, and the electron temperature, T_e [47,48]:

34

$$V_p = V_3 + T_e \cdot \ln\left(\frac{1}{0.6} \cdot \sqrt{\frac{m_i}{2 \cdot \pi \cdot m_e}}\right)$$

Eq. 2.8

The electron density can be found from the ion current collected by the probe and the electron temperature[43,48]:

$$n_e = \frac{I}{0.6 \cdot A_p \cdot q^{\frac{3}{2}}} \cdot \sqrt{\frac{m_i}{T_e}} \cdot \left(1 - \frac{2 \cdot e^{\left(\frac{-V_4}{T_e}\right)}}{1 - e^{\left(\frac{-V_4}{T_e}\right)}}\right)^{-1}$$

Eq. 2.9

There are certain requirements for the emissive probe relations to be valid[48]. The probe geometry must be small such that the three electrodes are exposed to the same plasma environment. However, the electrodes must be spaced far enough apart (many Debye lengths) so the sheaths around each electrode do not affect the other electrodes. As with the single Langmuir probe, quasineutrality is assumed and the electron population is assumed to be Maxwellian[46].

In the data presented herein, an effective collection area, A_s, was used in place of the probe area, A_p, in Eq. 2.9 following Beal[43]:

$$\delta = 1.02 \cdot \lambda_D \cdot \left[\left(\frac{1}{2} \cdot \ln\left(\frac{m_i}{m_e}\right)\right)^{\frac{1}{2}} - \frac{1}{\sqrt{2}}\right]^{\frac{1}{2}} \cdot \left[\left(\frac{1}{2} \cdot \ln\left(\frac{m_i}{m_e}\right)\right)^{\frac{1}{2}} + \sqrt{2}\right]$$

Eq. 2.10

$$A_s = A_p \cdot \left(1 + \frac{\delta}{r_p}\right)$$

Eq. 2.11

This correction is applied to account for the effective sheath area instead of using the thin sheath assumption only. The effective collection area approaches the probe area as the

35

plasma density increases or the electron temperature decreases (as reflected through the Debye length).

2.6.3 Emissive Probe

An emissive probe is used to measure the potential of the plasma[29,49]. A picture of the emissive probe is shown in Figure 2.11. Normally, a conducting electrode placed in a plasma will float at a potential below the true plasma potential due to the higher flux of electrons in the plasma relative to more massive ions. In an emissive probe, a filament is heated to the point where it will emit electrons and neutralize the surrounding plasma sheath. When hot enough, the probe will float near the true plasma potential. This is useful because it enables direct and straightforward measurement of plasma potential compared to the analysis required to obtain plasma potential from Langmuir probe data.

There is some uncertainty in the potential measurement when using a floating emissive probe. One source of error is a voltage drop that occurs across the filament from the heating power supply. In this study, the voltage drop was about 5 V at a heating current of 3.4 A for a 0.127 mm diameter filament. Another source of error is due to the fact that the heated probe floats at a potential slightly below the true plasma potential. It is commonly accepted that a sufficiently heated probe will float below true potential by about 1.03 times the electron temperature in eV[47]. The expected electron temperatures were in the 1 to 3 eV range for the plasma near the hollow cathode. Therefore, in most cases the floating potential was recorded with respect to the positive terminal to bias the measurements closer to the actual plasma potential. Even though the measurements are biased, it is anticipated that an error of ±3 V still exists.
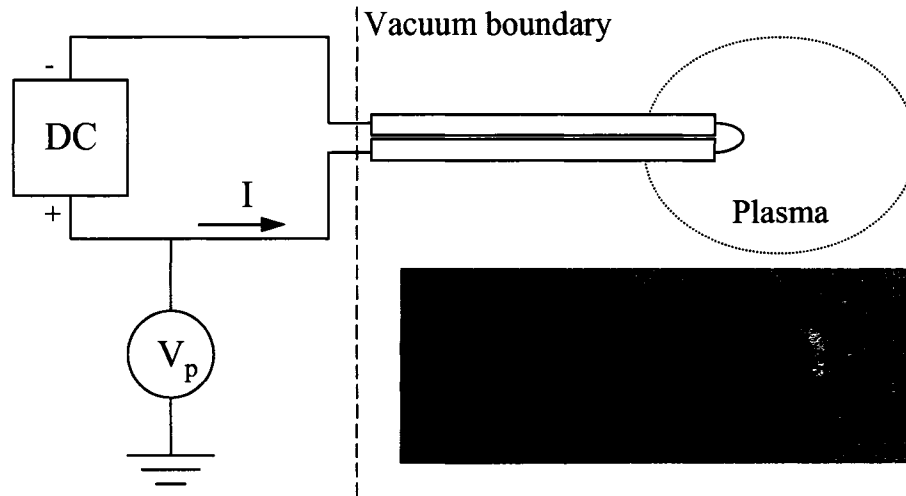
Figure 2.11 Floating emissive probe used to measure the local plasma potential (0.127 mm diameter filament).

For the measurements presented here, the plasma potential, V_p, was measured using a voltmeter connected to the probe through a high impedance, low capacitance amplifier circuit, similar to the one used by Goebel[50]. The circuit was necessary for two reasons: 1) to reduce the effects of the relatively low impedance meter that is used to measure the floating potential of the probe, and 2) to allow for measurements of plasma oscillations. The emissive probe circuit is shown in Figure 2.12. The maximum potentials that could be measured were 85 V relative to ground, which was limited by the drain voltage on a high impedance transistor. An approximate 10:1 voltage resistor divider was used to reduce the output voltage of the circuit to below 10 V prior to insertion into a data acquisition system. The data acquisition system was capable of sampling at rates of up to about 2 MHz, and the probe response was limited to 0.5 MHz.

37
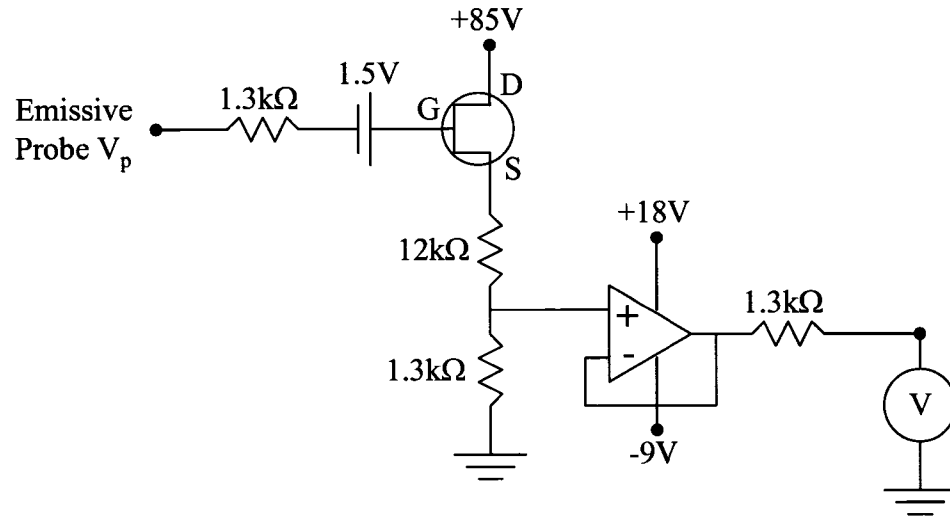
Figure 2.12 High impedance circuit used to measure the potential on the floating emissive probe[50].

38

3 Data and Results

Results will be presented for two discharge chamber configurations. The first case that will be discussed is for the open cathode (zero magnetic field) configuration (case 1). The second case that will be discussed is for plasma produced within a prototype NSTAR discharge chamber (case 2). One main difference between the two cases is the magnetic field confining the plasma. The operating conditions for both cases are summarized in Table 3.1.

Table 3.1 – Operating conditions for the discharge chamber configurations.

Case	Condition	J_D (A)	V_D (V)	Flow (sccm Xe)	P_t ($\times 10^{-5}$ Torr)
1 Open cathode	1a	3.75	32.0	7.6	4.7
	1b	7.5	33.0	7.6	4.7
	1c	11.25	34.0	7.6	4.7
	1d	15.0	33.5	7.6	4.7
	1e	15.0	41.0	9.8	5.9
2 Prototype NSTAR	2a	4.5	24.8	3.3	1.7
	2b	8.3	24.9	6.1	2.8
	2c	8.3	22.5	13.0	5.6
	2d	13.0	25.2	13.1	5.7
	2e	18.0	24.9	13.0	5.6
	2f	18.0	36.0	8.3	3.9

3.1 Case 1: Open Cathode (Zero Magnetic Field) Configuration

Results will be presented for five operating conditions in the open cathode configuration, as seen in Figure 3.1. The five operating conditions are summarized in Table 3.1. Four of the conditions (1a-1d) were chosen to investigate the effects of discharge current, which was varied from 3.75 A up to 15 A. The fifth condition (1e) was chosen to investigate the effect of varying the cathode flow rate on the downstream

39

plasma structure. The heater and keeper power supplies were turned 'off' for all of the tests.

At each of the operating conditions, plasma measurements were made with the emissive probe, triple Langmuir probe, and the ESA_ExB probe. Each probe could be mounted to two linear stages (in an x-y orientation) to allow for movement to different locations within the plasma.
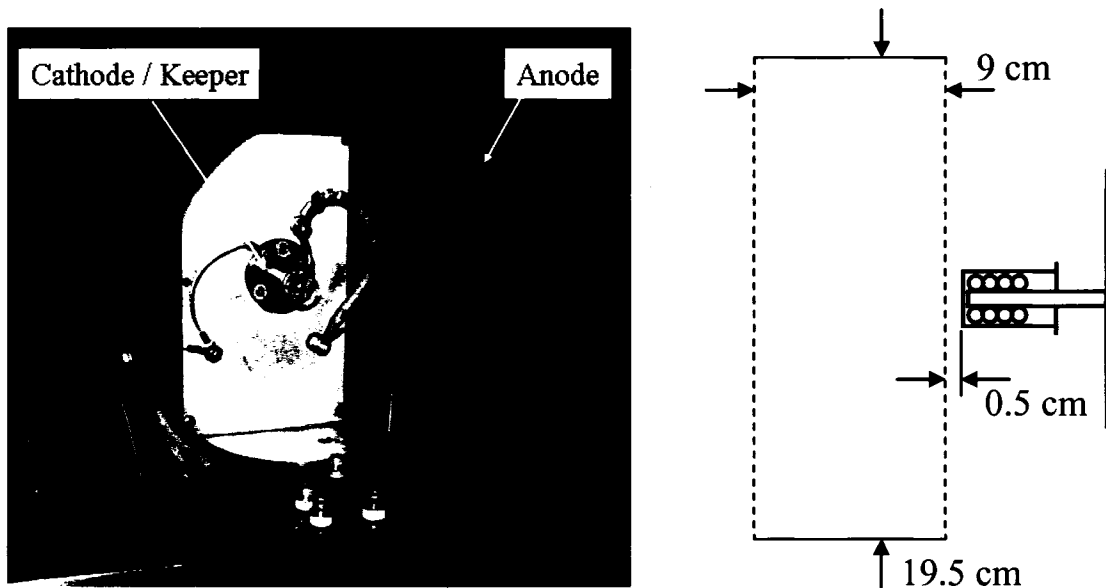

Figure 3.1 Open cathode (zero magnetic field) configuration. The anode was 19.5 cm in diameter and 9 cm in length.

3.1.1 Direct Measurements in Steady State

The first sets of measurements that will be discussed are from the emissive and triple Langmuir probes. Figure 3.2 shows a picture of plasma being produced in the open cathode configuration along with the emissive probe used to measure the plasma potential. Two linear stages were used to move the emissive probe. The radial stage moved the probe in a direction normal to the cathode centerline and the axial stage moved the probe in a direction along the cathode centerline.

40
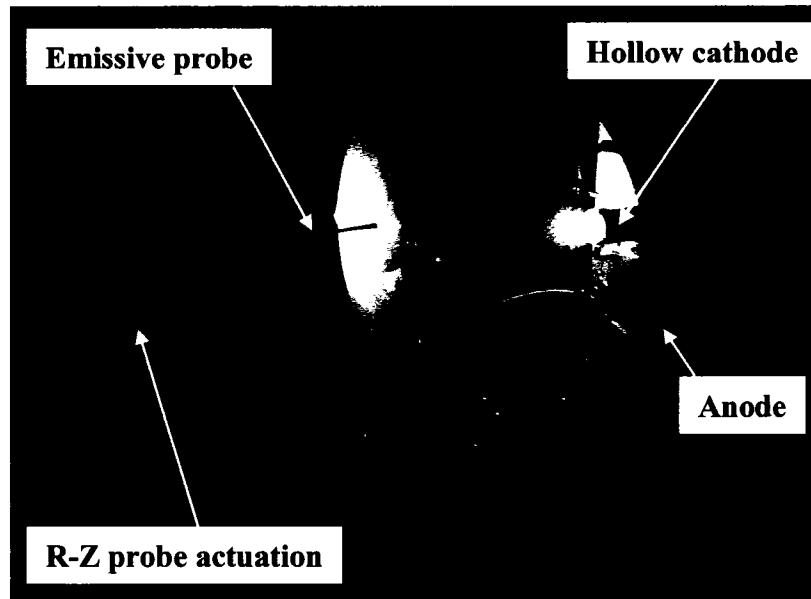
Figure 3.2 Experimental setup of the emissive probe used to measure plasma potential in the open hollow cathode configuration. The radial stage moved the probe in a direction normal to the cathode centerline and the axial stage moved the probe in a direction along the cathode centerline.

3.1.2 Emissive Probe Time-Averaged Profiles

Figure 3.3 shows potential profile plots taken with the emissive probe at each of the five operating conditions. The emissive probe was first moved to a few locations in the plasma and the filament heating current was varied to ensure that the probe was sufficiently hot to float near plasma potential. Once the proper heating current was selected, potential measurements were taken from z = 0.5 to 25.25 cm (from the keeper orifice location) and r = -7.5 to 7.5 cm (from the cathode centerline axis). All potentials are relative to cathode common which was connected to the vacuum chamber ground. In general, plasma potential ranged from about 16 to 50 V, with the potential dropping off as the emissive probe was moved farther away from the discharge region (axial distances greater than z ~ 10 cm). Also, the plasma potential decreased to low values when the probe was positioned close to the cathode, i.e., to within a centimeter from the

41

cathode/keeper orifice. The contour plots contained in Figure 3.3 show the time-averaged potential of the emissive probe. Temporal measurements were also made with the emissive probe (which will be described in subsequent sections) and strong oscillations were present in the plasma.

At conditions 1b (7.5 A) and 1c (11.25 A), there was a potential maximum, or potential hill, that existed just downstream of the hollow cathode where the peak potentials were above the cathode-to-anode voltage difference. As the discharge current was increased from 7.5 A to 15 A (condition 1b to 1c to 1d), the potential hill broadened and moved farther downstream of the cathode. Also, the peak potential magnitude decreased from the 7.5 A to 15 A condition.

At conditions 1d and 1e ($J_D = 15.0$ A), it was observed that an increase in flow rate caused the measured potentials to decrease significantly, especially along the cathode centerline. Conditions 1a and 1e are similar in that the measured potentials were well below the anode voltage, however, the potentials increased as the probe was moved closer to the anode wall (in regions not shown in Figure 3.3). This condition existed whenever the ratio of the flow rate-to-discharge current was large. It is likely that this ratio would vary with anode geometry and neutral pressure.

42
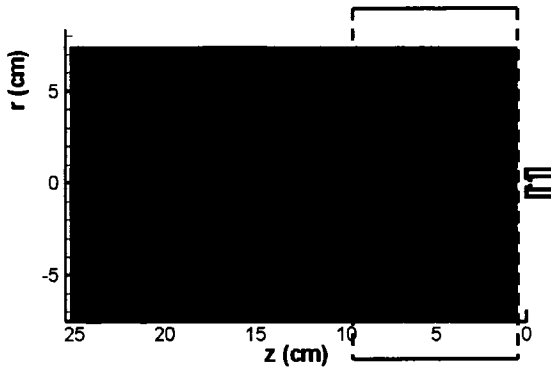
Figure 3.3a Condition 1a. Emissive probe potential measurements at J_D = 3.75 A, $\dot{m}$ = 7.6 sccm Xe, V_D = 32 V.
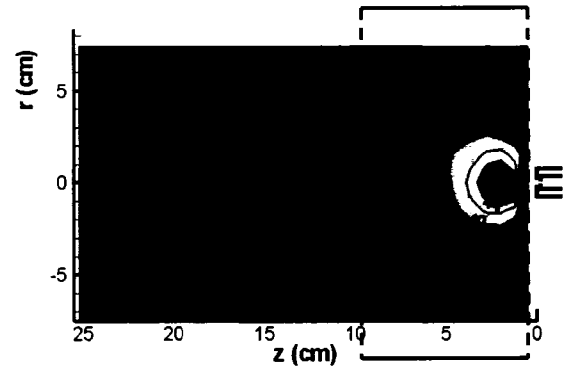

Figure 3.3b Condition 1b. Emissive probe potential measurements at J_D = 7.5 A, $\dot{m}$ = 7.6 sccm Xe, V_D = 33 V.
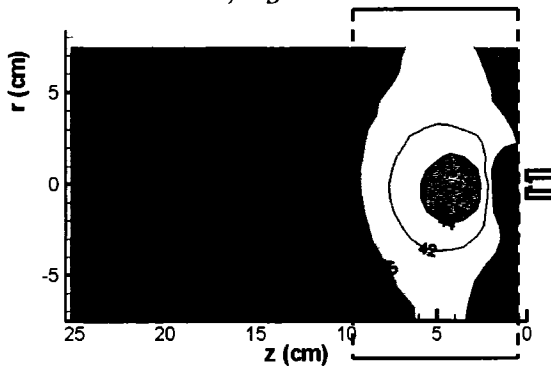

Figure 3.3c Condition 1c. Emissive probe potential measurements at J_D = 11.25 A, $\dot{m}$ = 7.6 sccm Xe, V_D = 34 V.
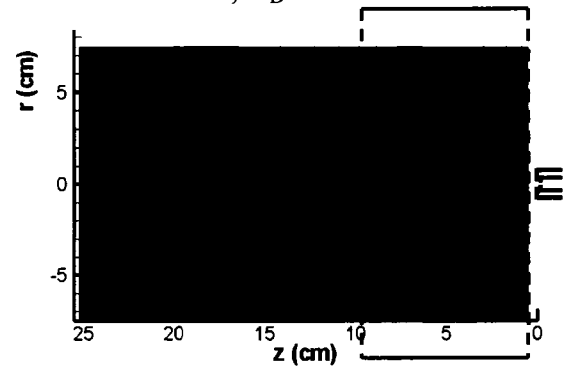

Figure 3.3d Condition 1d. Emissive probe potential measurements at J_D = 15.0 A, $\dot{m}$ = 7.6 sccm Xe, V_D = 33.5 V.
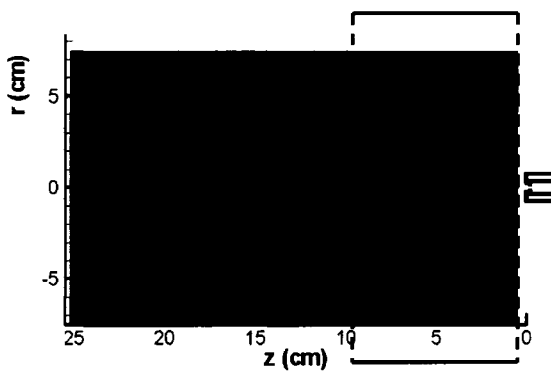

Figure 3.3e Condition 1e. Emissive probe potential measurements at J_D = 15.0 A, $\dot{m}$ = 9.6 sccm Xe, V_D = 41 V.

43
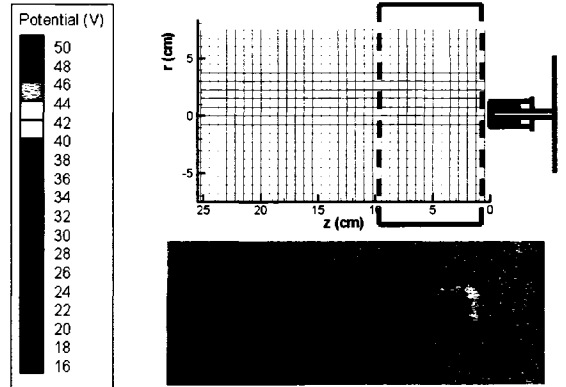
3.1.3 Triple Langmuir Probe Profiles

The triple Langmuir probe was mounted to two linear stages to allow for movement to different radial and axial locations within the plasma in a manner similar to the emissive probe. The triple Langmuir probe was used for comparison to the emissive probe potential measurements and to obtain estimates of the plasma density and electron temperature profiles. Figure 3.4 shows potential profile plots taken with the triple Langmuir probe at each of the five operating conditions from z = 0.5 to 25.25 cm (from the keeper orifice plate) and from r = -7.5 to 7.5 cm (from the cathode centerline axis). Like the emissive probe measurements, the potentials dropped off as the emissive probe was moved farther away from the discharge region (axial distances greater than z ~ 10 cm). Other similarities between the triple Langmuir probe and the emissive probe measurements included (a) higher potentials at the 7.5 A and 11.25 A conditions (1b and 1c) compared to the 3.75 and 15 A conditions (1a, 1d, and 1e), (b) potentials at conditions 1a and 1e were lower than the discharge voltage, and (c) the same potential well was observed directly in front of the cathode/keeper orifice.

Although similar in general characteristics, the triple probe measurements were not as symmetric about the cathode centerline. Some non-symmetry was also observed in the emissive probe measurements but not to the extent displayed by the triple probe from one side of the cathode to the other. It is thought that the non-symmetry is due to the orientation of the triple probe with respect to the cathode and anode where each of the triple electrodes were affecting the ion and electron currents flowing to the other electrodes. A similar effect is described by Tilley et al.[51] in regard to the orientation of the triple probe with respect to flowing ion currents that perturbed measurements of

44

plasma properties. In the data presented herein, no corrections were made to account for these effects. Also, some non-symmetry in the plasma was expected from imperfect placement of the anode centerline relative to the cathode.

The main differences in the emissive and triple Langmuir probe measurements included the location of the potential peaks. The triple probe showed the potential peaks occurring at locations farther downstream from the cathode compared to the emissive probe (5 to 10 cm for the triple probe compared to 1.5 to 7 cm for the emissive probe). Another difference was for the potential measurements at conditions 1a and 1e. While the emissive probe showed low potentials along the centerline axis, the triple probe showed a small potential peak similar to conditions 1b, 1c, and 1d, although the peak potential was still below the anode voltage.

There are some causes of measurement error with triple Langmuir probes, which are strongly associated with an assumption that the electron population is Maxwellian and that the probe electrode interactions with the plasma meet certain requirements[45,46,48,51]. The assumption of a Maxwellian population breaks down when there are significant numbers of primary electrons present (e.g., whenever primary to Maxwellian density ratios exceed 1%). This could be the case near the cathode where large numbers of primary electrons are being provided by the cathode. Also, low plasma density conditions cause the electrode sheaths to grow and interact with the other electrodes. For the open cathode conditions, the measured electron densities were in the 10^{13} to 10^{15} particles/m^3 range. In the lower part of this density range, the probe radius was comparable to the Debye length and therefore the thin sheath assumption may not have

45

been valid. However, to account for the sheath area, an effective sheath area correction was used in place of the probe electrode area[43].
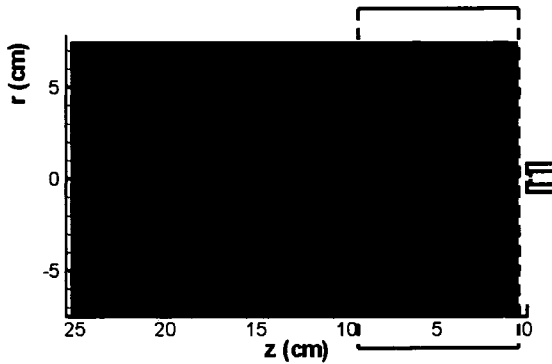

Figure 3.4a Condition 1a. Triple Langmuir probe potential measurements at $J_D = 3.75$ A, $\dot{m} = 7.6$ sccm Xe, $V_D = 32$ V.
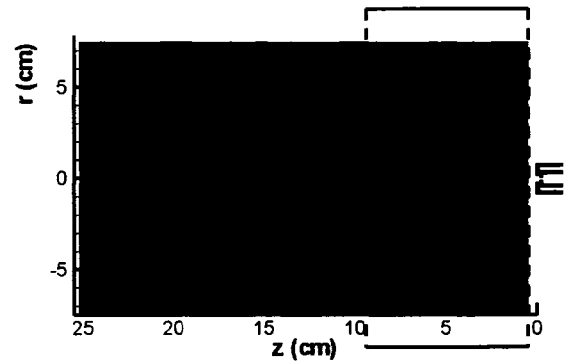

Figure 3.4b Condition 1b. Triple Langmuir probe potential measurements at $J_D = 7.5$ A, $\dot{m} = 7.6$ sccm Xe, $V_D = 33$ V.
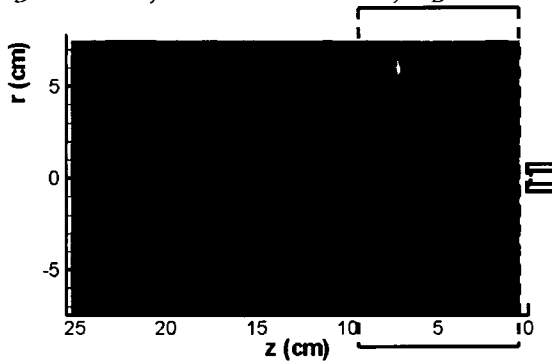

Figure 3.4c Condition 1c. Triple Langmuir probe potential measurements at $J_D = 11.25$ A, $\dot{m} = 7.6$ sccm Xe, $V_D = 34$ V.
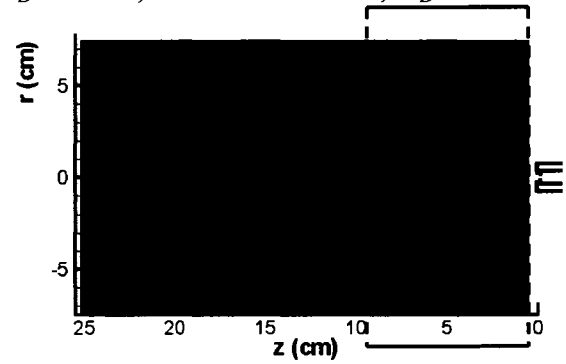

Figure 3.4d Condition 1d. Triple Langmuir probe potential measurements at $J_D = 15.0$ A, $\dot{m} = 7.6$ sccm Xe, $V_D = 33.5$ V.
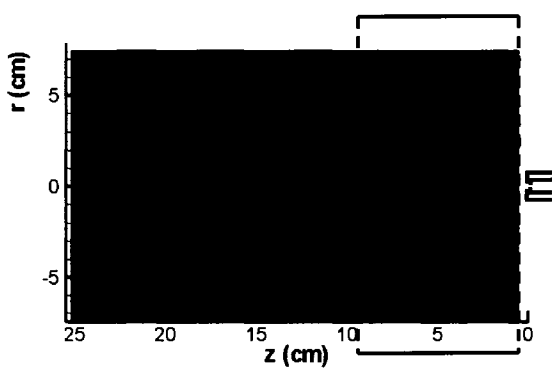

Figure 3.4e Condition 1e. Triple Langmuir probe potential measurements at $J_D = 15.0$ A, $\dot{m} = 9.6$ sccm Xe, $V_D = 41$ V.

46
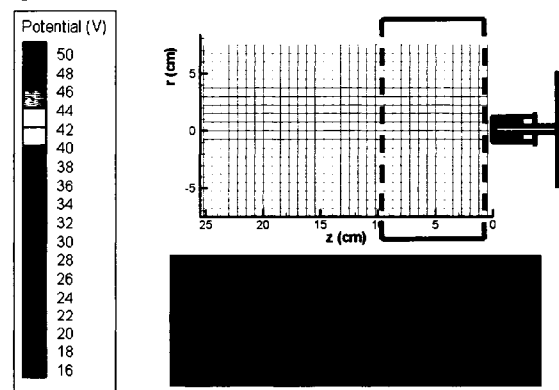
In addition to the plasma potential, the triple probe yields useful information about the electron temperature and electron density. Figure 3.5 shows contour plots of the calculated electron temperature and electron density at condition 1c. Note that the electron densities are plotted on a logarithmic scale. As expected, the electron density was highest near the cathode. The density in the majority of the discharge chamber was about two to three orders of magnitude lower than near the cathode. The electron temperatures were about 1.5 to 6.5 eV inside the discharge region, with the lowest electron temperatures occurring near the cathode and the highest in a band that connected to the anode.
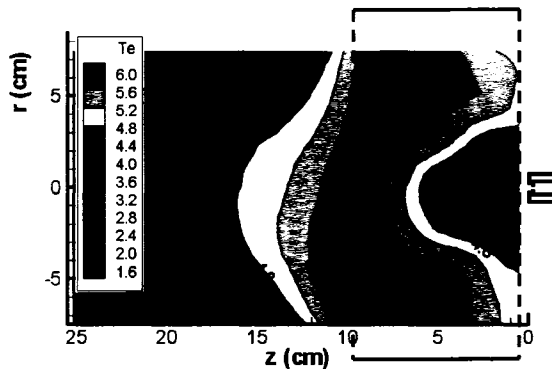

Figure 3.5a   Triple Langmuir probe electron temperature, T_e (eV), profile at condition 1c (J_D = 11.25 A, $\dot{m}$ = 7.6 sccm Xe, V_D = 34 V).
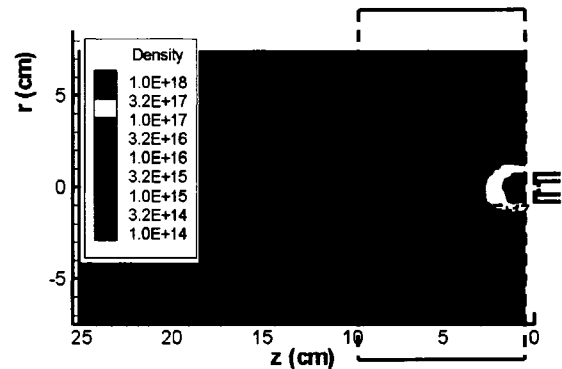
Figure 3.5b   Triple Langmuir probe electron density profile, n_e ($\#/m^3$), at condition 1c (J_D = 11.25 A, $\dot{m}$ = 7.6 sccm Xe, V_D = 34 V).

3.1.4 Emissive Probe Potential Oscillations

The emissive probe was used to measure the plasma potential as a function of time at many different locations. The typical procedure was to place the emissive probe at a desired location using the radial and axial positioning stages. Then, the emissive probe voltages were sampled at a rate of 1 MHz using a high speed data acquisition system. Some of the selected positions for the oscillation measurements are shown in

47

Figure 3.6. Radial locations of 0.5, 2.5, and 6.0 cm were chosen at axial locations of 0.5, 1.25, 2.0, 3.5, 5.0, 6.5, 9.5, 14.5, and 20.0 cm from the keeper plate.
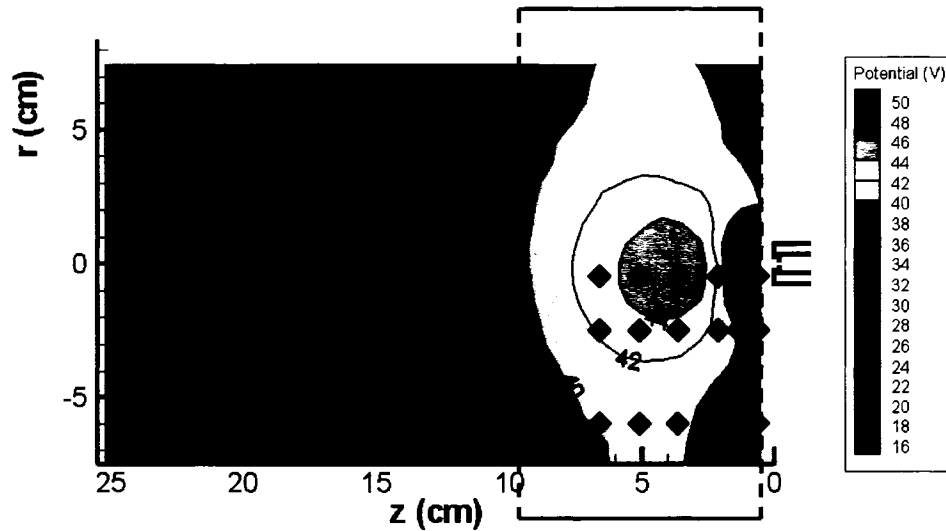

Figure 3.6 Selected points for potential oscillation measurements using the floating emissive probe. The contour plot shows the time-averaged emissive probe potentials (condition 1c shown at $J_D = 11.25$ A, $\dot{m} = 7.6$ sccm Xe, $V_D = 34$ V).

Figure 3.7 shows typical oscillation measurements at axial locations of 0.5, 2.0, 5.0, 9.5, and 20.0 cm from the keeper for operating condition 1c. The largest potential oscillations were observed near the cathode centerline from about $z = 1$ to $z = 6$ cm from the cathode. At the 1c operating condition, the oscillations at $z = 2.0$ cm and $r = 0.5$ cm (red) varied from 20 V to over 85 V, which was near the maximum potential that the emissive probe circuitry was capable of measuring.

It is unfortunate in terms of erosion due to sputtering that the largest potential oscillations were observed to occur near the cathode. Ions produced at higher potentials would gain more energy as they fall toward lower potentials and would have a much greater ability to sputter erode surfaces such as the cathode and keeper surfaces. Also, the ion density, which is relatively high near the cathode, would result in higher flux energetic ions striking the cathode and keeper.

48
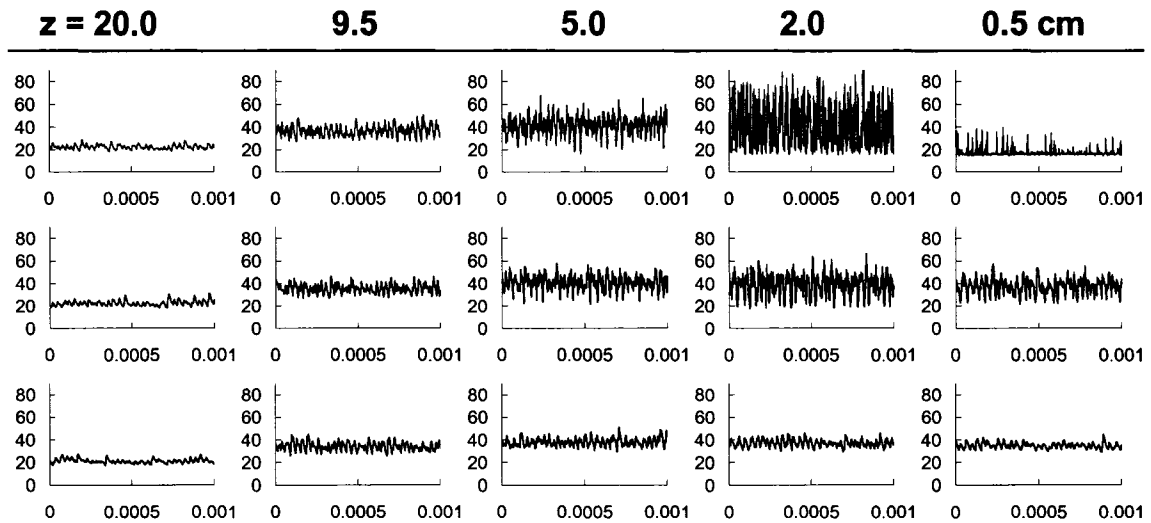
Figure 3.7 Plasma potential oscillation measurements for condition 1c (J_D = 11.25 A, $\dot{m}$ = 7.6 sccm Xe, V_D = 34 V) at r = 0.5, 2.5, and 6.0 cm and z = 0.5, 2.0, 5.0, 9.5, and 20.0 cm from the keeper. The y-axis is plasma potential (0 to 90 V) and the x-axis is time (s). The largest potential oscillations were seen near the cathode centerline from about z = 1 to z = 6 cm from the cathode.

Figure 3.8 shows a comparison of the time-averaged (or steady state) potentials at conditions 1b, 1c, and 1d. The discharge current was varied from 7.5 to 15 A while the cathode flow rate was held constant (7.6 sccm Xe). The discharge voltage was about the same for all three conditions (33 V, 34 V, and 33.5 V). The diamonds show the positions of selected oscillation measurements at a radial location of 0.5 cm. Figure 3.9 shows the plasma potential oscillations at each of the selected points in Figure 3.8. Similar to the time-averaged potential profile trend, as the discharge current was increased from 7.5 A (1b) to 15 A (1d), the location of the largest potential oscillations moved farther downstream from the cathode (1.25 to 3.5 cm). However, note that the location of the time-averaged potential peak did not correspond to the location of the maximum oscillation amplitude. The largest amplitude oscillations were observed at locations between the cathode and time-averaged potential peaks.

49
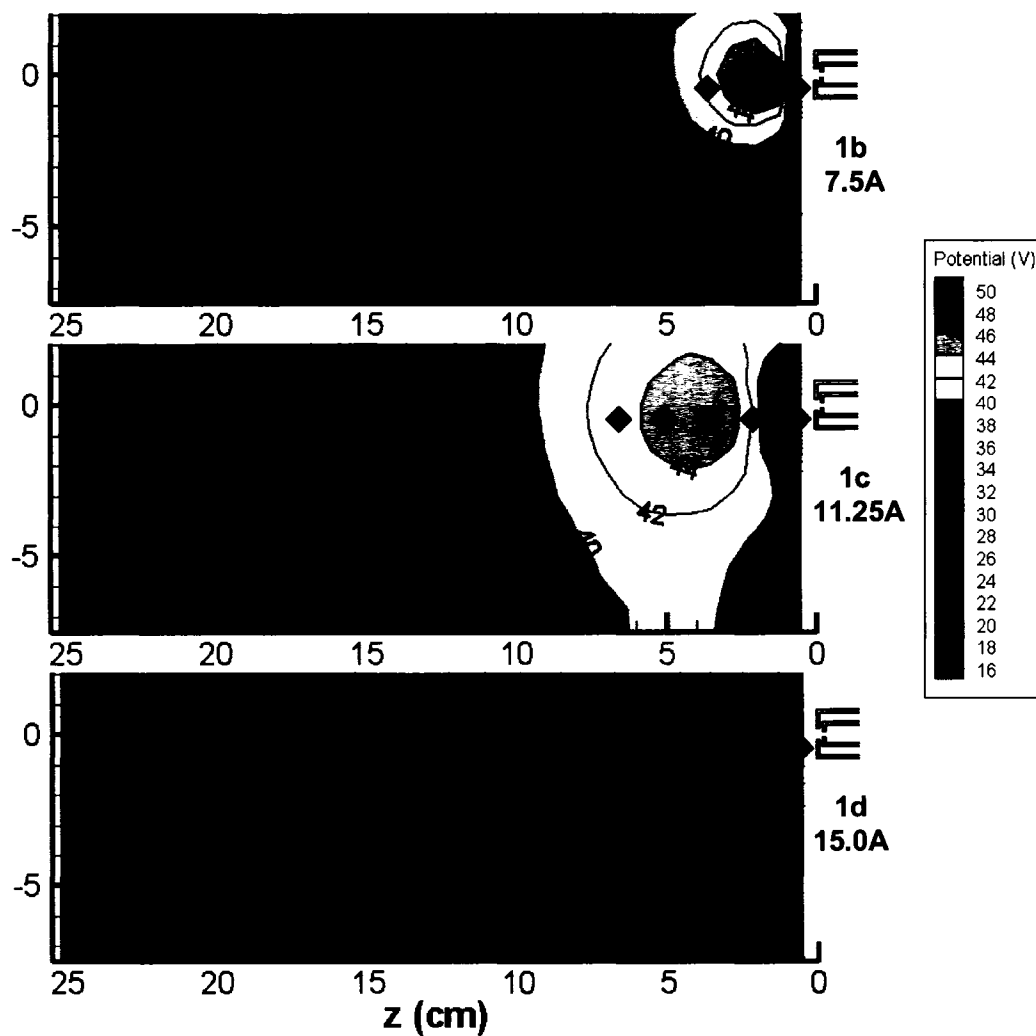
Figure 3.8 Emissive probe measurements for conditions 1b, 1c, and 1d. The discharge current was varied from 7.5 to 15 A while the cathode flow rate was held constant (7.6 sccm Xe). The discharge voltage was about the same for all three conditions (33 V, 34 V, and 33.5 V). The diamonds show the positions of the emissive oscillation measurements (discussed in Figure 3.9).

50

z = 6.5	5.0	3.5	2.0	1.25	0.5 cm
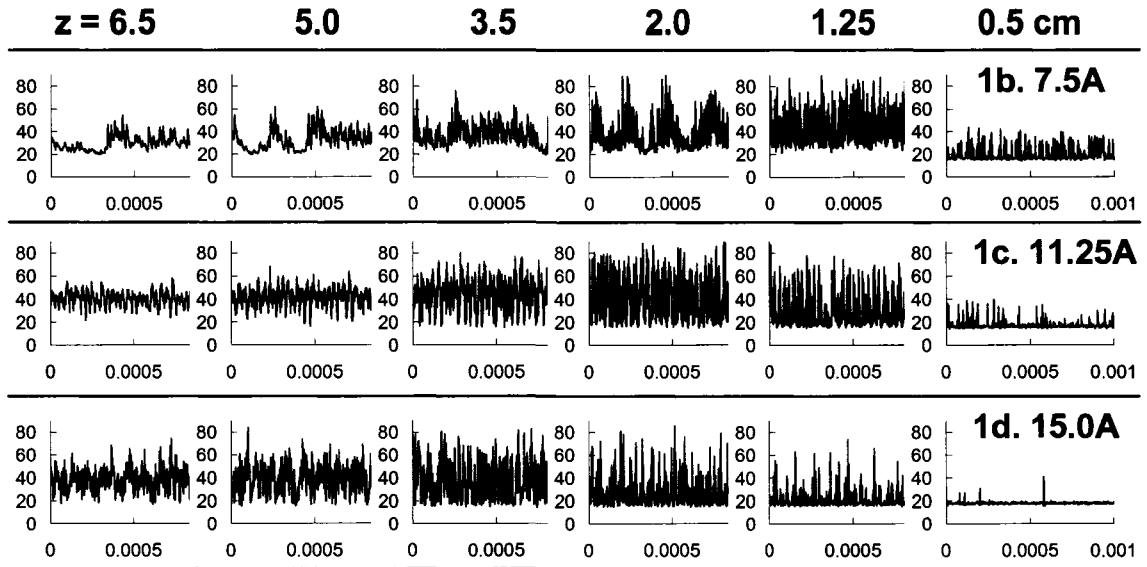
Figure 3.9 Emissive probe oscillation measurements at r = 0.5 cm for conditions 1b, 1c, and 1d. The y-axis is plasma potential (0 to 90 V) and the x-axis is time (s). As the discharge current was increased from 7.5 A (1b) to 15 A (1d), the location of the largest potential oscillations moved away from the cathode (from z = 1.25 to z = 3.5 cm).

Conditions 1a and 1e had much lower amplitude oscillations compared to the oscillations observed at conditions 1b, 1c, and 1d. This is more clearly evident in Figure 3.10 for selected axial locations at a radius of 0.5 cm. In general, the magnitude of the potential oscillations decreased when the flow rate-to-discharge current ratio was large.

51
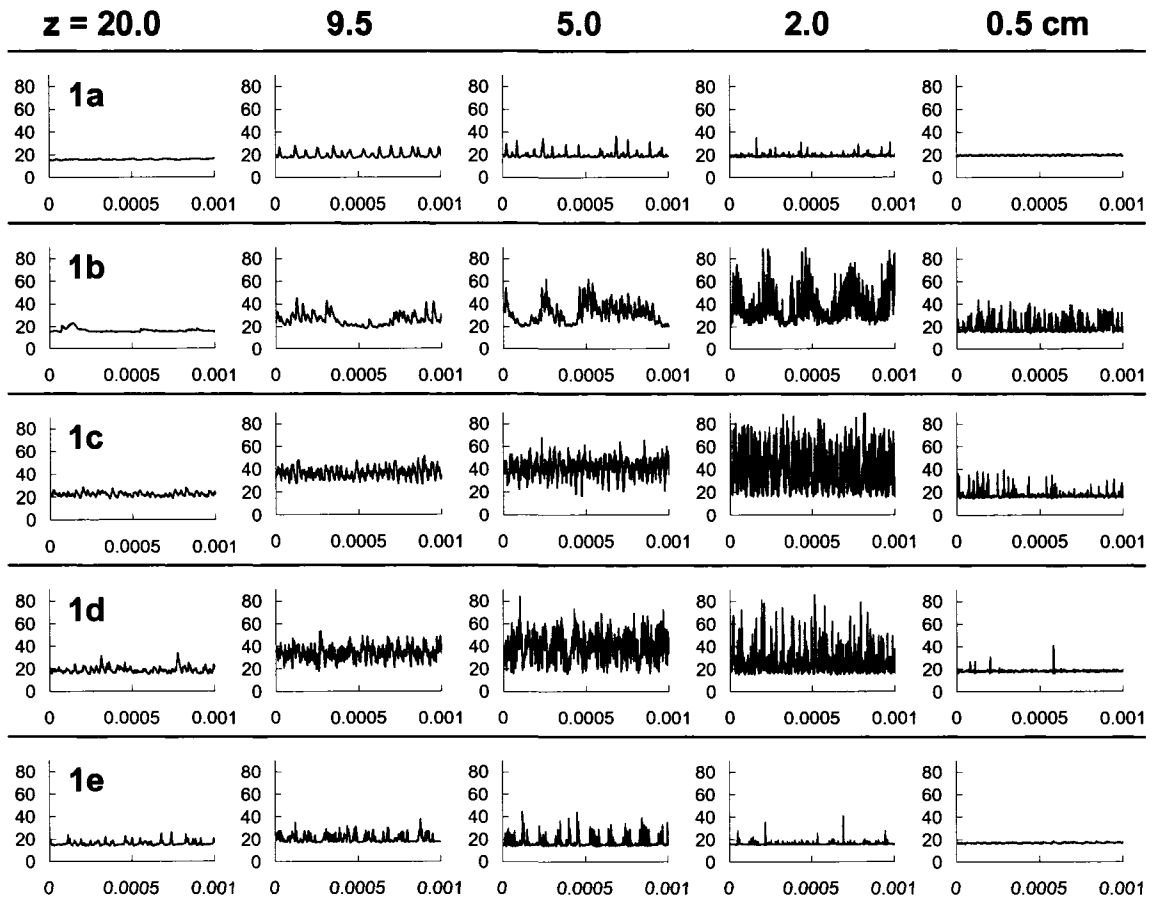
Figure 3.10   Comparison of potential waveforms for conditions 1a-1e at five axial locations (at fixed r = 0.5 cm).   The y-axis is plasma potential (0 to 90 V) and the x-axis is time (s).   The magnitude of the potential oscillations decreased when the flow rate was high relative to the discharge current (as at conditions 1a and 1e).

3.1.5   Electrostatic Analyzer and ExB (ESA_ExB) Remote Measurements

The combined ESA_ExB probe was used to investigate the discharge plasma produced in the open cathode configuration (case 1).   Figure 3.11 contains ion energy distribution functions (IEDFs) with the corresponding doubles-to-singles ratio for each of the five operating conditions.   The entrance to the ESA was located at an axial distance of 45 cm from the keeper orifice plate.   Each of the three IEDFs shown in Figure 3.11 correspond to a radial location of the ESA relative to the cathode of r = 0, -3, and -6 cm

52

as indicated in the sketch in Figure 3.11f. The doubles-to-singles ratio data correspond to a radial location of 0 cm (r = 0 cm).

Figure 3.11 and Figure 3.12 show how the IEDF changed with discharge current. As the discharge current was varied from 3.75 to 15 A, the relative number of higher energy ions increased, especially in the 50 to 150 eV energy range. A main ion signal was present in all cases that had a most probable energy near the discharge voltage. Comparisons between the remote measurements to the direct measurements from the emissive and triple Langmuir probes suggest that the potential oscillations likely contribute to the production of ions with energies above the cathode-to-anode potential difference. Specifically, the most energetic ions would be detected at the remote probe location whenever ions are produced at a maximum plasma potential that fall from this point and accelerate toward the remote probe. The energetic ions, both inferred from the high emissive probe potential oscillations and measured using the remotely located ESA, would have a greater ability to sputter erode discharge chamber components. Other processes could result in high ion energies such as multiple charge exchange and re-ionization reactions, however, these reactions would have to occur in phase with the spatial and temporal potential field to produce some ions with high energies[32]. Although possible, resonant reaction processes are considered unlikely to occur at rates high enough to be detected in the low neutral pressure environment that exists in the case 1 configuration.
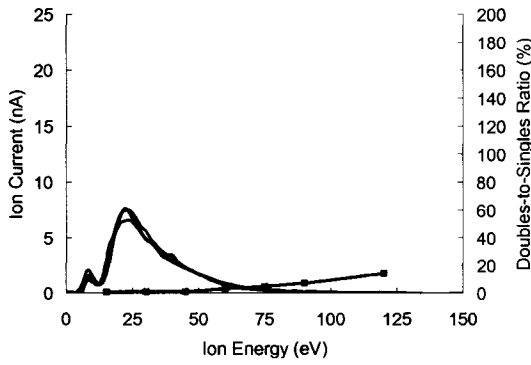
Figure 3.11a Condition 1a. ESA_ExB probe measurements at J_D = 3.75 A, $\dot{m}$ = 7.6 sccm Xe, V_D = 32 V.
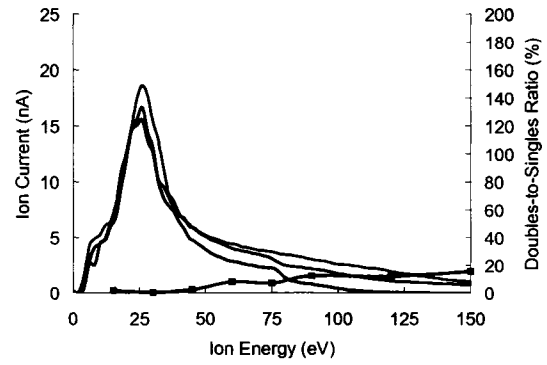
Figure 3.11b Condition 1b. ESA_ExB probe measurements at J_D = 7.5 A, $\dot{m}$ = 7.6 sccm Xe, V_D = 33 V.
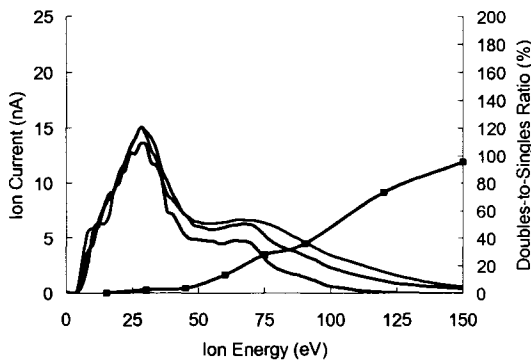
Figure 3.11c Condition 1c. ESA_ExB probe measurements at J_D = 11.25 A, $\dot{m}$ = 7.6 sccm Xe, V_D = 34 V.
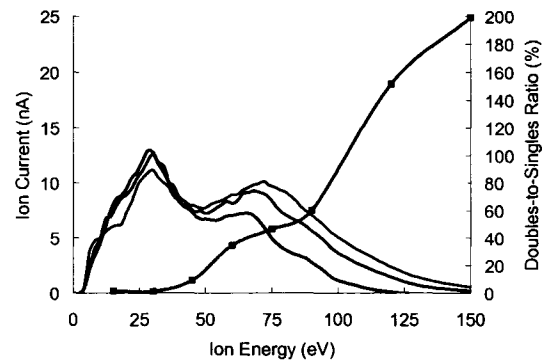
Figure 3.11d Condition 1d. ESA_ExB probe measurements at J_D = 15.0 A, $\dot{m}$ = 7.6 sccm Xe, V_D = 33.5 V.
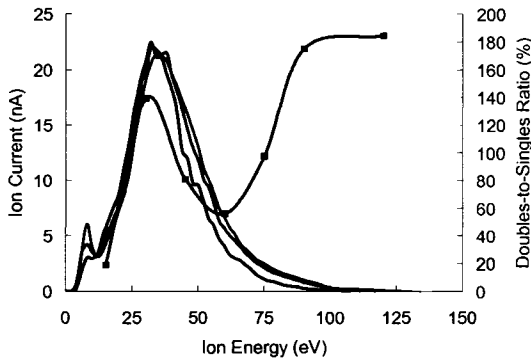
Figure 3.11e Condition 1e. ESA_ExB probe measurements at J_D = 15.0 A, $\dot{m}$ = 9.6 sccm Xe, V_D = 41 V.
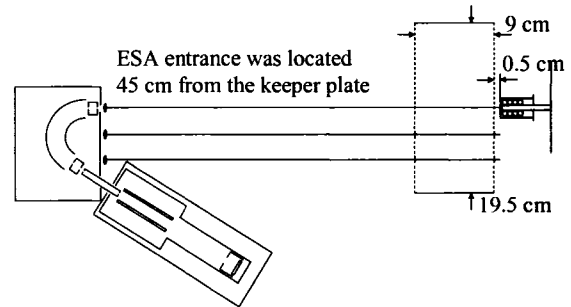
Figure 3.11f Location of the ESA relative to the cathode for each measured IEDF (red = 0 cm, blue = -3 cm, black = -6 cm). The doubles-to-singles ratio was measured on the cathode centerline (r = 0 cm).

ESA entrance was located 45 cm from the keeper plate

9 cm

0.5 cm

19.5 cm

54

Another effect was that as the discharge current was increased, the doubles-to-singles ratio increased (at each of the energies selected for charge state characterization) as shown in Figure 3.11 and Figure 3.13. It is interesting to note that condition 1e had a different trend for the doubles-to-singles ratios compared to the other four conditions. While there were not many doubly charged ions at lower energies for conditions 1a-1d, there were significant numbers of doubly charged ions at condition 1e. Direct measurements of condition 1e did not show excessive DC or AC potentials (see Figure 3.3e, Figure 3.4e, and Figure 3.10), and so the excessive production of doubles at condition 1e at low energies may represent a mode change in the discharge from conditions 1a through 1d.

Consider the results from both the ESA section of the probe and the ExB section. Measurements using the ESA showed that there were many energetic ions produced in the case 1 configuration, especially at conditions 1c and 1d (see Figure 3.12). At high ion energies, the ExB section of the probe showed that the doubles-to-singles ratio increased with ion energy (see Figure 3.13). The considerable portion of higher energy ions that were also doubly charged further increases the sputtering capability of these ions. Therefore, it is especially important to operate in a configuration which limits the production of energetic ions, since the energetic ion populations are comprised of larger fractions of multiply charged ions.

55
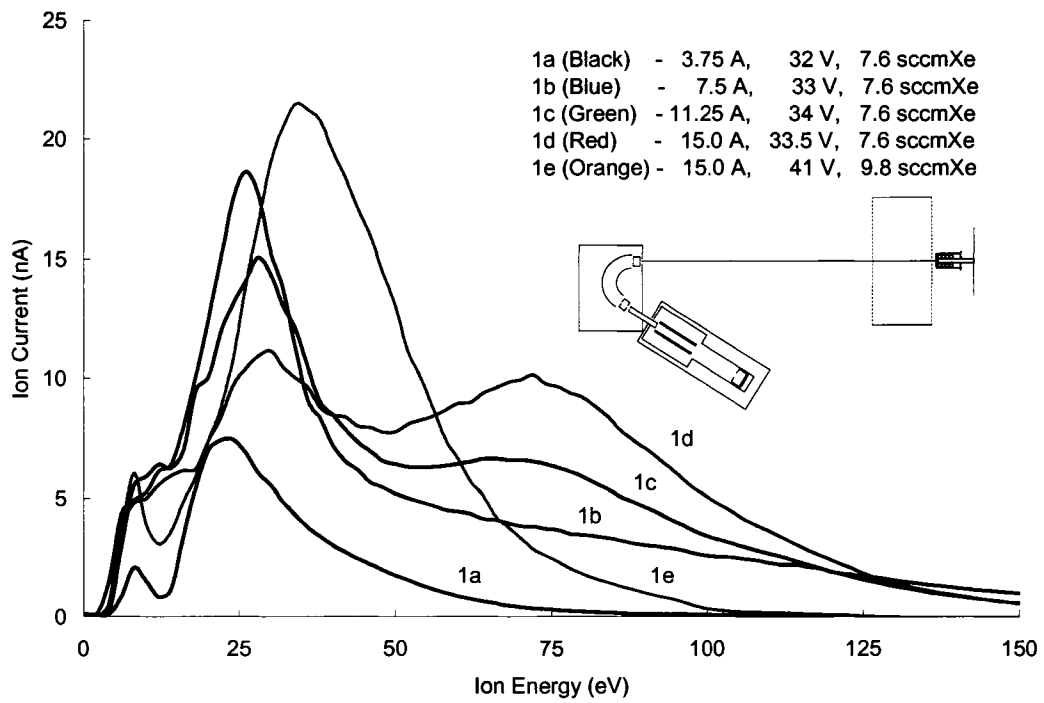
Figure 3.12 ESA traces taken at operating conditions 1a-1e. The ESA was located about 45 cm from the keeper on the cathode centerline (r = 0 cm).
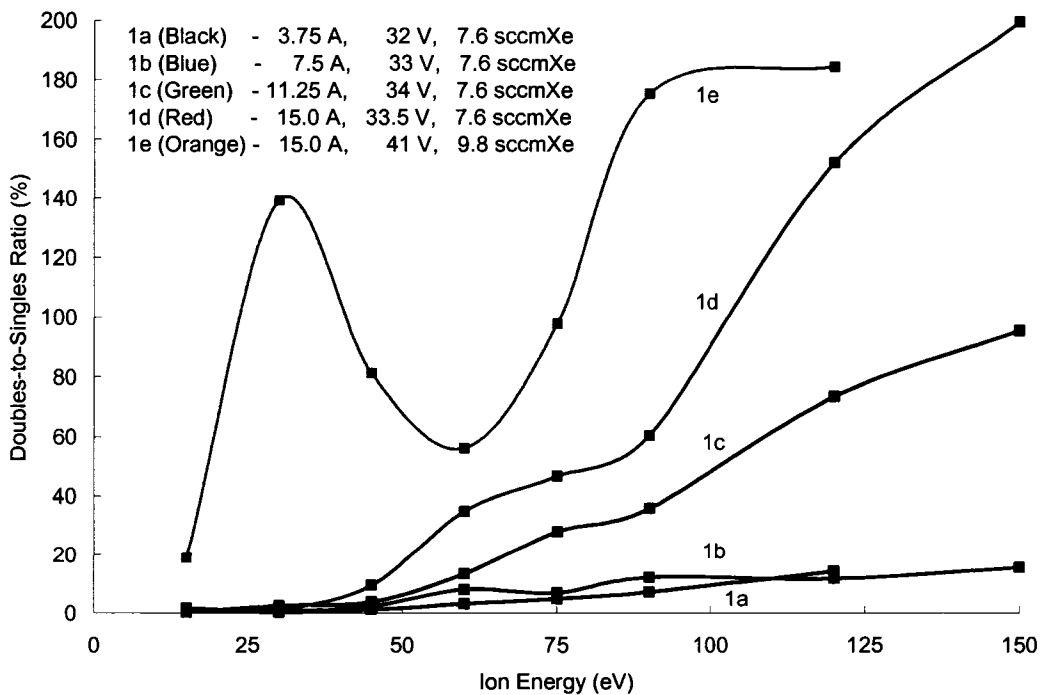

Figure 3.13 Measured doubles-to-singles ratio at operating conditions 1a-1e. The ESA was located about 45 cm from the keeper on the cathode centerline (r = 0 cm).

56

3.2 Case 2: Prototype NSTAR Discharge Chamber Configuration

Results will be presented for six cathode operating conditions in the prototype NSTAR discharge configuration, as displayed in Figure 3.14 and Figure 3.15. Figure 3.15a shows the discharge plasma as viewed by a remotely located probe located at a zenith angle of 0 degrees and Figure 3.15b shows the plasma as viewed by a probe positioned at a zenith angle of 90 degrees. Compared to the discharge setup discussed in case 1, this configuration was intended to produce plasma similar to that found within the discharge chamber of an ion thruster. Three magnet rings were used to produce a magnetic field to better confine the electrons in the plasma. A description of the magnetic field is contained in Appendix A.

Table 3.2 shows the operating conditions for case 2. Three discharge conditions (2a, 2b, and 2d) were chosen to operate over a range used in the NSTAR ion engine. In addition, the discharge current was 18 A in conditions 2e and 2f to investigate the effects of increased discharge current. The sixth operating point, condition 2c, was chosen to investigate the effect of increased xenon gas flow compared to condition 2b. For most of the operating conditions, except for conditions 2c and 2f, the flow rate was chosen to set the discharge voltage near 25 V. The heater and keeper power supplies were turned 'off' for all of the tests.

Table 3.2 – Test conditions for case 2.

Case	Condition	J_D (A)	V_D (V)	Flow (sccm Xe)	P_t ($\times 10^{-5}$ Torr)
2 Prototype NSTAR	2a	4.5	24.8	3.3	1.7
	2b	8.3	24.9	6.1	2.8
	2c	8.3	22.5	13.0	5.6
	2d	13.0	25.2	13.1	5.7
	2e	18.0	24.9	13.0	5.6
	2f	18.0	36.0	8.3	3.9

57

At each of the operating conditions, plasma measurements were made with the emissive probe, triple Langmuir probe, and the ESA_ExB probe. Each probe could be mounted to two linear stages to allow for movement to different locations within the plasma. A radial motion stage moved the probes in a direction normal to the cathode centerline and an axial stage moved the probe in a direction parallel to the cathode centerline (similar to the case 1 configuration study).
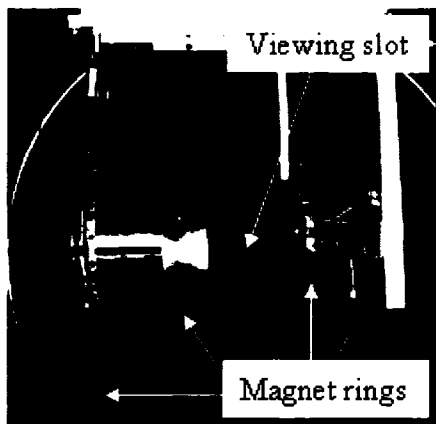

Figure 3.14a Side view of the prototype NSTAR discharge chamber.
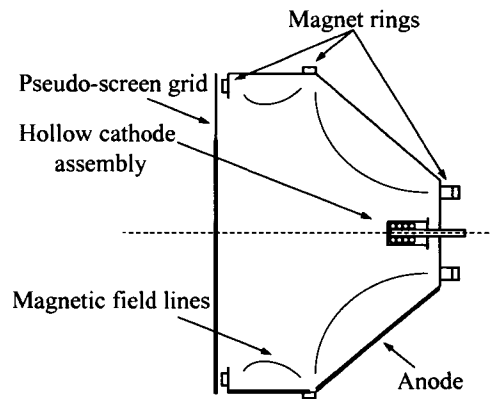

Figure 3.14b Discharge chamber schematic.
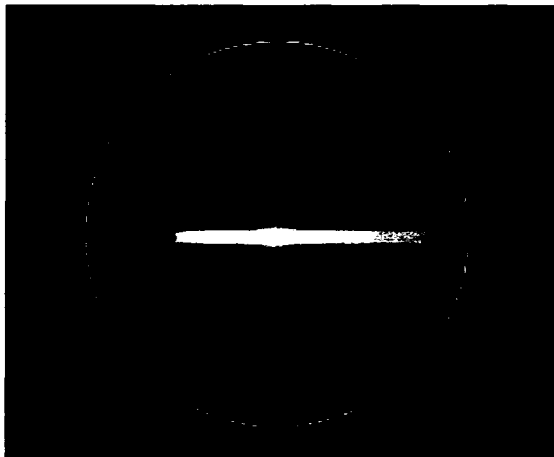
Figure 3.15a Prototype NSTAR discharge chamber in operation (0 degree view).
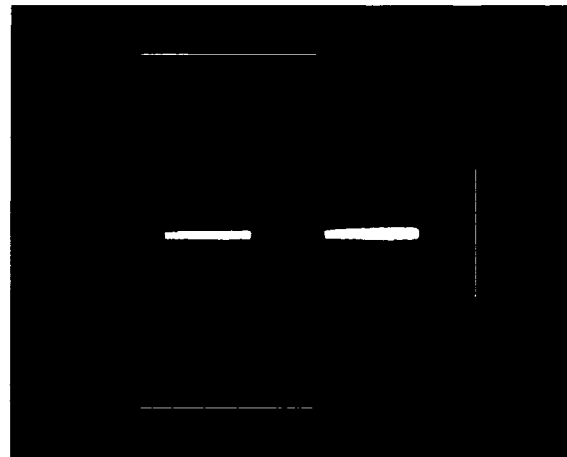
Figure 3.15b Prototype NSTAR discharge chamber in operation (90 degree view).

58

3.2.1 Emissive Probe Time-Averaged Profiles

Figure 3.16 shows time-averaged potential profile plots taken with the emissive probe at each of the six operating conditions. Measurements were taken from z = 0.5 to 29.0 cm from the keeper orifice and r = -29.5 to 5.0 cm from the cathode centerline axis. The plasma potential in the discharge chamber region ranged between 16 and 36 V. The plasma potential dropped off as the emissive probe was moved outside of the discharge region (axial distances greater than z ~ 10.5 cm), however, plasma potential near the cathode centerline remained slightly higher than the potentials off centerline at locations just outside of the pseudo-screen grid. Plasma potential dropped as the probe was moved close to the cathode, to within a couple of centimeters of radius from the cathode/keeper orifice. For the mapped region, the time-averaged potentials were highest near the anode (measured in the viewing slot cut in the conical portion of the anode). The plasma potentials dropped off gradually at radial positions outside of the anode. An outline of the discharge chamber is presented in all contour plots to help guide the eye of the reader.

It is noted that there was some undesirable coupling of the discharge plasma to the outside of the anode wall to the magnet rings, especially when operating at high discharge currents. This was due to the viewing slot cut in the anode that allowed plasma to form outside of the discharge chamber. It is reasonable to assume that the fraction of discharge current carried to the outside of the discharge chamber was small compared to the fraction of current flowing to the interior wall of the discharge chamber since both the plasma density and accessible coupling area were a couple orders of magnitude higher inside the discharge chamber.

59

For conditions 2a, 2b, 2d, and 2e, the xenon flow rate was adjusted so that the discharge voltage was near 25 V. Similar DC plasma potential contour plots were observed for these conditions even though the discharge current was varied over a range from 4.5 to 18.0 A.

Condition 2c was operated at a discharge current of 8.3 A, similar to condition 2b, but at a higher flow rate (13 sccm xenon) similar to conditions 2d and 2e. The increased xenon flow reduced the discharge voltage to 22.5 V, and, correspondingly, the emissive probe measured potentials slightly lower at this condition.

Condition 2f was operated at a discharge current of 18.0 A, similar to condition 2e, but at a lower flow rate. The decreased xenon flow caused the discharge voltage to increase to 36.0 V. Corresponding to the increased discharge voltage, the emissive probe measured higher plasma potentials from 30 to 37 V inside the discharge region.
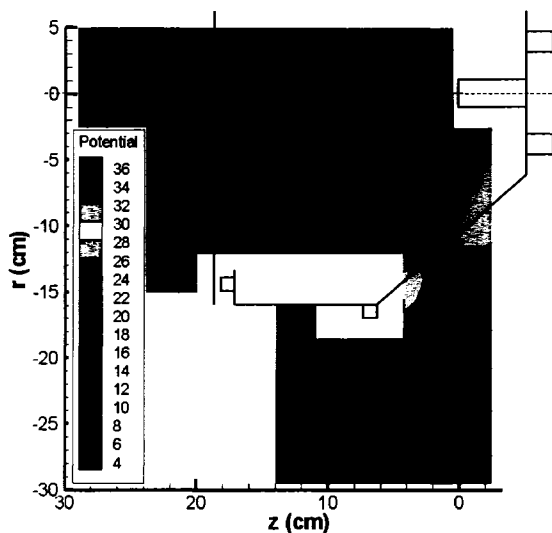

Figure 3.16a Condition 2a. Emissive probe potential measurements at J_D = 4.5 A, $\dot{m}$ = 3.3 sccm Xe, V_D = 24.8 V.
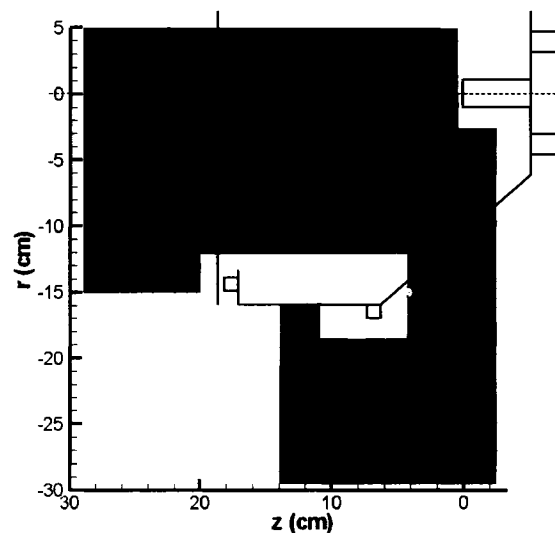
Figure 3.16b Condition 2b. Emissive probe potential measurements at J_D = 8.3 A, $\dot{m}$ = 6.1 sccm Xe, V_D = 24.9 V.

60
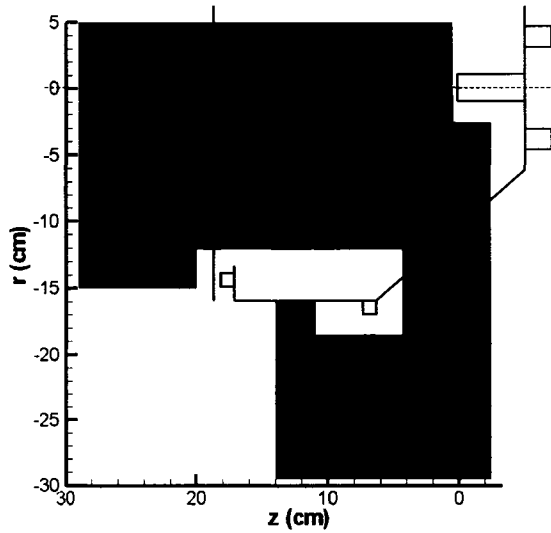
Figure 3.16c Condition 2c. Emissive probe potential measurements at J_D = 8.3 A, $\dot{m}$ = 13.0 sccm Xe, V_D = 22.5 V.
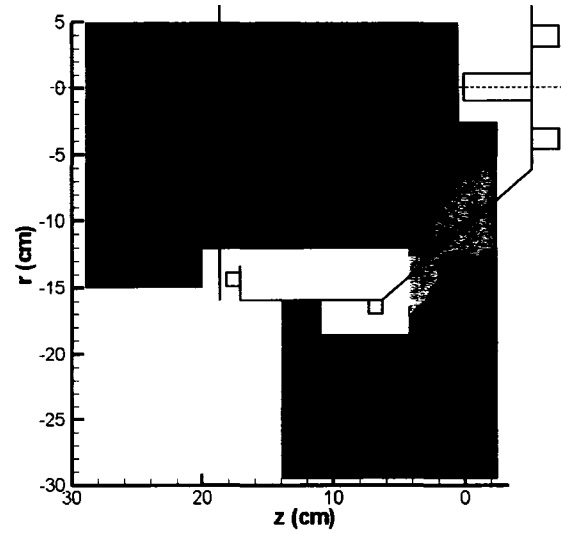
Figure 3.16d Condition 2d. Emissive probe potential measurements at J_D = 13.0 A, $\dot{m}$ = 13.1 sccm Xe, V_D = 25.2 V.
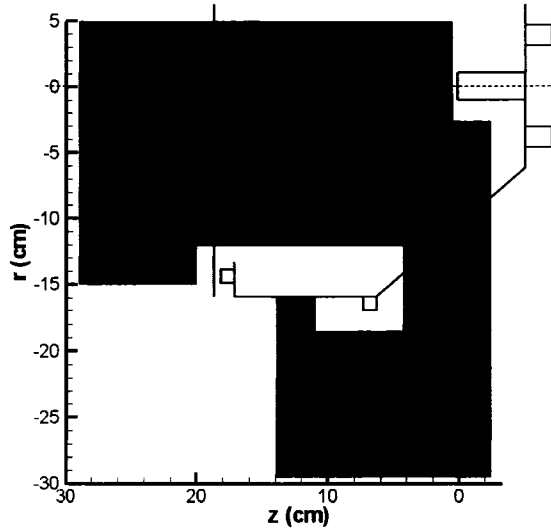
Figure 3.16e Condition 2e. Emissive probe potential measurements at J_D = 18.0 A, $\dot{m}$ = 13.0 sccm Xe, V_D = 24.9 V.
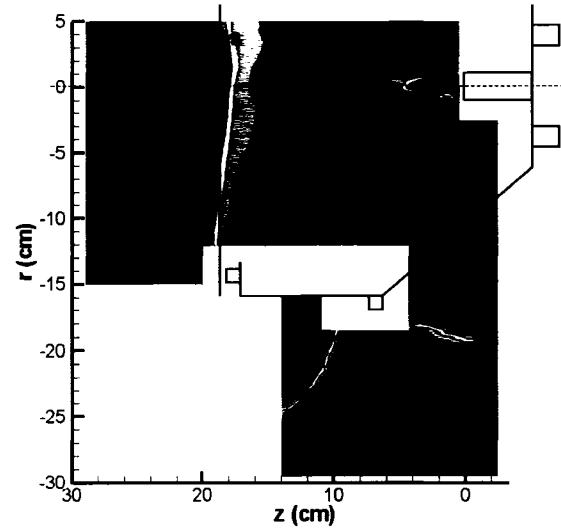
Figure 3.16f Condition 2f. Emissive probe potential measurements at J_D = 18.0 A, $\dot{m}$ = 8.3 sccm Xe, V_D = 36.0 V.

3.2.2 Triple Langmuir Probe Profiles

Figure 3.17 shows potential profile plots taken with the triple Langmuir probe. Measurements were taken at the same points as the emissive probe from z = 0.5 to 29.0 cm from the keeper orifice plate and from r = -29.5 to 5.0 cm from the cathode centerline axis. Low plasma potential was observed near the cathode/keeper assembly and the

61

plasma potential was also low as the probe was moved outside of the discharge chamber. The highest potentials were observed near the anode walls and at off axis locations near the cathode.

The triple probe plasma potential was higher than the emissive probe at most locations, especially for condition 2f. Note that the potential scale on the contour plots is different for the triple probe than the emissive probe. The potentials ranged from a low of 4 V up to a maximum of 52 V inside the discharge chamber. At condition 2f, the potentials went well above 52 V at some locations near the anode and just outside the anode. As mentioned earlier, the triple probe is prone to errors and may have been affected by electrode shadowing and sheath interactions at the low plasma densities expected within the anode slot and in the regions outside of the discharge chamber.

Both the triple Langmuir probe and the emissive probe indicated that the potentials at locations just outside of the pseudo-screen grid remained slightly higher near the chamber centerline compared to the potentials off centerline.
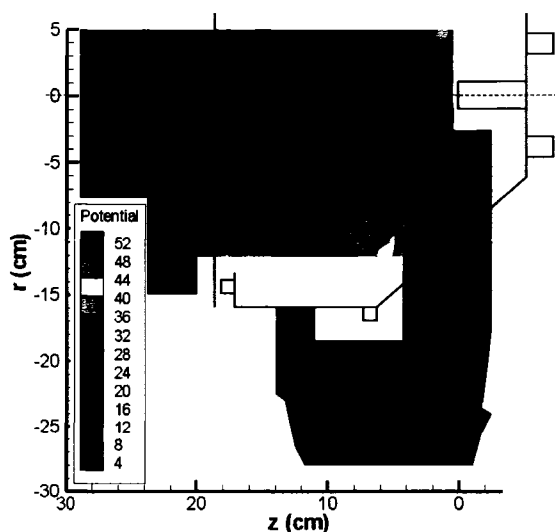
Figure 3.17a Condition 2a. Triple probe potential measurements at J_D = 4.5 A, $\dot{m}$ = 3.3 sccm Xe, V_D = 24.8 V.
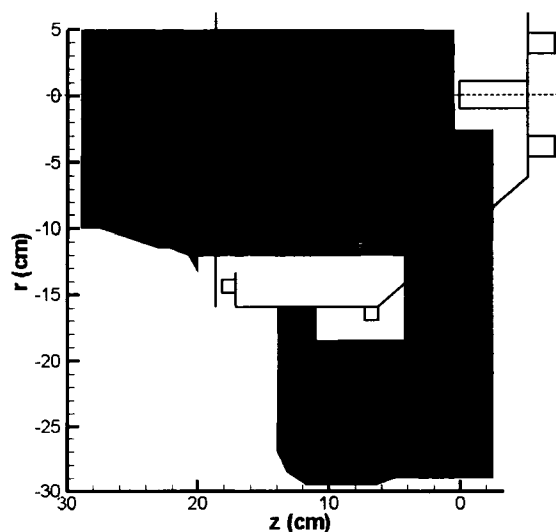
Figure 3.17b Condition 2b. Triple probe potential measurements at J_D = 8.3 A, $\dot{m}$ = 6.1 sccm Xe, V_D = 24.9 V.

62
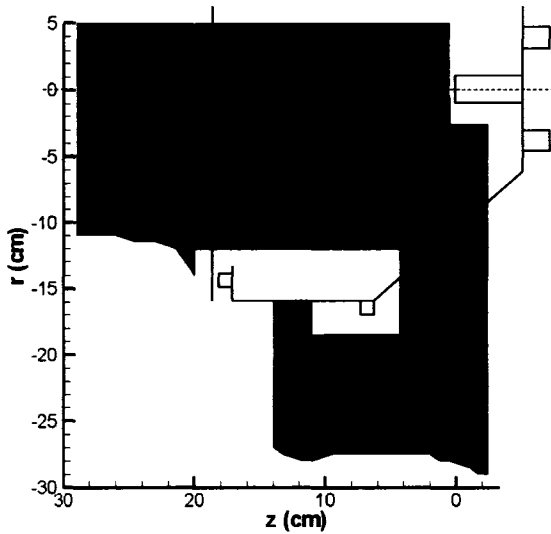
Figure 3.17c Condition 2c. Triple probe potential measurements at J_D = 8.3 A, $\dot{m}$ = 13.0 sccm Xe, V_D = 22.5 V.
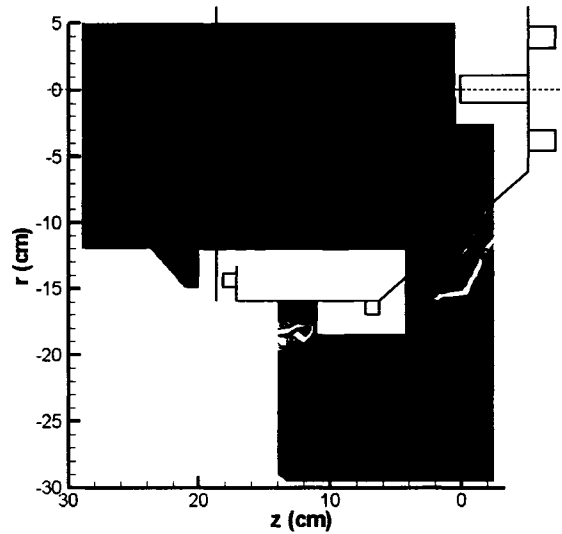
Figure 3.17d Condition 2d. Triple probe potential measurements at J_D = 13.0 A, $\dot{m}$ = 13.1 sccm Xe, V_D = 25.2 V.
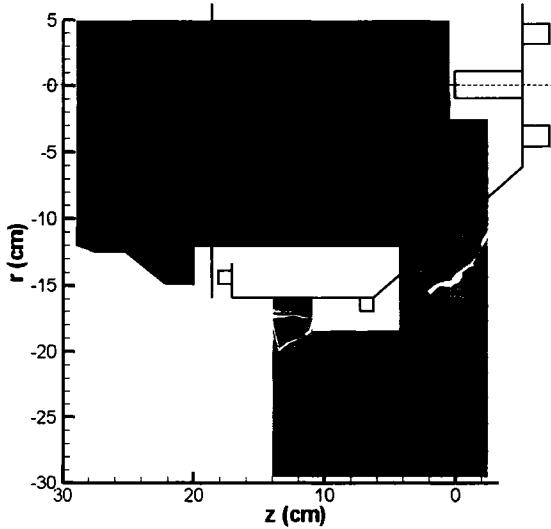
Figure 3.17e Condition 2e. Triple probe potential measurements at J_D = 18.0 A, $\dot{m}$ = 13.0 sccm Xe, V_D = 24.9 V.
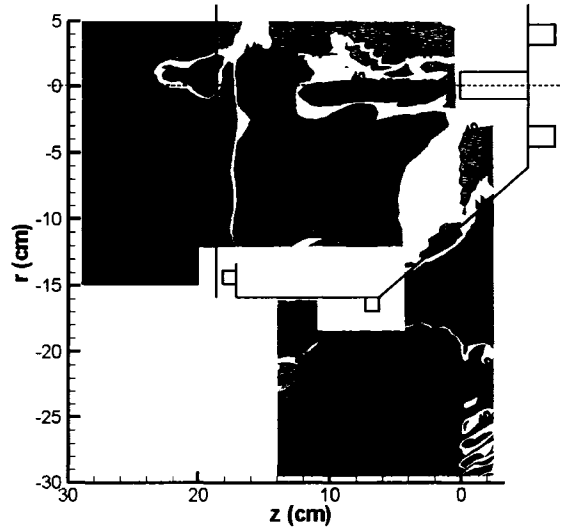
Figure 3.17f Condition 2f. Triple probe potential measurements at J_D = 18.0 A, $\dot{m}$ = 8.3 sccm Xe, V_D = 36.0 V.

Consistent with visual observation and the emissive potential measurements, the triple probe indicated that some plasma was being produced outside the anode region.

In addition to plasma potential, the triple probe yields information about the electron temperature and electron density. Figure 3.18 shows contour plots of the plasma potential, floating potential, electron temperature, and electron density at condition 2d.

63

The electron densities are plotted on a logarithmic scale. The floating potential and electron temperature measurements are used to calculate the plasma potential. The electron temperatures were about 2 to 5 eV inside the discharge chamber. The highest electron density was observed just downstream of the cathode. Once again, the triple probe data may have been affected by errors from electrode shadowing and sheath interactions at the low plasma densities in regions outside of the discharge chamber.
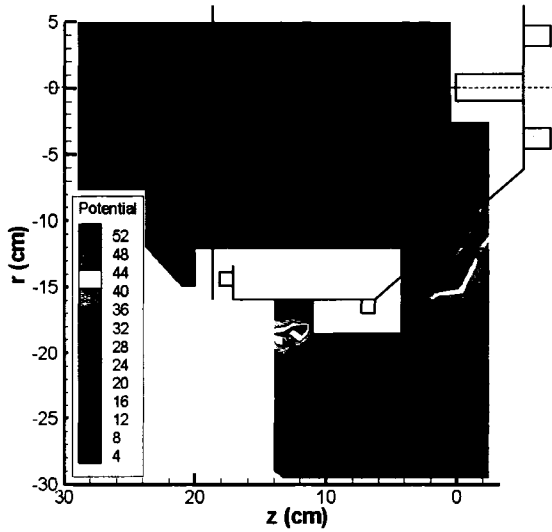

Figure 3.18a Condition 2d. Triple probe potential measurements at J_D = 13.0 A, $\dot{m}$ = 13.1 sccm Xe, V_D = 25.2 V.
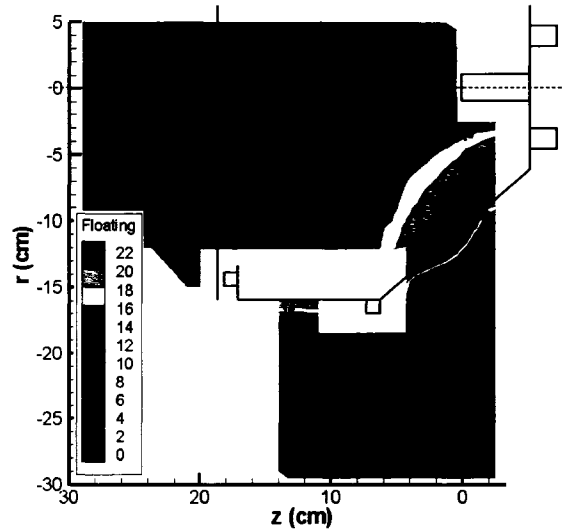
Figure 3.18b Triple probe floating potential (V_f) measurements at condition 2d.
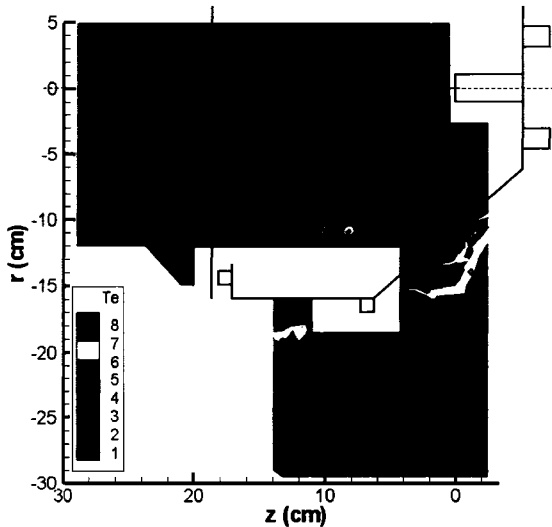
Figure 3.18c Triple probe electron temperature, T_e (eV), measurements at condition 2d.
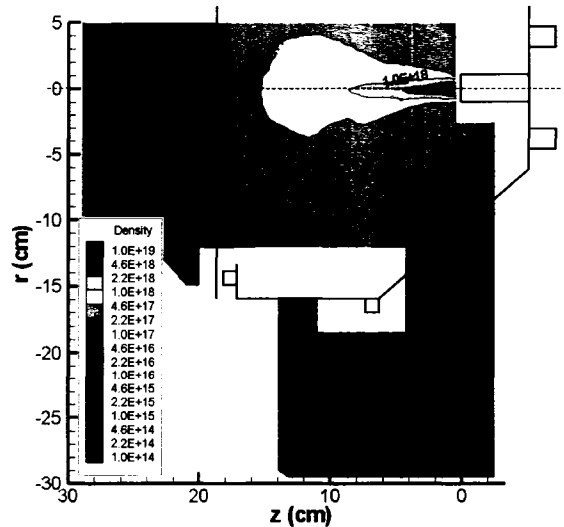
Figure 3.18d Triple probe electron density, n_e (#/m^3), measurements ($\cong$ ion density, n_i) at condition 2d.

64

3.2.3 Emissive Probe Potential Oscillations

Temporal measurements of plasma potential are shown in Figure 3.19 at condition 2d. The maximum amplitude oscillations occurred near the cathode and were ±2.5 V relative to the time-averaged values. In general, the oscillation amplitudes for the prototype NSTAR configuration of case 2 were much lower than for the open cathode configuration of case 1. However, as with all of the conditions in case 1, the oscillation amplitude in case 2 also increased at locations close to the hollow cathode.
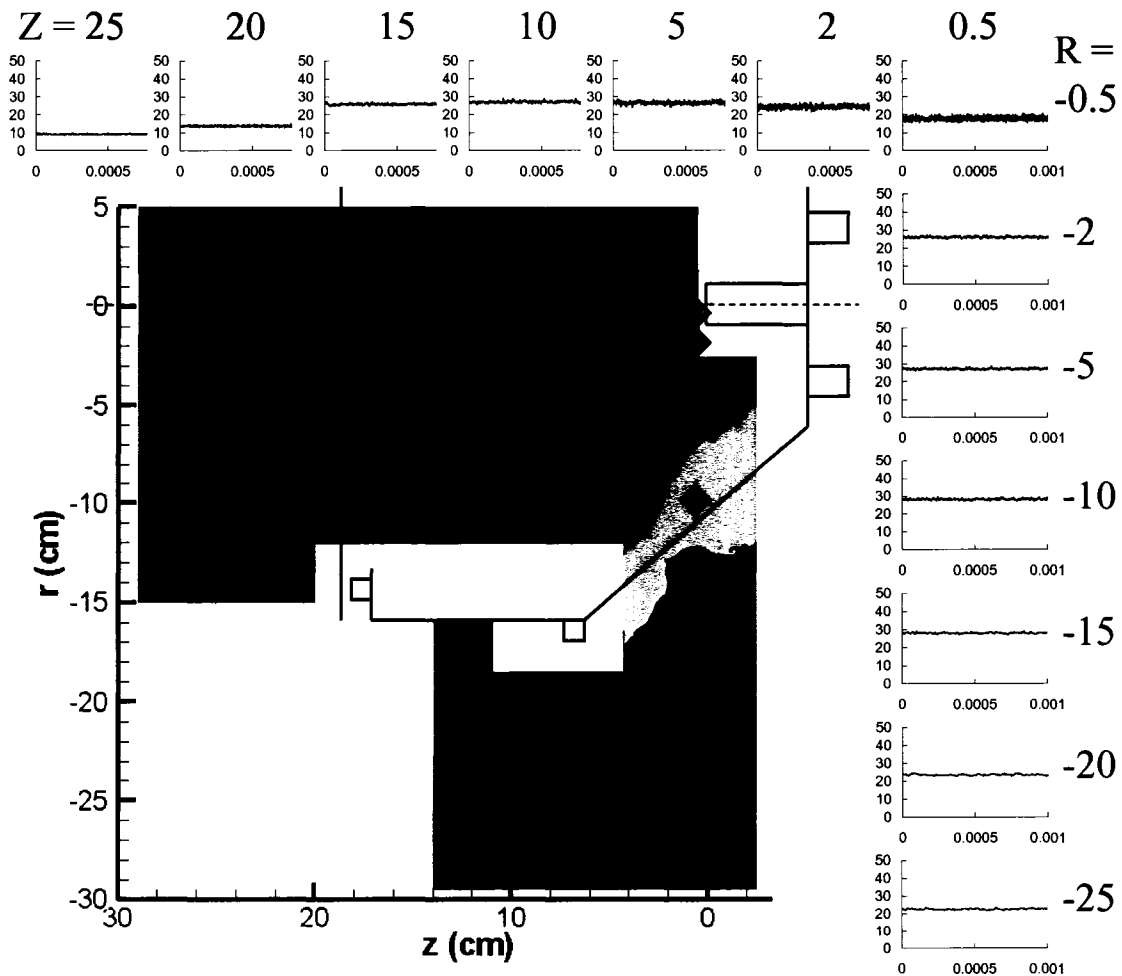
Figure 3.19   Potential versus time at selected locations using the emissive probe at condition 2d (J_D = 13.0 A, $\dot{m}$ = 13.1 sccm Xe, V_D = 25.2 V). The y-axis is plasma potential (0 to 50 V) and the x-axis is time (s).

65

Figure 3.20 contains a comparison of plasma potential waveforms at selected operating conditions at a constant radial location of -0.5 cm. The oscillation amplitudes were similar for conditions 2a through 2e. This is somewhat interesting considering the discharge current was varied from 4.5 to 18.0 A, however, it is noted that the discharge voltage was held nearly constant at 25 V by varying the flow rate through the cathode. Operation at constant discharge voltage will likely result in similar coupling in the plasma region between the cathode and anode. The oscillation amplitudes were higher at condition 2f where the discharge voltage was higher at 36.0 V and the ratio of the discharge current to the flow rate was higher.
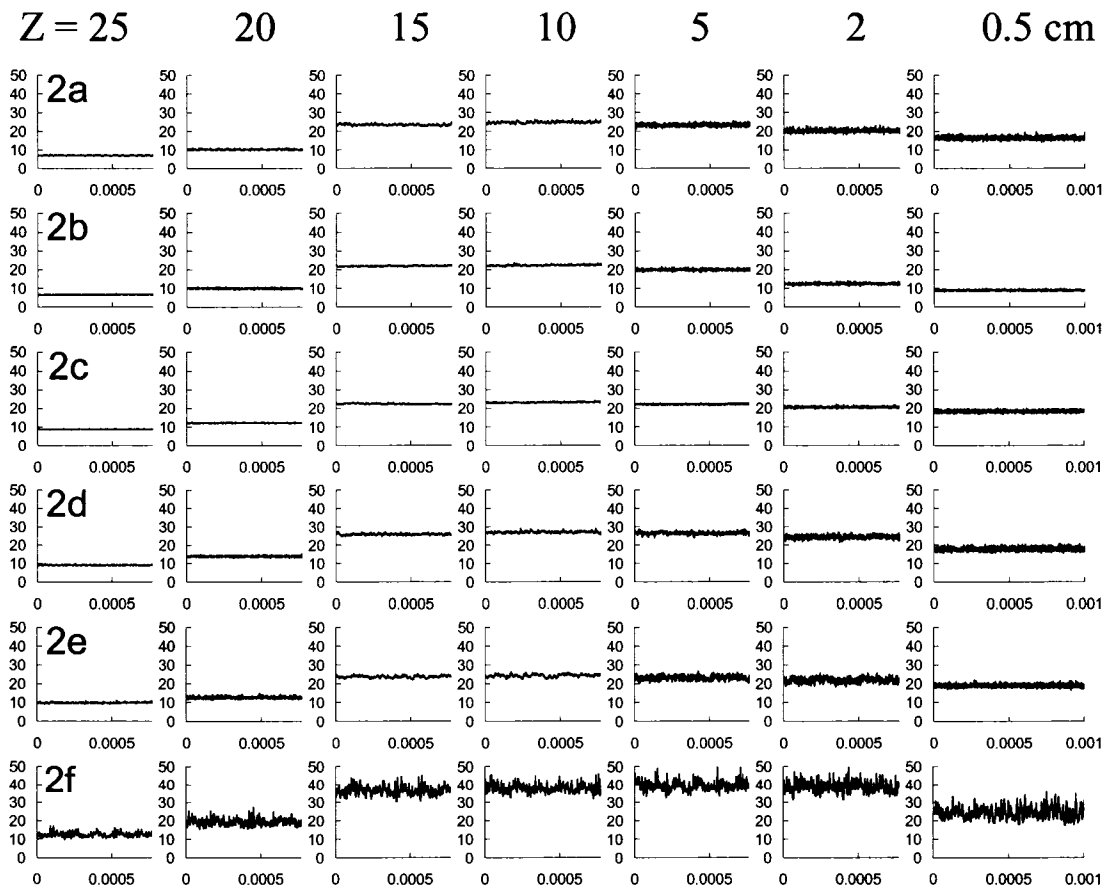
Figure 3.20 Emissive probe oscillations at selected axial locations from z = 0.5 to 25 cm from the cathode/keeper at a radial location of r = -0.5 cm (see diamonds on Figure 3.19 for relative locations with respect to the cathode). The y-axis is plasma potential (0 to 50 V) and the x-axis is time (s).

66

Additional plots of the higher amplitude oscillations are shown in Figure 3.21.

The oscillations near the cathode varied over a range of ±5 V relative to the time-averaged potentials.
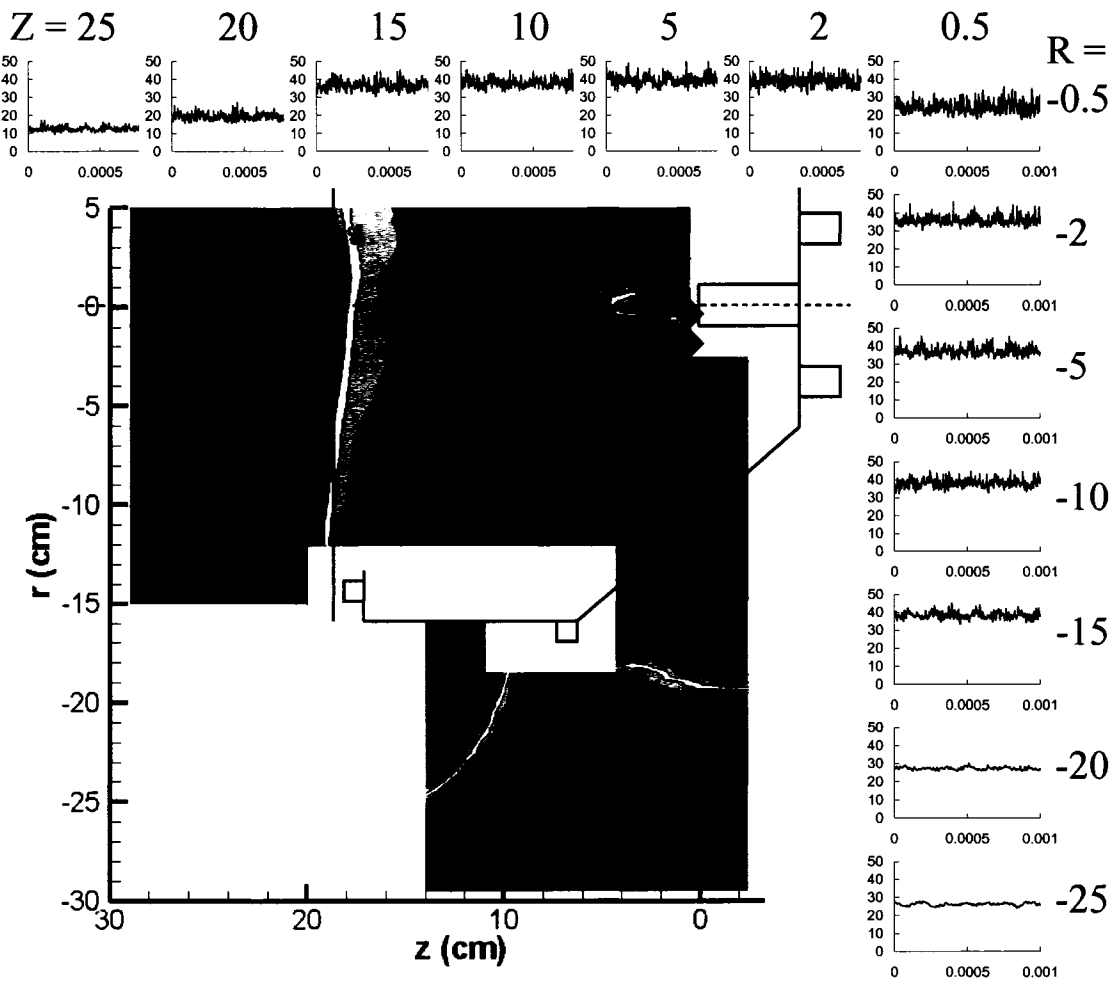
Figure 3.21   Potential versus time at selected locations using the emissive probe at condition 2f (J_D = 18.0 A, $\dot{m}$ = 8.3 sccm Xe, V_D = 36.0 V).   The y-axis is plasma potential (0 to 50 V) and the x-axis is time (s).

The emissive probe was also used to measure the potential versus time for different cathode flow rate values. While operating conditions 2a through 2e showed the effects of changing the discharge current while adjusting the flow rate to maintain a

67

discharge voltage near 25 V, this test was performed by varying the flow rate while keeping the discharge current constant. Figure 3.22 shows a plot of the measured potentials along with frequency plots at four cathode flow rates of 2.3, 2.7, 3.1, and 3.5 sccm Xe. In this test, a second flow line was installed in the prototype NSTAR discharge chamber that allowed for main discharge flow in addition to the xenon flow through the cathode. The discharge current and the main flow rate were maintained at 8.3 A and 15 sccm Xe, respectively.
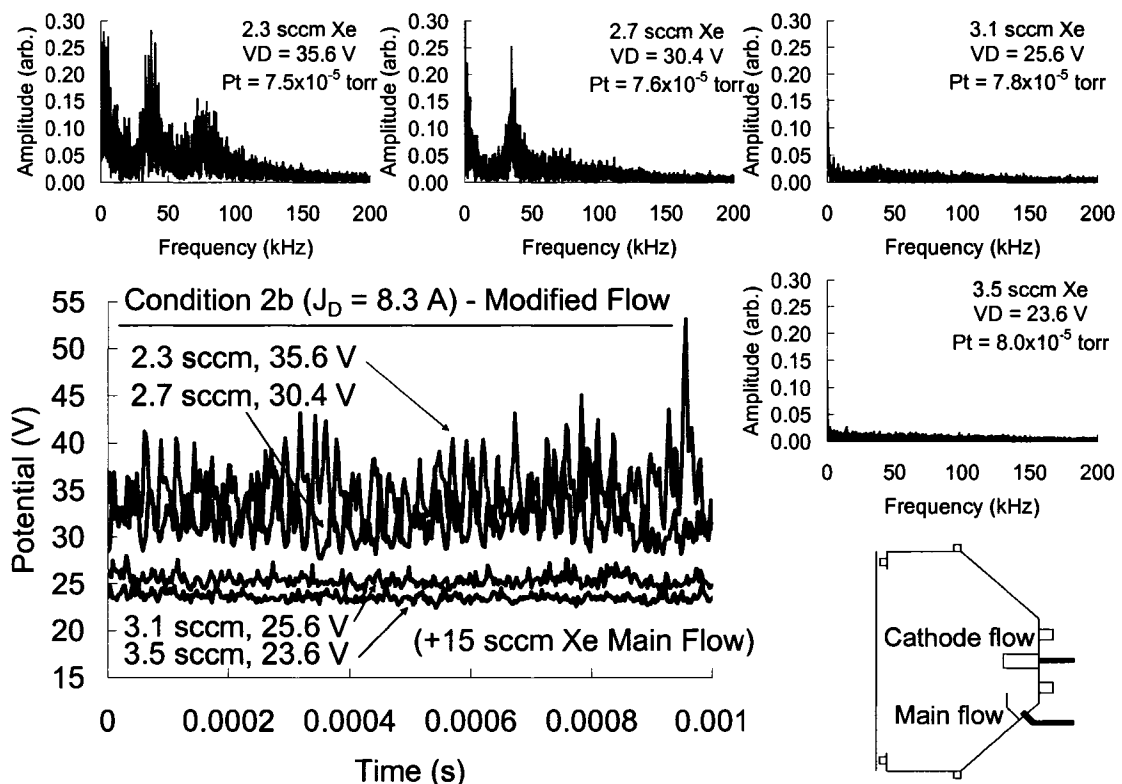
Figure 3.22 Emissive probe potential versus time and frequencies for four cathode flow rates of 2.3, 2.7, 3.1, and 3.5 sccm Xe. In this experiment, the discharge current was held constant at 8.3 A and xenon was injected through a main flow line at 15 sccm in addition to the specified cathode flow. The emissive probe was located at r = 3 cm, z = 3 cm.

The potential versus time plots in Figure 3.22 show the oscillation amplitude decreasing as the cathode flow rate was increased. Large plasma potential oscillations of

68

15 V peak-to-peak were observed at the lowest cathode flow rate of 2.3 sccm Xe. The frequency spectrums of the potential waveforms are also shown for each of the four flow rates in Figure 3.22. At low flow rates, peaks in the frequency spectrum were detected at 38 and 76 kHz. There was also a peak at lower frequencies in the 2 to 4 kHz range. Figure 3.22 suggests that the flow rate through the cathode has a large effect on both the discharge voltage and the oscillation characteristics of the discharge chamber plasma.

3.2.4 Multiple Emissive Probe Measurements

Two emissive probes were installed in the prototype NSTAR discharge chamber setup to study the correlation of the potential oscillations observed near the cathode. A high level of correlation between the two probes suggests that plasma potentials rise and fall together while low levels of correlation suggest a more randomized time dependence in the oscillations. Figure 3.23 contains plasma potential measurements from two emissive probes separated by ~ 2 to 3 cm for condition 2d. Three orientations were used; one in which the emissive probes were separated radially with respect to each other and another two in which the emissive probes were separated axially with respect to each other. In each of the three orientations (Figure 3.23b-d), the plasma potential oscillation pattern was nearly the same for the two probes. This is interesting considering that there was no definite single frequency signal observed in the measurements. The pattern was most similar for lower frequencies in the 5 to 100 kHz range while the pattern became slightly less similar for higher frequencies above 100 kHz. Recall that the oscillation amplitudes for the case 2 configuration were low in general and that variations in the measurements were affected to some degree by noise from the probe circuits and data acquisition system, especially at higher frequencies above a hundred kHz where the

69

oscillation amplitude approached the noise floor. Similar trends were observed at all other operating conditions.

One way to characterize the correlation between two signals is to calculate the correlation coefficient over the sampled time period. The correlation coefficient, r, can be defined as:

$$Correl(X,Y) = r = \frac{\sum_i (x(i) - \bar{x}) \cdot (y(i-d) - \bar{y})}{\sqrt{\sum_i (x(i) - \bar{x})^2 \cdot \sum_i (y(i-d) - \bar{y})^2}}$$
Eq. 3.1

Where $\bar{x}$ and $\bar{y}$ are the sample means of the signals x(t) and y(t), and d is a sample delay between the signals. The correlation can be calculated using different delay values to determine if the signals are correlated but shifted in phase. The correlation function can result in values from -1 to 1, where values close to 1 or -1 mean that the signals are well correlated. A correlation function value of 1 means that the signals are exactly the same in frequency and phase (but can have different amplitudes) whereas a value of -1 means that the signals have the same frequency but are exactly out of phase. Correlation function values near zero (determined over range of chosen delay values) suggest that the signals are not related. (Note that the best fit correlation values (r_{max}) are listed on each of the plots along with the delay used to determine the maximum correlation.) For the conditions in Figure 3.23, the correlation coefficients were near 1 (r_{max} = 0.78 to 0.82 for a delay time of 1.0 µs) which indicated that the signals were similar in both frequency and phase.

70
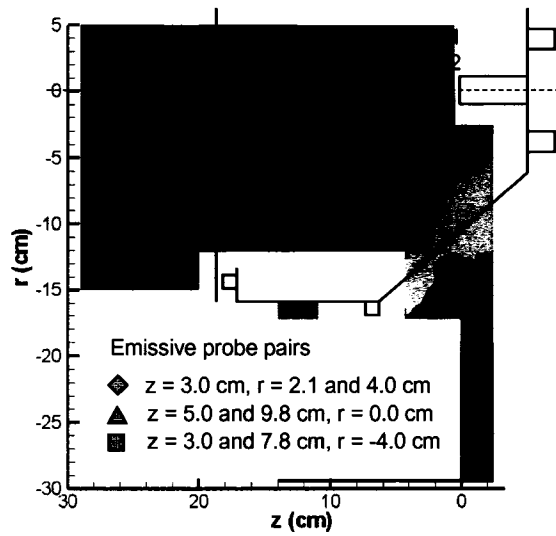
Figure 3.23a   Time-averaged emissive potential contour plot at condition 2d (J_D = 13.0 A, $\dot{m}$ = 13.1 sccm Xe, V_D = 25.2 V).
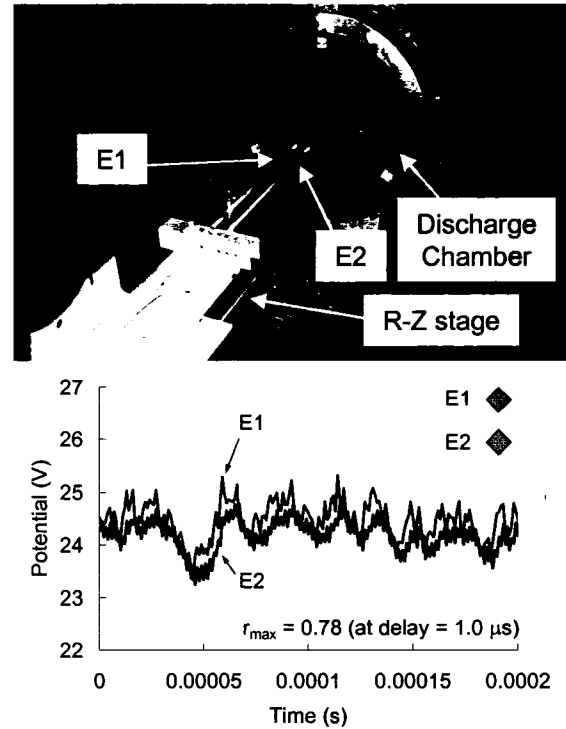
Figure 3.23b   Potential versus time using two emissive probes at different locations. The potentials rise and fall together in the lower frequency ranges.
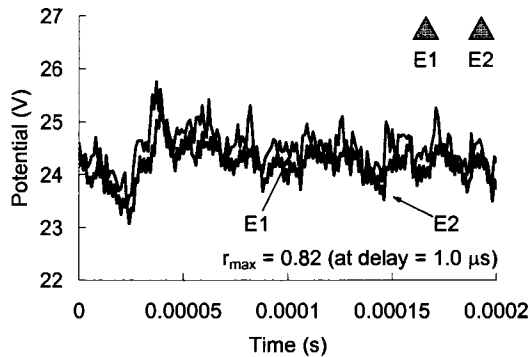
Figure 3.23c   Potential versus time using two emissive probes at different locations.
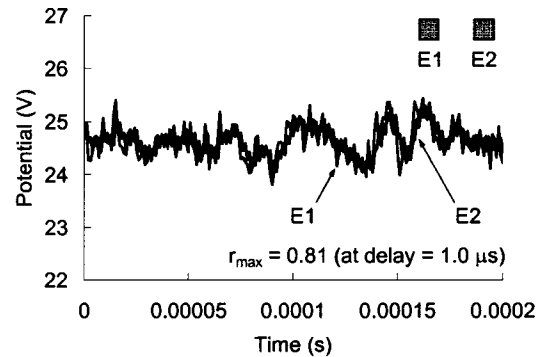
Figure 3.23d   Potential versus time using two emissive probes at different locations.

The frequency of the oscillations ranged from about 5 to 60 kHz with no definite single frequency component in the signal. One interesting feature was observed when the discharge was operated in the constant voltage mode instead of the conventional constant current mode. This was done to investigate the effects of the discharge power supply on

71

the plasma oscillations. The potential versus time and the frequency spectrum of the signal are shown in Figure 3.24c-d. The potential oscillations displayed larger magnitude and a more dominant single frequency component near 85 kHz compared to the conventional constant discharge current condition (see Figure 3.24a-b). Although differences were noted at 85 kHz, it is pointed out that there were oscillation features in the 5 to 50 kHz range that were similar for both discharge operating modes. It is believed that the 85 kHz signal was excited by coupling between the discharge plasma circuit and the discharge power supply that is quenched when the power supply is operated in constant current mode.
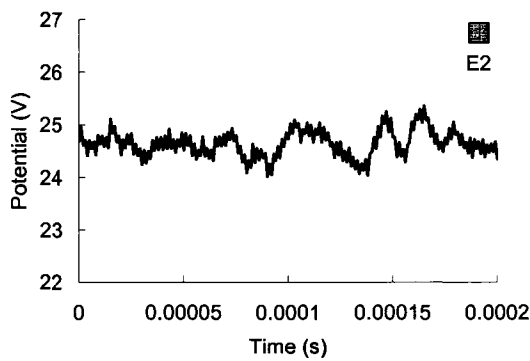
Figure 3.24a Potential versus time at r = -4.0 cm and z = 3.0 cm at condition 2d (J_D = 13.0 A, $\dot{m}$ = 13.1 sccm Xe, V_D = 25.2V).
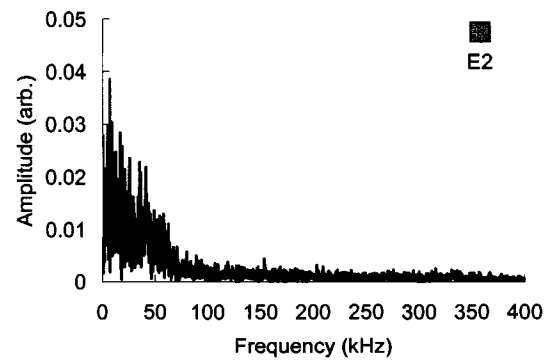
Figure 3.24b Frequency spectrum of the plasma potential at r = -4.0 cm and z = 3.0 cm.
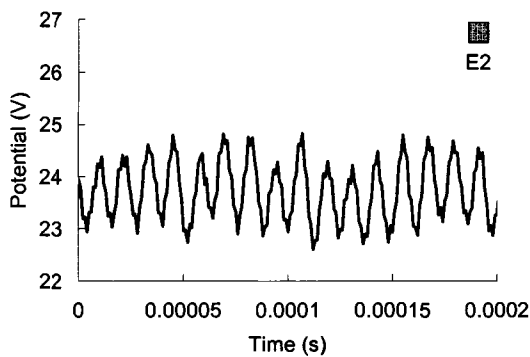
Figure 3.24c Potential versus time using an emissive probe with the discharge operated in the constant voltage mode instead of the conventional constant current mode.
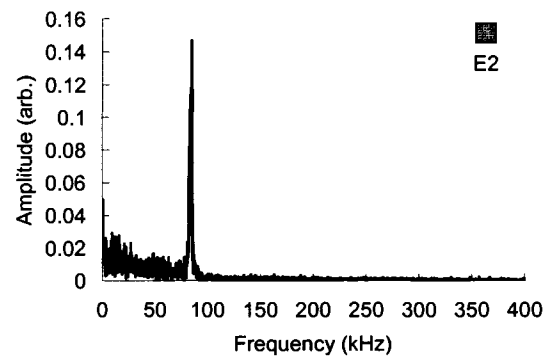
Figure 3.24d Frequency spectrum of the potential at r = -4.0 cm and z = 3.0 cm. Note the frequency component in the signal near 85 kHz in addition to oscillations in the 5 to 50 kHz range.

72

Examples of coupling between the discharge plasma and the anode and keeper power supplies can be seen in Figure 3.25 for both the constant current mode and the constant voltage mode at condition 2d. The potential versus time was measured on both the anode and keeper power supply leads and simultaneously on an emissive probe placed within the discharge plasma.
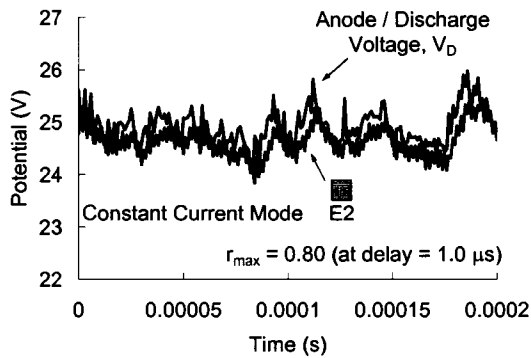
Figure 3.25a Potential versus time from an emissive probe placed in the plasma versus the discharge voltage (conventional constant current mode) at condition 2d.
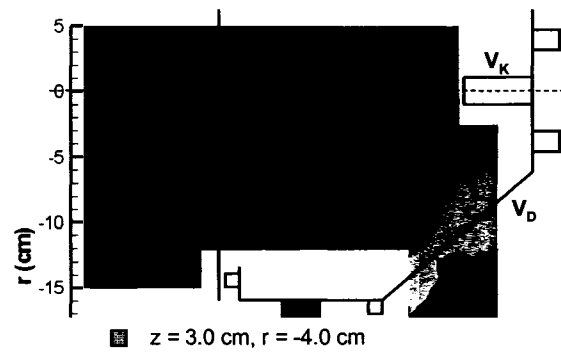
Figure 3.25b Condition 2d (J_D = 13.0 A, $\dot{m}$ = 13.1 sccm Xe, V_D = 25.2 V). The emissive probe was located at r = -4.0 cm and z = 3.0 cm from the cathode.
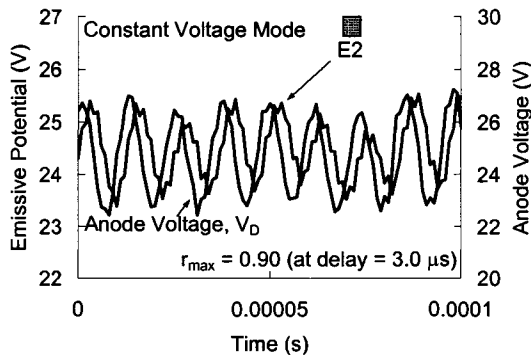
Figure 3.25c Potential versus time from an emissive probe placed in the plasma versus the discharge voltage (constant voltage mode) at condition 2d.
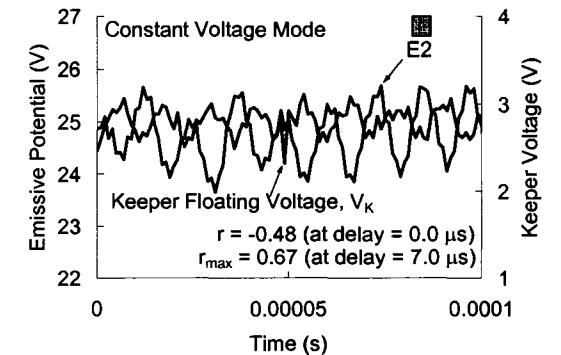
Figure 3.25d Potential versus time from an emissive probe placed in the plasma versus the keeper floating voltage (constant voltage mode) at condition 2d.

The correlation coefficients were near 1 (r_{max} = 0.67 to 0.90) which means that the signals were well correlated. However, there was a larger delay, or phase, between the

73

emissive-to-power supply comparisons compared to the correlations between the signals from the two emissive probes. The signals from the emissive probe and anode were more out of phase in the constant voltage mode than in the constant current mode. The keeper floating voltage was also well correlated with the emissive probe potential (r_{max} = 0.67 for a delay of 7.0 μs), but the signals were nearly out of phase (r = -0.48 for a delay of 0.0 μs) at this location and operating condition.

3.2.5 Possible Causes of the Potential Profiles and Oscillations

From the emissive probe measurements, plasma potential oscillations were observed in case 1 and case 2 discharge chamber configurations. In the open cathode configuration of case 1, the oscillations had amplitudes with plasma potentials near (and possibly exceeding) the probe circuitry limit of 85 V with respect to the cathode. These are large amplitudes considering the cathode-to-anode voltage differences were only 25 to 35 V. In the prototype NSTAR configuration of case 2, lower amplitude oscillations were recorded near the cathode having potentials of ±2 to ±5 V with respect to the time-averaged plasma potential readings. In both cases, the oscillation amplitudes were highest at locations within a few centimeters of the hollow cathode/keeper region. The frequency spectrums in both cases had significant frequency content from about 5 to 100 kHz depending on the operating condition and probe location relative to the hollow cathode. In the open cathode configuration of case 1, there was a slightly more defined frequency component in the 40 to 50 kHz range. Similar plasma potential measurements have been made by Goebel et al.[30] nearby hollow cathodes and by Fitzgerald[54]. Although the discharge chamber conditions and cathode and keeper assembly dimensions of these

74

studies were different from the measurements presented herein, both observed potential oscillations that had similar frequency content in the 50 to 100 kHz range.

The physical bases of the potential profiles and oscillations are difficult to determine. In the experimental sense, it appears that some mechanism exists whereby potential hills and oscillations develop either as a result of the conduction of electrons to the anode or to facilitate the conduction process. One supporting piece of evidence for this explanation is the strong oscillations that occur when the flow rate to discharge current ratio falls below a critical value for a given discharge geometry. Most discussions of potential oscillations in the frequency ranges seen in these experiments have focused on turbulent ion acoustic waves[16,33,52,53,54,55].

Choueire[33] describes both ion and electron interactions with neutrals as well as ionization instabilities that can create fluctuations in a plasma. The ion-neutral instability (or ion acoustic instability) can arise whenever there are density gradients in a weakly ionized plasma. The ionization instability is described as arising from excess electron energy (e.g., the presence of primary electron populations) in a localized part of the plasma. These energetic electron populations can lead to localized enhancement of plasma density and subsequent modification of primary electron energy (due to changes in localized plasma conductivity) and ionization rate. The changes in ionization rate can disrupt in the current flow through the local region and lead to oscillations of local plasma properties. Both ion acoustic and ionization instabilities are likely to exist near the cathode where large density gradients are present and where relatively large numbers of energetic (primary) electrons are present while relatively large electron currents are being drawn from the cathode toward the anode.

75

The ion wave, or ion acoustic instability, can develop when counter streaming electrons and ions are present in a plasma[52,53] when the drift velocity between the electrons and ion reaches a certain critical velocity. The critical velocity, which depends highly on the ratio of electron temperature to ion temperature, can be more easily reached when the ratio of T_e/T_i is high[16,55] as it is in the discharge plasmas being considered herein ($T_e/T_i \sim 10 - 100$). Such a two-stream condition can exist near a hollow cathode where electrons stream from the cathode orifice and ions stream toward the cathode. Judging by the magnitude of T_e/T_i alone, the instability might be expected to be larger at locations away from the cathode where the electron temperature is higher. However, the electric fields and density gradients are largest near the cathode, which also contribute to the instability onset and growth rate.

3.2.6 Electrostatic Analyzer and ExB (ESA_ExB) Remote Measurements

The combined ESA_ExB probe was used to investigate the discharge plasma produced in the prototype NSTAR configuration (case 2). Figure 3.26 shows the measured ion energy distribution function (IEDF) for each operating condition at zenith angles of 0 and 90 degrees. The entrance to the ESA was located about 55 cm away from the keeper plate for all of the zenith angles shown. The most probable energy of the ions occurred at or just below the value of the discharge voltage. The magnitude of the ion current to the ESA was about 5 to 10 times less at 90 degrees compared to 0 degrees. At most operating conditions and zenith angles, there were a small number of ions that had energies above the cathode-to-anode voltage difference. The largest fractions of energetic ions were usually observed at off-axis zenith angles, usually at the 30 degree angle.

76
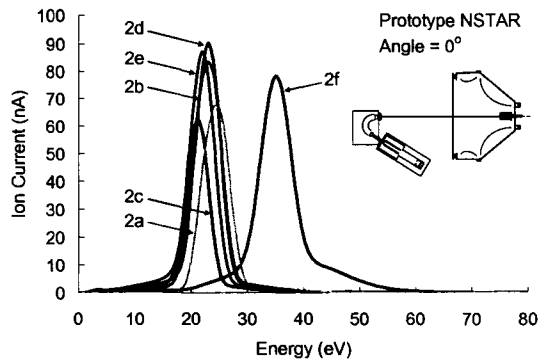
Figure 3.26a IEDFs measured at a zenith angle of 0 degrees using the ESA. The most probable energy of the ions occurred near the discharge voltage (Conditions 2a-2e ≅ 21-24 eV, condition 2f ≅ 35 eV).
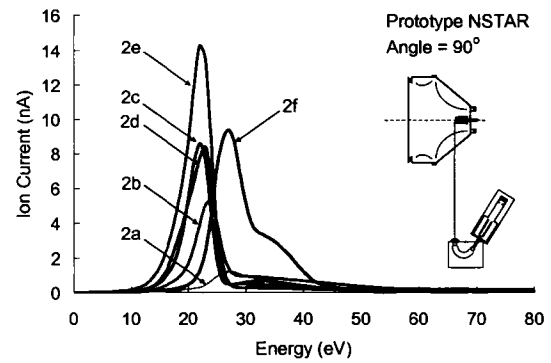
Figure 3.26b IEDFs measured at a zenith angle of 90 degrees using the ESA. Note that the ion current to the ESA (y-axis) was much lower than for the IEDFs recorded at 0 degrees.

A comparison of the IEDFs at different zenith angles is shown in Figure 3.27 for conditions 2b and 2f. The current magnitude was highest at the 0 degree zenith angle. The lowest ion currents occurred at 55 degrees, where the ESA was positioned to look at the cathode through the cylindrical portion of the anode. The plots are also shown on an expanded y-axis scale in Figure 3.27c and Figure 3.27d to show more detail of ions measured at higher energies. It is somewhat unclear as to the creation point of the high energy ions considering the emissive probe measurements did not show plasma potentials or potential oscillations to values much higher than the discharge voltage in the regions that were mapped.

Figure 3.27 also shows the doubles-to-singles ratio when the ESA_ExB was positioned along the cathode centerline at 0 degrees. At operating conditions 2b and 2f, the doubles-to-singles ratio was low for ion energies (actually E/z) near the discharge voltage (0.5 to 10 %), however, the ratio increased for ions with energies above the discharge voltage (5 to 45 %) and below the discharge voltage. In fact, the doubles-to-singles ratio was much higher for ions with energies below the discharge voltage,

77

especially at a zenith angle of 0 degrees. For example, there were up to twice as many

doubles as singles (comparing ion currents) in the 25 eV range at condition 2f. These

lower energy ions most likely originate from regions near the pseudo-screen grid where

the plasma potential begins to drop below the potentials found in the center of the

discharge region. The ions could also be created near the cathode where the potentials

are lower but they would not likely overcome the negative potential gradients in order to

exit the discharge chamber.
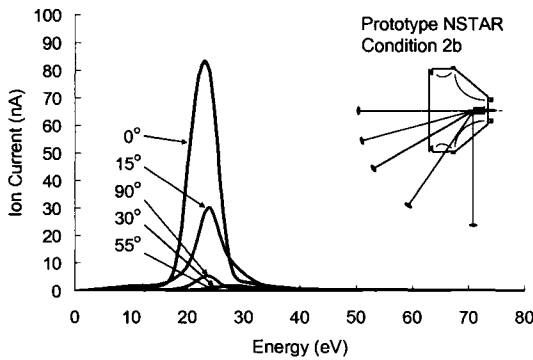
Figure 3.27a   IEDFs measured at zenith angles of 0, 15, 30, 55, and 90 degrees for condition 2b (J_D = 8.3 A, $\dot{m}$ = 6.1 sccm Xe, V_D = 24.9 V).
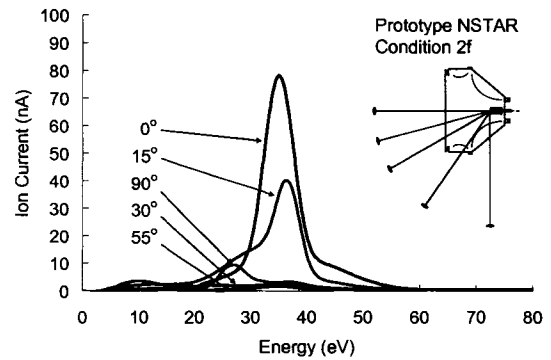
Figure 3.27b   IEDFs measured at zenith angles of 0, 15, 30, 55, and 90 degrees for condition 2f (J_D = 18.0 A, $\dot{m}$ = 8.3 sccm Xe, V_D = 36.0 V).
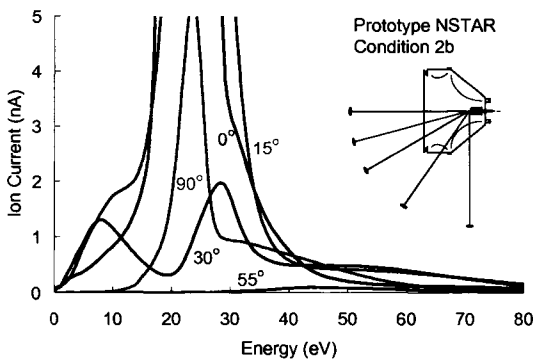
Figure 3.27c   IEDFs for condition 2b. Expanded y-axis is shown to see the small numbers of ions with energies above the cathode-to-anode voltage difference.
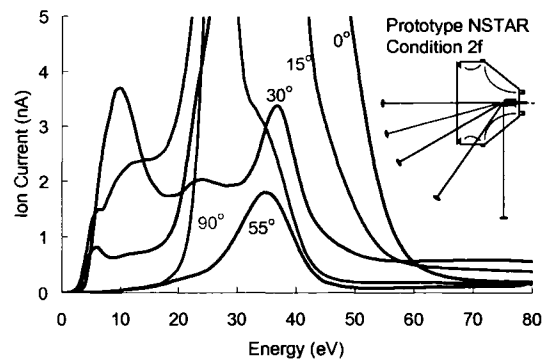
Figure 3.27d   IEDFs for condition 2f. Expanded y-axis is shown to see the small numbers of ions with energies above the cathode-to-anode voltage difference.
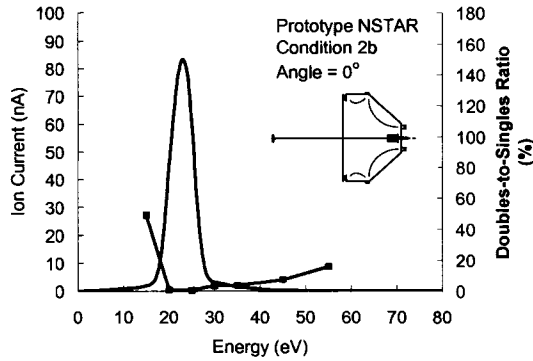
Figure 3.27e ESA_ExB probe measurements at a zenith angle of 0 degrees for condition 2b.
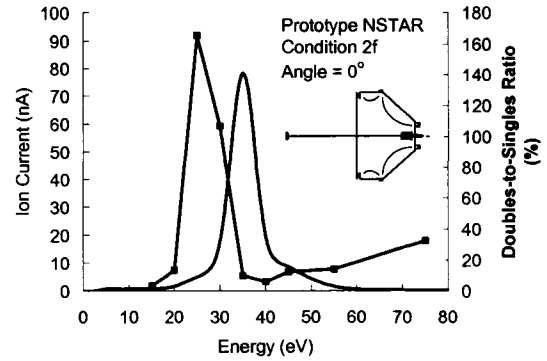
Figure 3.27f ESA_ExB probe measurements at a zenith angle of 0 degrees for condition 2f.
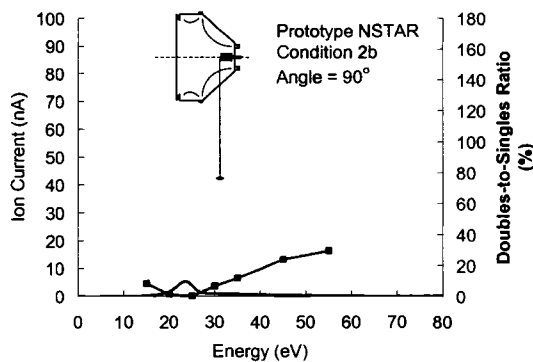
Figure 3.27g ESA_ExB probe measurements at a zenith angle of 90 degrees for condition 2b.
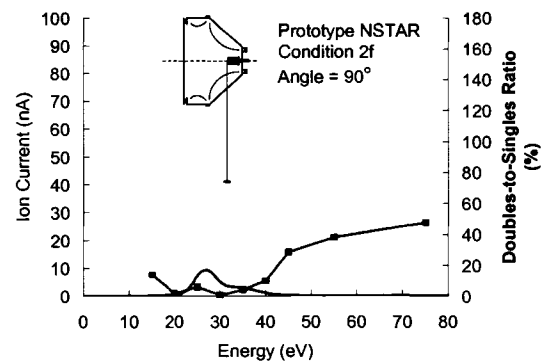
Figure 3.27h ESA_ExB probe measurements at a zenith angle of 90 degrees for condition 2f.

Figure 3.28 shows IEDF measurements along with doubles-to-singles ratios as a function of radial position relative to the cathode axis. (Specifically, the ESA_ExB probe was placed at locations of 0, -5, and -10 cm relative to the cathode axis.) The discharge current was 10 A and the discharge voltage was 27 V. The ion current to the ESA decreased as the ESA was moved radially outward from the centerline. The doubles-to-singles ratio was low for ion energies (E/z) near the discharge voltage (0.6 to 5.0 %) and the ratio increased (5 to 20 %) at higher ion energies. The largest variation between positions, however, was observed for ions with energies just below the discharge voltage. The ratio was highest when the ESA was positioned on the cathode centerline. As with

79

the other operating conditions investigated with the prototype NSTAR discharge chamber, the lower energy ions observed with the ESA most likely originate from regions near the pseudo-screen grid where the plasma potential begins to drop below the potentials found in the center of the discharge region.
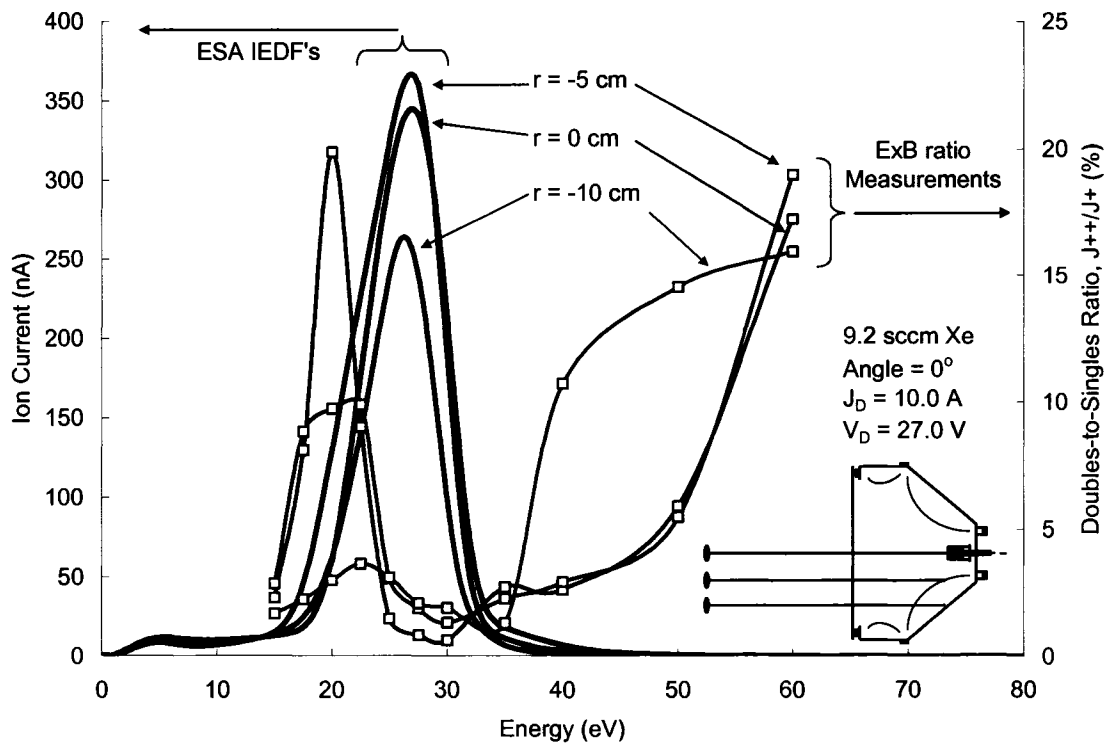
Figure 3.28 ESA_ExB probe doubles-to-singles ratio as a function of position relative to the cathode centerline.

4 Correlation Model for Direct and Remote Probes

4.1 Model Setup and Explanation

The results section above presented measurements from four different sources: a floating emissive probe, a triple Langmuir probe, an electrostatic analyzer (ESA), and an ExB probe (Vein filter). The direct measurement emissive and triple Langmuir probes yielded spatial information such as the plasma potential, electron temperature, and electron density within the plasma while the remotely located ESA_ExB probe yielded information about the energy and charge state of the ions flowing from the plasma region.

It would be useful to correlate and compare measurements from the different probes, both to verify what each probe is measuring and to investigate effects occurring in the plasma. For example, it would be useful to measure plasma potential throughout the discharge chamber and determine the resulting IEDF at a given zenith angle and distance. Alternately, it would be useful to use a set of measured IEDFs along with the discharge chamber geometry to re-create the structure of the discharge plasma. To compare the measurements from the probes, a model was created to incorporate the direct and remote properties. Specifically, the model described below takes the directly measured plasma properties as inputs and generates a resulting IEDF. The resulting IEDF from the model calculations was then compared to the IEDF measured with the remotely located ESA.

81

4.1.1 Model Input

The following items were used as inputs to the model.

1. Plasma potential profile.

    a. A set of plasma potentials over a two dimensional (r,z) space are input from the emissive and triple probes. In most cases, the time-averaged emissive probe potentials are used over the values obtained with the triple probe potentials because the former are considered more accurate over the entire mapped region.

    b. The plasma potential values are used to estimate the electric field, E (V/m), at each (r,z) location. The electric fields are necessary to calculate basic ion trajectories through the simulation region. Those initial potentials and electric fields could be later modified to alter the resulting ion distribution.

2. Ion and neutral density profiles.

    a. An estimate for the ion density comes from the triple Langmuir probe estimate of the electron density. Within the plasma, the ion density is equal to the electron density ($n_i \cong n_e$) at each location.

    b. The ion (and electron) density is used to estimate at the ion generation rate at each (r,z) location. This rate is important to re-create the IEDF which is a measure of the number of ions having a certain energy based on the potential at which each ion was created.

82

c. A neutral density profile can be used to determine charge exchange reaction rates that could alter the resulting IEDF, but for this simplified model, no charge exchange reactions were considered.

3. Time-varying potential and density information.

   a. Data from the time-varying emissive probe potential measurements are used in the model.

   b. This input is necessary to account for the large amplitude time-varying oscillations that were observed, especially in the open cathode configuration of case 1 where no magnetic field was present. The potential oscillations are expected to have an effect on the energy of ions observed in the distribution. For example, it is reasonable to imagine that the energetic ions detected in the 50 to 150 eV range in case 1 originated from ions produced when the local plasma potential was at the higher points of the oscillation cycle.

   c. The ion production rate would also likely change as a result of potential oscillations. For example, a varying ion production rate could be incorporated by estimating the production rate as a function of the electron-xenon ionization cross section.

4.1.2 Model Flow Process

The model flow processes included the following steps.

1. Input steady state profile geometry and create a 2d (r,z) mesh.

2. Input time-varying potential information. In each case, an equation is used to describe how the potentials vary with time (one oscillation cycle) along with a

83

second equation to describe how the potential (both dc and ac components) varies with position.

3. Input ion density formulas. An equation is used to describe how the ion density varies with position.

4. Calculate ion trajectories through the simulation region over a period of one oscillation. The ion weighting (density) and energy is varied over the entire mesh according to the measured plasma properties at each starting location.

5. For each ion tracked, record the initial location, trajectory, exit location, energy, and weight value to determine the resulting IEDF.

6. In the instance where the user is working toward a pre-defined IEDF (which was not done in the present work), the next step would be to modify the steady or time-varying potentials and ion production rates and iterate on the result.

4.2 Geometry Model

The simulation region consisted of a two dimensional array with limits corresponding to the measured emissive probe regions in each case. Figure 4.1 shows the mesh used for both cases. In case 2, two regions were considered; one mesh was used when looking for ions that exited through the pseudo-screen grid (0 to 30 degrees with respect to the cathode) and another mesh was used when looking for ions that exited through the anode (90 degrees with respect to the cathode).

84
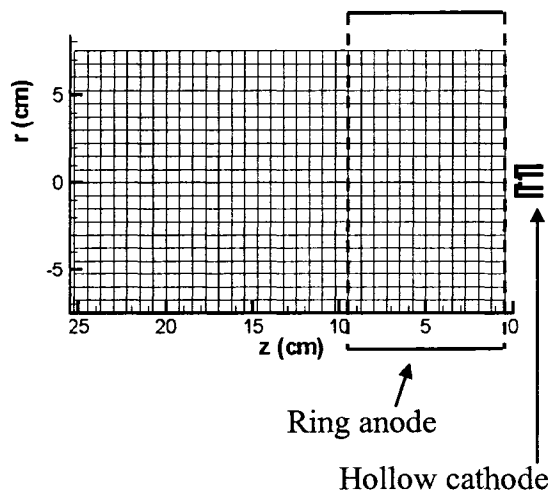
Figure 4.1a Simulation region for the open cathode configuration, case 1. The cathode and anode are shown for reference.
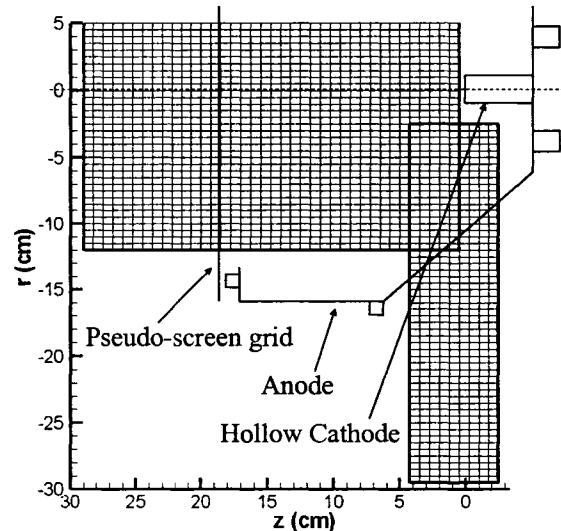
Figure 4.1b Simulation regions for the open cathode configuration, case 2. The cathode, anode, and pseudo-screen grid are shown for reference.

4.3 Ion Density Model

The ion density was modeled by fitting a power equation to the electron density data from the triple Langmuir probe. Due to the quasi-neutrality of the plasma, the ion density is equal to the electron density ($n_i \cong n_e$) at each location. The peak of the ion density was centered near the hollow cathode orifice and dropped as the distance was increased away from the cathode. The power fit equation was:

$$w_{avg}(x) = w_0(x)^{w_1} \qquad\qquad \text{Eq. 4.1}$$

Where $w_{avg}(x)$ was the weight, or density, of the ions, x was the distance from the peak ion density location (near the cathode/keeper orifice), and w_0 and w_1 were constants to describe how the ion density varied with distance. The ion density was limited to a maximum value close to the cathode when the distance, x, was small.

85

The temporal ion density for a particular location was then modified from its steady state value according to the electron-ion ionization cross section, which is a function of the potential, ϕ(r,z,t). This was done to account for higher ionization rates that will occur when the plasma potentials were high due to the increased electron-ion ionization cross section. The equation used was:

$$w_{particle}(r,z,\phi) = w_{avg}(r,z) \cdot \sigma(\phi)$$ Eq. 4.2

Where $w_{particle}$ was the weight of a test particle, w_{avg} was the weight according to position, and σ was the electron-ion cross section determined by the potential at the initial particle location. Also note that the potential, ϕ, was a function of position and time. This modification to the weight of the particle results in a slight preference to particles being born at higher potentials.

4.4 Plasma Potential Model (Time-Varying + Position)

The plasma potential was observed to vary as a function of time and position. In general, the potential at a given position was calculated as the average potential at that location plus an oscillation potential:

$$\phi(r,z,t) = \phi_{avg}(r,z) + \phi_{osc}(r,z,t)$$ Eq. 4.3

The average potential at a particle location, ϕ_{avg}(r,z), was found directly from the time-averaged emissive probe measurements at the chosen operating condition. Two equations were used to describe the potential oscillations; one equation described how the potential varied with time (over one oscillation cycle) and a second equation described how the potential magnitude varied with position:

$$\phi_{osc}(r,z,t) = \phi_{osc\_p}(r,z) \cdot \phi_{osc\_t}(t)$$ Eq. 4.4

86

To describe how the plasma potential varied with time, Eq. 4.5 was used:

$$\phi_{osc\_t}(t) = \begin{vmatrix} \dfrac{1}{2-b}\cdot\left(1 - b - \cos\left(\dfrac{t}{b}\cdot 2\cdot\pi\right)\right) & \text{if } t < b \\[2ex] \dfrac{-b}{2-b} + \dfrac{1}{M}\cdot\sin\left[2\cdot\pi\cdot\left(\dfrac{t-b}{1-b}\right)\right] & \text{otherwise} \end{vmatrix}$$

Eq. 4.5

Where ϕ_{osc_t} was the potential at time, t. For the simulation, the time was varied from 0 to 1 to simulate one oscillation cycle and the particle trajectories were calculated at each chosen time. The variables b and M were constants and were chosen to approximate how the potential varied with time by looking at the emissive probe time-varying data. The potential oscillation profile was chosen such that the integral from time 0 to 1 was equal to zero. This means that on average the potential at each location was equal to the measured potential from the emissive probe.

A second equation (Eq. 4.6) was used to describe how the magnitude of the potential oscillations varied with position:

$$\phi_{osc\_p}(d) = A\cdot\frac{C_1\cdot e^{-C_2\cdot\frac{d}{d_0}} + C_3}{C_1 + C_3}$$

Eq. 4.6

Where ϕ_{osc_p} was the potential as a function of position, d. The value d_0 was a reference value of the maximum distance from the origin to the farthest point in the simulation:

$$d_0 = \sqrt{(r_{max})^2 + (z_{max})^2}$$

Eq. 4.7

The variable, d, was the distance from the center of the peak oscillation to the particle location:

$$d = \sqrt{(r_{particle} - r_{center})^2 + (z_{particle} - z_{center})^2}$$

Eq. 4.8

87

Consequently, the ratio, d/d_0, could vary from about 0 to 1 over the simulation region. The maximum oscillation potential amplitude, A, was established from the time-varying emissive measurements. The constants C_1, C_2, and C_3 were found from fits to the emissive probe data that determined the envelope of the potential oscillations with distance from the maximum.

Another effect that was included in the simulation was the effect of differences in the oscillation phase between different locations. This effect was modeled as a small amplitude, random modification to the time, t, in the potential oscillation function, $\phi_{osc\_t}(t)$:

$$t = t_i - R \cdot t_{phase} \qquad\qquad \text{Eq. 4.9}$$

Where t was the time used to determine the potential at which the particle was generated, t_i was the average time along in the cycle, R was a random number between 0 and 1, and t_{phase} was the maximum allowable phase difference between points. The value t_i was determined in the simulation by dividing up the oscillation cycle into an even number of increments and then generating particles at each of those points in the cycle. The value t_{phase} was determined from the time-varying emissive probe measurements and could vary from 0 to 1. A value of zero for t_{phase} meant that all of the potentials in the simulation were rising and falling at the same time. Generally, it was found that for case 1, some phase value other than zero (but less than 0.3) was needed to make the simulation results agree with the measurements, whereas for case 2, a phase of zero was suitable. Table 4.1 shows the values used for the potential oscillations in each case. Notice that the main difference between the cases is in the magnitude of the oscillations which were controlled by variables M and A that were obtained from curve fits to probe measurements.

88

Table 4.1 – Values used to describe plasma potential variations.

Variable	Case 1	Case 2
b	0.18	0.00
M	10.0	1.0
A	120.0	2.5
C_1	1.0	1.0
C_2	5.0	5.0
C_3	0.1	0.1
t_{phase}	0.25	0.00

Figure 4.2 shows plots of the potential versus time for each simulation case along with sample measurements from the time-varying emissive probe data. The values for b, M, and A were chosen to reproduce the general shape of the oscillations. The magnitude of the potentials in case 1 was much higher than the magnitude in case 2. Also, the magnitude of the potentials was made to drop off as the distance from the oscillation center point increased.
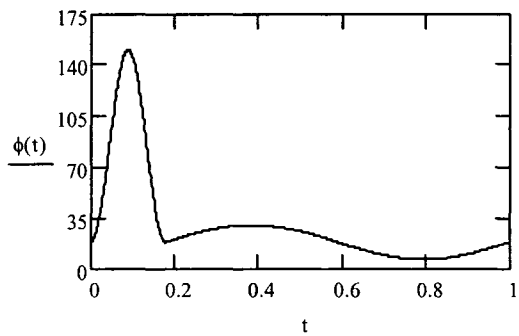
Figure 4.2a Simulated maximum potential oscillation profile (one cycle) versus time for case 1 (b = 0.18, M = 10.0, A = 120.0, ϕ_{avg} = 30 V, r = r_{osc_center}, z = z_{osc_center}).
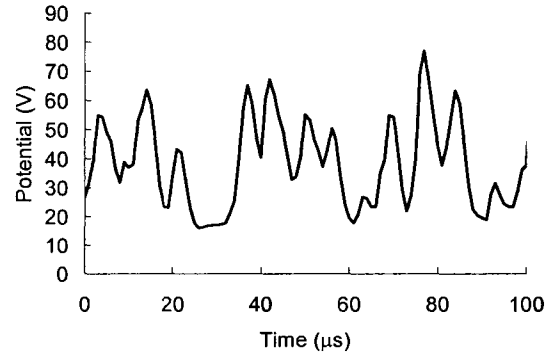
Figure 4.2b Sample time-varying emissive probe measurements for case 1 (Condition 1c, J_D = 11.25 A, $\dot{m}$ = 7.6 sccm Xe, V_D = 34 V, r = -1.5 cm, z = 2.0 cm). Note that the emissive probe was not capable of measuring voltages above 85 V.

89
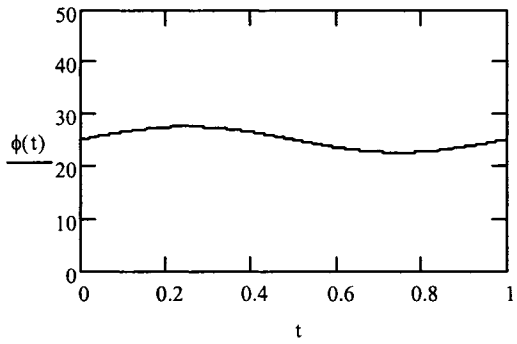
Figure 4.2c Simulated maximum potential oscillation profile (one cycle) versus time for case 2 (b = 0.00, M = 1.0, A = 2.5, ϕ_{avg} = 25 V, r = r_{osc_center}, z = z_{osc_center}).
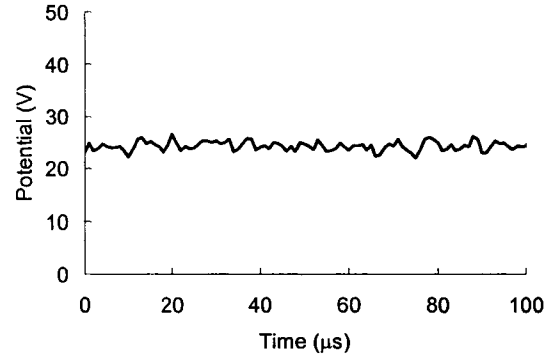
Figure 4.2d Sample time-varying emissive probe measurements for case 2 (Condition 2d, J_D = 13.0 A, $\dot{m}$ = 13.1 sccm Xe, V_D = 25.2 V, r = -0.5 cm, z = 2.0 cm).

One simplifying assumption in the model was that particles were assumed to move in a non time-varying potential field. Instead, the oscillation profile was divided up into snapshots in which the particles were started and assumed to exit a region before the potential profile greatly changed. How much this simplification affects the simulation depends on the frequency of the oscillations as well as the velocity the ions gain as they start to travel from their creation point. The velocity of an ion is given by:

$$v_i = \sqrt{\frac{2 \cdot E_i}{m_i}}$$

Eq. 4.10

Where v_i is the ion velocity, E_i is the ion kinetic energy, and m_i is the ion mass. Also, the distance of travel during one period is:

$$d = \frac{1}{f} \cdot v_i$$

Eq. 4.11

Where d is distance, v_i is velocity, and f is frequency. These equations can be used estimate how far an ion would travel during an oscillation period given a certain energy. For the oscillations in case 1, the frequencies were in the 5 to 50 kHz range. As an

90

example, assuming the frequency was 40 kHz and the ion quickly gained 10 eV of energy, the distance the ion would travel in one cycle would be:

$$d = \frac{1}{f} \cdot \sqrt{\frac{2 \cdot E_i}{m_i}} = \frac{1}{40000\,\frac{1}{s}} \cdot \sqrt{\frac{2 \cdot 10eV \cdot 1.6 \cdot 10^{-19}\,\frac{J}{eV}}{131.3amu \cdot 1.66 \cdot 10^{-27}\,\frac{kg}{amu}}} = 0.096m \qquad \text{Eq. 4.12}$$

This distance is on the order of the simulation region so it is likely that the ion would be moving through at least a partially varying potential region. For more energetic ions or lower frequency oscillations, the ion would travel longer distances and would not see the effects of the potential oscillations as much.

4.5 Simulation Results – Case 1

Operating conditions 1b, 1c, and 1d were examined for the open cathode setup of case 1. Figure 4.3 shows the basic setup of the simulation region along with the relative locations of the cathode, anode, and remotely located ESA. The ESA was positioned about 45 cm downstream of the keeper at radial locations of 0.0, -3.0, and -6.0 cm relative to the cathode centerline. It was estimated that the ESA had an acceptance angle of about 3 degrees based on the aperture dimensions. In reality, the ESA has a conical acceptance because ions can enter the ESA if they have small tangential velocity components and still travel through the spherical ESA segments to the collector plate. However, for this two dimensional simulation, all tangentially directed ions were ignored.

91
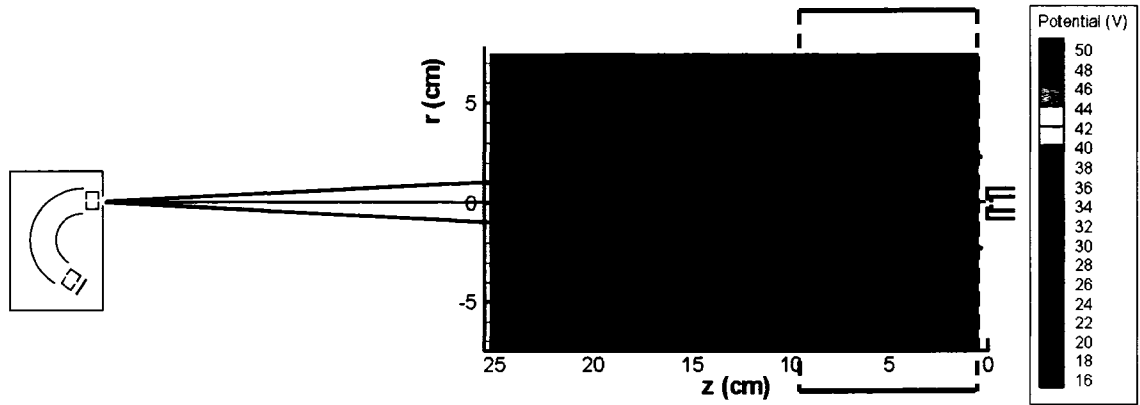
Figure 4.3 Setup of the ESA relative to the simulation region. The ESA was positioned about 45 cm downstream of the keeper (Condition 1d, $J_D = 15.0$ A, $\dot{m} = 7.6$ sccm Xe, $V_D = 33.5$ V). The time-averaged potential profile is shown for reference.

Figure 4.4 illustrates the ion weighting and peak potential oscillation profiles used for case 1. The ion density profile was modeled as a power fit equation with the peak ion density located near the cathode/keeper orifice. The constants in the power fit were determined from the triple Langmuir probe electron density profiles. The potential oscillation profile was modeled as an exponential function with the peak located a few centimeters downstream of the cathode/keeper orifice. The potential profile in Figure 4.4 is modified according to the time during the oscillation cycle and added to the average potential at each location.
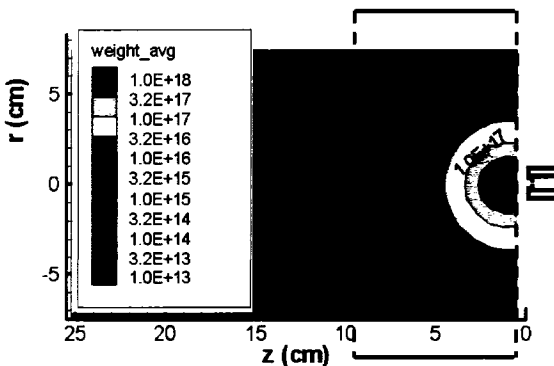
Figure 4.4a Ion weighting profile used for case 1. The peak density was located near the cathode/keeper orifice at r = 0.0 cm, z = 1.0 cm.
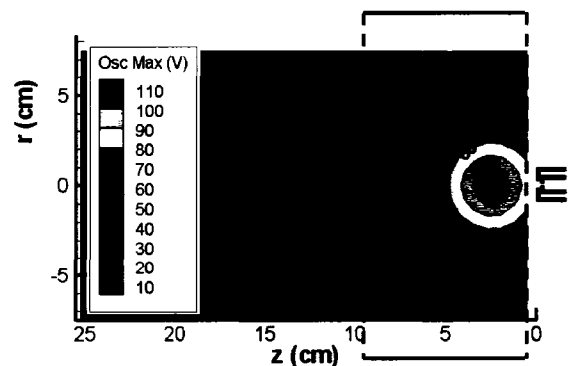
Figure 4.4b Profile of the maximum potential oscillation used for case 1 (A = 120 V). The oscillation peak was centered at r = 0.0 cm, z = 2.5 cm from the cathode.

92

Once the ion density and potential profile was determined for a particular time during the cycle, ions were placed throughout the simulation region and their trajectories were calculated. Each ion trajectory was determined from local electric fields that were calculated from gradients of the plasma potential profile. Figure 4.5 shows the starting point of ions that had trajectories toward the ESA over the entire oscillation cycle for condition 1d. If the calculated trajectory indicated that the ion would travel toward the ESA, and the ion was within the required acceptance angle, the particle was binned according to ion energy to create the IEDF. In most cases, the simulation was run where the initial trajectory of each ion was calculated and the ions were not tracked further. This was done due to the long simulation times required if each ion path was calculated. The energy of the ion was assumed to be equal to the potential difference between the ion starting point and the ESA, which was assumed to be at 0 V.
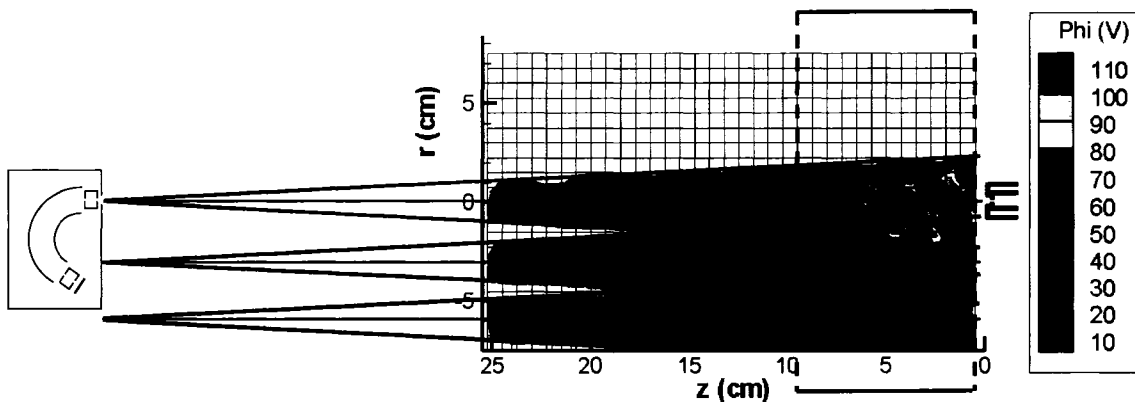
Figure 4.5 Plot of the locations and potentials of ions that were started in the simulation region that were directed toward the ESA and were within the ESA acceptance angle. The ions were binned according to ion energy. Three ESA locations of r = 0.0, -3.0, and -6.0 cm are shown at condition 1d (J_D = 15.0 A, $\dot{m}$ = 7.6 sccm Xe, V_D = 33.5 V).

93

After the particles had been monitored and recorded over the oscillation cycle, the binned particles were used to create the resulting ion energy distribution function. The ions were grouped according to energy and the particle weights were added to determine the relative strength of particles with different energies. Then, the distribution was normalized to the peak value, which typically occurred near the discharge voltage similar to the experimentally measured IEDFs.

Figure 4.6 shows IEDFs from a simulation along with the measured IEDFs from the ESA for operating conditions 1b, 1c, and 1d. First, both the simulation and the ESA measurements showed a main group of ions with energies from about 20 to 50 eV, which was near the discharge voltage. This is expected since a large portion of the oscillation cycle was spent where the potentials in the discharge plasma were near the value that would result in these ion energies. There was also a second group of ions having energies above 50 eV for both the ESA measurements and the simulations. These more energetic ions were produced when the potentials were in the higher portion of an oscillation cycle.
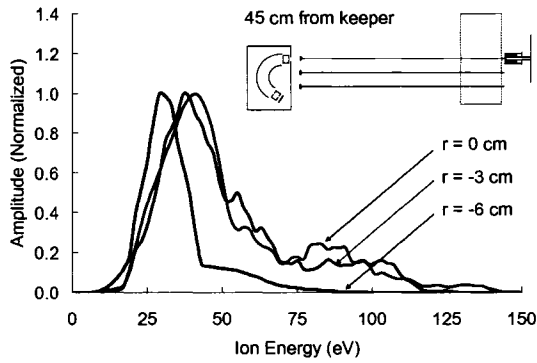
Figure 4.6a Simulation results for condition 1b at radial locations of 0.0, -3.0, and -6.0 cm.
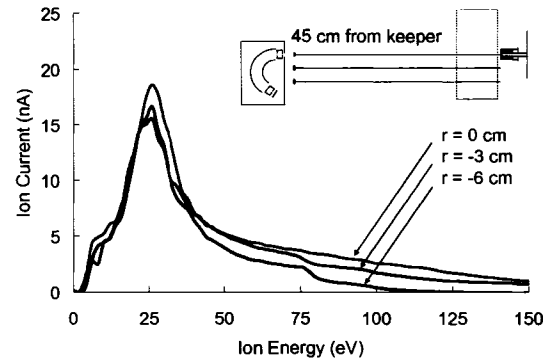
Figure 4.6b Measured IEDF using the ESA for condition 1b ($J_D = 7.5$ A, $\dot{m} = 7.6$ sccm Xe, $V_D = 33$ V).
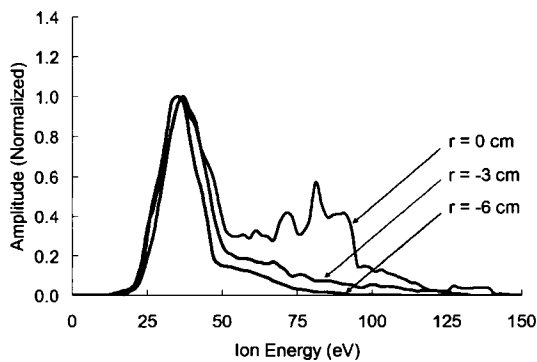
Figure 4.6c Simulation results for condition 1c at radial locations of 0.0, -3.0, and -6.0 cm.
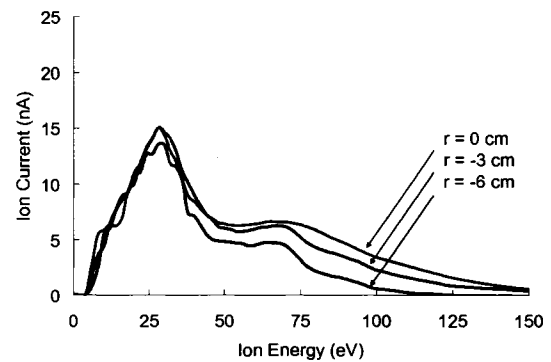
Figure 4.6d Measured IEDF using the ESA for condition 1c ($J_D = 11.25$ A, $\dot{m} = 7.6$ sccm Xe, $V_D = 34$ V).
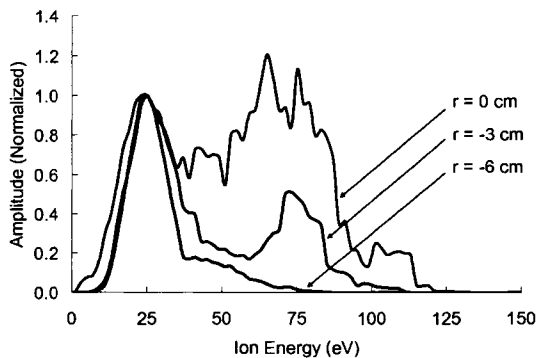
Figure 4.6e Simulation results for condition 1d at radial locations of 0.0, -3.0, and -6.0 cm.
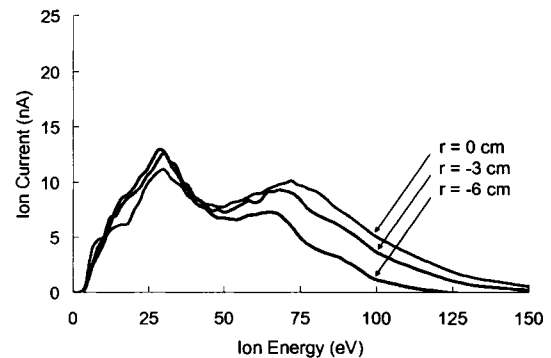
Figure 4.6f Measured IEDF using the ESA for condition 1d ($J_D = 15.0$ A, $\dot{m} = 7.6$ sccm Xe, $V_D = 33.5$ V).

The agreement between general trends in the simulated and measured IEDFs is considered to be quite high. Specifically, the simulation results in Figure 4.6 suggest

95

there were more energetic ions present when the ESA was positioned closer to the cathode centerline (at r = 0.0 cm). This result agrees with both the experimental IEDFs and the emissive probe measurements in which the highest plasma potentials were measured on the cathode centerline. Also similar to the measured distributions from the ESA, the amount of energetic ions in the simulated IEDFs increased relative to the main ion group as the discharge current was changed from 7.5 to 15.0 A (1b-1d). In a more detailed comparison, one can see that the simulated IEDFs slightly overestimate the high ion energy component when the line of sight is along the cathode centerline. The drop in energetic ion content with radial position was more pronounced for the simulated IEDFs.

The shape of the distributions obtained from the simulations could be varied by adjusting the values for the weighting, oscillation profile, oscillation magnitude, or phase. The values used in these simulations were chosen because they gave a reasonable representation of the measured plasma properties from the emissive and triple Langmuir probes. In addition, the chosen simulation parameters also yielded reasonable agreement between the simulated IEDFs and the ESA measurements.

Two variables that had a large effect on the resulting distribution were the amplitude of the oscillations, A, and the time phase, t_{phase}. Figure 4.7a shows the effect of choosing two very different values for the peak-to-peak oscillation amplitude, A, of 10 V versus 120 V. As expected, a lower value for the oscillation amplitude resulted in a distribution with most ions having energies close to the time-averaged potentials.

Figure 4.7b shows the effect of the value for t_{phase} which varied how the potentials were related from location to location at a particular point in time. Values of 0.0 and 0.25 were chosen for t_{phase} with the other parameters held constant. When t_{phase} was set to 0.0,

all of the potentials in the simulation were rising and falling at the same time according to the oscillation profile. When t_{phase} was set to 0.25, more random potential profile gradients were generated which caused a wider energy range of ions to be produced with trajectories heading toward the ESA. It was found that for case 1, some phase value other than zero was needed to make the simulation results agree better with the measurements. Increasing the value of t_{phase} from 0.0 to 0.25 caused the number of energetic ions to increase relative to the main ion group.
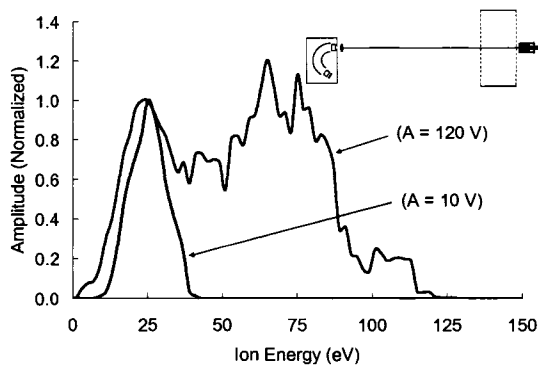
Figure 4.7a   Effect of the oscillation amplitude, A, on the resulting ion energy distribution function (condition 1d).
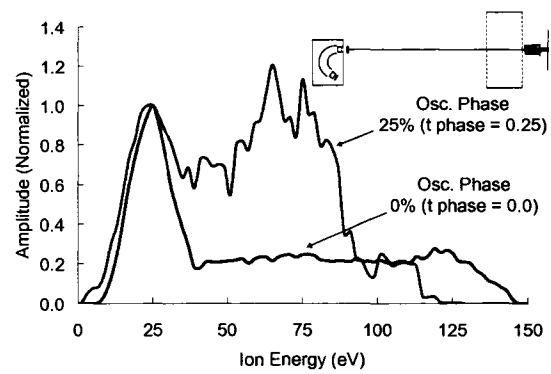
Figure 4.7b   Effect of the oscillation time phase, t_{phase}, on the resulting ion energy distribution function (condition 1d).

4.6 Simulation Results – Case 2

The simulation was also exercised for conditions 2d and 2f for the prototype NSTAR discharge chamber configuration (case 2). At each condition, the simulation was run with the ESA positioned at angular locations of 0, 15, 30, and 90 degrees relative to the cathode centerline. The ESA entrance point was positioned at 55 cm from the cathode in all cases. Figure 4.8 and Figure 4.9 show the simulation setup with the approximate angles of acceptance to the ESA for conditions 2d and 2f, respectively.

97

Binned particles are shown that had the proper position and trajectory to be accepted into the ESA over the entire oscillation cycle.

The amplitude of the oscillations, A, was set to 2.5 V based on the time-varying emissive probe measurements. Although the amplitudes of the potential oscillations were relatively small in case 2 compared to case 1, the oscillations were included because they would affect the widths of the IEDFs. The phase value, t_{phase}, was set to 0.0 based on the time-varying multiple emissive probe experiments, which showed only small variations of the potential oscillations with position. The ions were binned according to energy and the particle weights were added to determine the relative strength of particles with different energies.

Two different regions were used in the simulation for the prototype NSTAR configuration. One region was used for the 0, 15, and 30 degree angles and a separate region was used for the 90 degree angle. At the 0, 15, and 30 degree angles, ions were accepted to the ESA from both inside and outside the discharge chamber. Although it appears more ions came to the ESA from outside the discharge chamber, especially in the 15 and 30 degree cases, these ions carried much less weight than the ions created closer to the cathode region. At the 90 degree angle, most of the accepted ions originated from either near the anode or outside of the discharge chamber. This was because ions formed inside the discharge chamber were directed on paths toward the center of the discharge chamber.

98
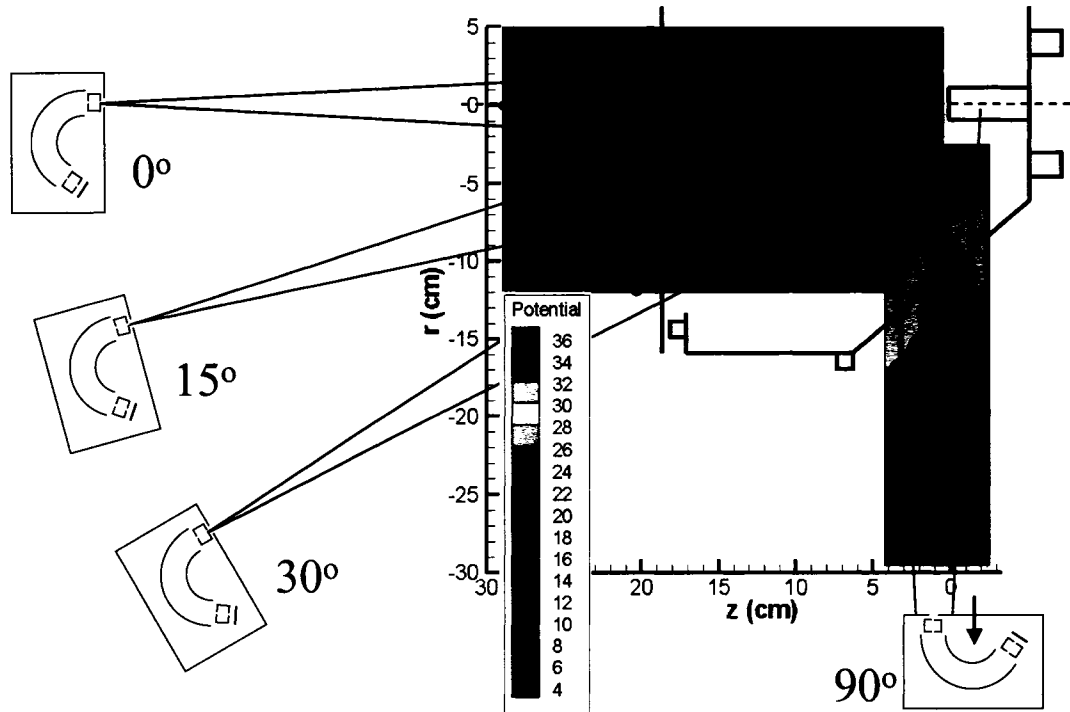
Figure 4.8 Simulation setup at condition 2d for the prototype NSTAR discharge chamber (J_D = 13.0 A, $\dot{m}$ = 13.1 sccm Xe, V_D = 25.2 V). Binned particles are shown that had the proper position and trajectory toward the ESA to be measured. The time-averaged potential profile is shown for reference.
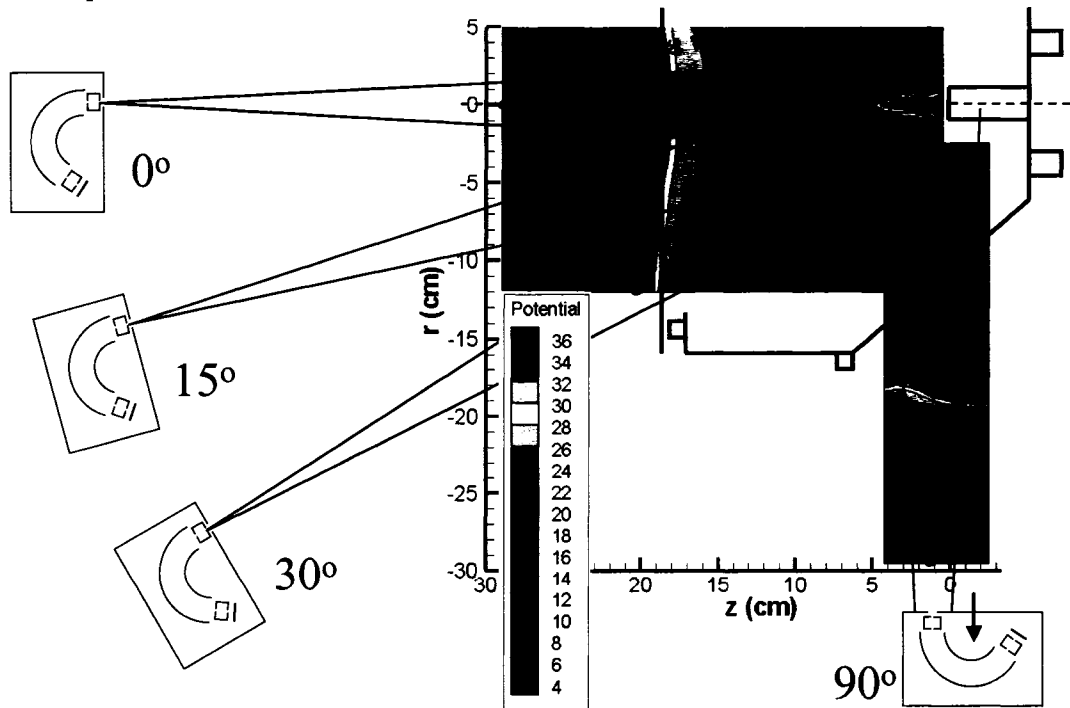
Figure 4.9 Simulation setup at condition 2f for the prototype NSTAR discharge chamber (J_D = 18.0 A, $\dot{m}$ = 8.3 sccm Xe, V_D = 36.0 V). Binned particles are shown that had the proper position and trajectory toward the ESA to be measured.

99

For case 2, the distributions were normalized to the peak of the distribution at the 0 degree zenith angle. The resulting distributions are shown in Figure 4.10 along with ESA measurements made at the same positions relative to the cathode. Looking first at the simulation results, the IEDF was much stronger at the 0 degree zenith angle. As the simulated ESA position was varied to 15 and 30 degrees, the distribution magnitude dropped. The magnitude of the distribution was also lower at the 90 degree angle. In all cases, the widths of the IEDFs were similar.

Trends observed in the simulations were also observed in ESA data. One example is the similarity between the most probable energies of the ions. At condition 2d where the discharge voltage was around 25 V, ions with energies in the 20 to 30 eV range were recorded in the simulation and measured with the ESA. Similarly, at condition 2f where the discharge voltage was 36 V, ions with energies in the 25 to 40 eV range were recorded. It appears that ions were able to leave the discharge region and enter the ESA most readily at the 0 degree zenith angle. Also, in both the simulation and measurements, the most probable energy of the distribution increased slightly as the ESA was moved from 0 to 30 degrees. This may be because ions created at slightly lower energies (15 to 24 eV) near the pseudo-screen grid were not directed toward the ESA (when positioned at a zenith angle of 30 degrees) in a manner that would allow them to flow through the ESA collimators.

Another similarity between the simulation and measurement was at the 90 degree angle for condition 2f where two groups of ions were seen. One ion group had an energy near 26 eV and the second ion group had an energy near 36 eV. This makes sense if one

100

re-examines Figure 4.9 for the time-averaged plasma potential profile. The plasma

potential near the anode was about equal to the discharge voltage of 36 V and the

potential farther outside of the anode was near 26 V.
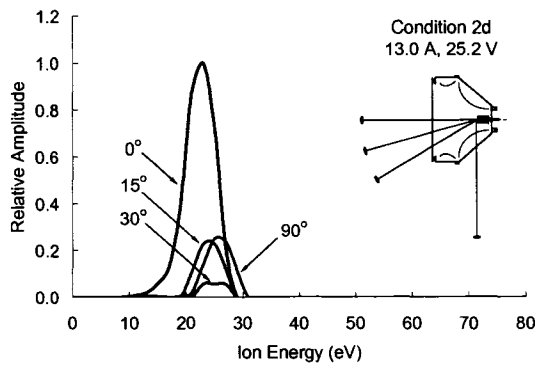
Figure 4.10a   Simulation results for
condition 2d at zenith angles of 0, 15, 30,
and 90 degrees.
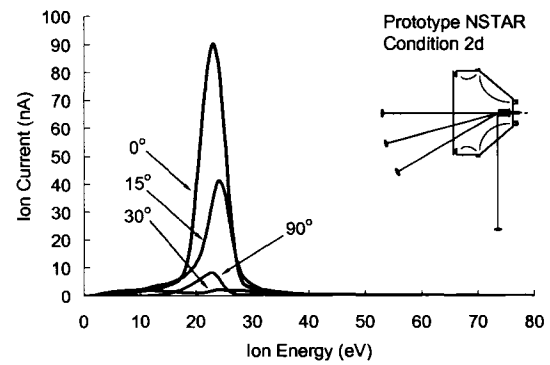
Figure 4.10b   ESA measurements for
condition 2d.
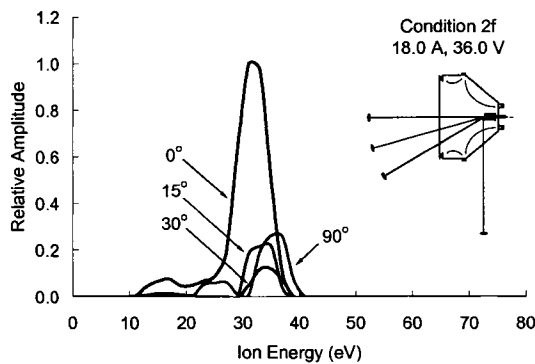
Figure 4.10c   Simulation results for
condition 2f at zenith angles of 0, 15, 30,
and 90 degrees.
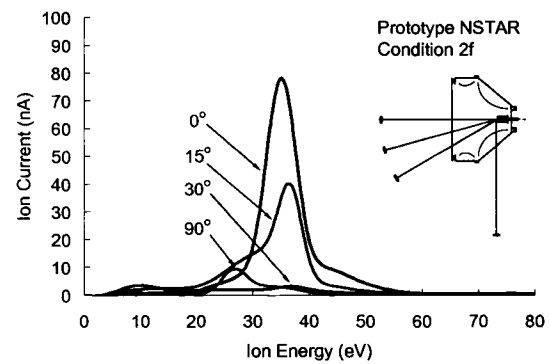
Figure 4.10d   ESA measurements for
condition 2f.

One part of the measured distributions that the simulations did not reproduce well

was the small number of energetic ions with energies above the cathode-to-anode

potential difference in the 35 to 70 eV range (see Figure 4.10 and Figure 3.27). In the

simulations of case 1, the energetic ions observed in the simulations were produced when

the plasma potentials were at the higher potential regions of the oscillation cycle. There

were potential oscillations observed in the prototype NSTAR discharge chamber, but the

amplitudes of the oscillations in this region were measured to be ±2.5 V, or only about 5 to 15 % of the discharge voltage. One possibility is that there were higher frequency potential spikes (>500 kHz) at some locations that were not measured by the time-varying emissive probe measurements. This isn't considered likely because the frequency spectral power was decreasing rapidly with frequency at frequencies above 100 kHz. Also, it is possible that energetic ions could be produced at locations that were not probed by the emissive and triple Langmuir probes (e.g., regions closer to the cathode). One final possibility is that emissive probes can indicate plasma potentials lower than actual values when placed in dense plasma or when not operated at adequate temperatures. Tests were conducted at higher emissive probe heating current (to the point right before the filament burned out), but only modestly higher plasma potentials were detected in the regions nearby the cathode.

One proposed mechanism of energetic ion production proposed by Katz at al.[32] that is not considered in the simulations for creating energetic ions is the possibility of having multiple charge exchange reactions that cause the ions to alternately gain kinetic energy, then potential energy, and again kinetic energy via the potential well that exists nearby the hollow cathode. In the DC plasma potential field, most of the energetic ions produced in this manner would have trajectories in directions perpendicular to the cathode axis (~ 90 degrees). It is pointed out that for the prototype NSTAR ESA measurements described herein, a small number of energetic ions were observed at zenith angles ranging from 0 to 90 degrees where the largest fractions of energetic ions were usually seen at the 30 degree angle. Therefore, the particles would need to undergo scattering collisions as well as the multiple charge exchange reactions to be observed by

102

the ESA at small zenith angles. One final possibility not pursued in the current research is multiple charge exchange/ionization reactions that occur at different phases of the plasma potential oscillation cycle that result in energetic ion formation. This explanation is not considered likely due to the fact that a 50 eV ion travels most of the way through the discharge chamber volume during a small fraction of a typical oscillation period.

5 Discussion and Conclusions

5.1 Summary – Case 1: Open Cathode Configuration

Overall, two different discharge configurations were studied using a combination of direct and remotely located probes. The open cathode, no magnetic field configuration of case 1 produced a very unstable plasma, especially at high discharge current operating conditions (1b-1e). The emissive and triple Langmuir probe time-averaged measurements showed the presence of a potential hill that existed just downstream of the hollow cathode exit. Near the peak potential location, the potentials were higher than the cathode-to-anode potential difference. In addition to the potential hill, the emissive probe time-varying measurements showed large amplitude potential oscillations with peak potentials exceeding the emissive probe circuitry limit of 85 V. This was compared to a cathode-to-anode potential difference of 30 to 40 V. The largest oscillations also occurred near the cathode, but at slightly different locations (typically closer to the cathode) than the peak of the DC potential hill.

Corresponding to these large potential oscillations observed with the emissive probe, a remotely located ESA_ExB probe measured ions having a wide range of energies from 10 eV all the way up to 150 eV. Given the presence of large amplitude potential oscillations, one would expect the ESA would measure ions with a wide range of energies flowing from the plasma. It was observed that as the discharge current was increased from 7.5 to 15.0 A, the relative number of energetic ions increased (conditions 1b-1d). The simulations showed similar trends when including effects for (1) large potential oscillations and (2) regions of non-uniform fluctuations. More energetic ions

104

cause higher rates of erosion due to higher sputter yield, and, all other factors being equal, components within the discharge chamber would erode less and last longer if the energy and production rate of energetic ions could be reduced. The most likely method of reducing ion energy is by reducing or eliminating large amplitude potential oscillations.

When the ExB section of the ESA_ExB probe was used to measure the number of singly and doubly charged ions, the same trend was followed as with the ion energies where the relative number of doubly charged ions increased as the discharge current was increased. Also, it was found that the ratio of doubly charged ions to singly charged ions increased as the energy of the ions increased. This means that a portion of ions in the distribution were not only more energetic, but they were also composed of larger fractions of multiply charged ions. The combination of higher energies and multiple charge states would cause increased erosion to components such as the cathode assembly and screen grid. Therefore, reducing the number of energetic ions that are created may be important for not only reducing the overall energy of the ions, but also for reducing the fraction of multiply charged ions.

105

5.2 Summary – Case 2: Prototype NSTAR Configuration

In case 2, the cathode was setup in a discharge chamber configuration similar to an NSTAR ion thruster. The prototype NSTAR discharge chamber had a more confined geometry compared to the open cathode configuration and included a magnetic field to enhance plasma production. Here, the emissive and triple Langmuir probes measured potentials that were near or just above the anode voltage. Plasma potential dropped as the probe was moved close to the cathode, to within a couple of centimeters of radius from the cathode/keeper orifice. The time-varying emissive probe measurements showed low amplitude potential oscillations on the order of 5 to 15 % of the discharge voltage. Like the results from case 1, the amplitude of the oscillations increased as the ratio of discharge current-to-flow rate was increased.

The remotely located ESA_ExB probe showed ions with energies near the anode voltage. This result was both encouraging and consistent with the direct probes considering that the plasma potentials measured inside the discharge chamber were also near the anode voltage. For the prototype NSTAR configuration, the ESA was also used to measure the IEDF of ions flowing from zenith angles of 0 to 90 degrees with respect to the cathode centerline. The largest numbers of ions were observed on the cathode axis at 0 degrees. This result agreed with the simulation model, which showed that ions were directed along paths normal to the pseudo-screen grid due to the potentials that developed in the exit slot region of this electrode. At the 90 degree angle, the simulations showed that most of the ions observed by the ESA would originate from near the anode and outside the discharge chamber. This was because ions inside the discharge chamber were directed away from the sidewall anode and could not overcome the negative potential

106

gradient to exit the discharge chamber in this direction. Ions formed in the near cathode region would not be able to exit the discharge chamber in the directions measured using the ESA (zenith angles from 0 to 90 degrees) due to negative potential gradients. Therefore, the direct probes become more useful than the remote probes for measuring ions produced near the cathode. The simulations were not able to reproduce the small number of energetic ions observed with the ESA due to the lack of high amplitude oscillations in the discharge.

The ExB measurements for the conditions of case 2 showed that the doubles-to-singles ratio increased as the energies of the ions increased. Therefore, ions in the tail of the ion energy distribution would contribute to cathode erosion from the combination of higher energies and multiple charge states. While some erosion to the hollow cathode and keeper in the prototype NSTAR discharge chamber would be caused by energetic singly charged ions in the tail of the ion energy distribution, most erosion would be caused by doubly charged ions which strike cathode potential surfaces at higher energies compared to singly charged ions.

5.3 Suggestions for Future Work

The overall focus of the research was to investigate and characterize the plasma produced downstream of a hollow cathode with the goal of identifying groups of ions and possible mechanisms that might cause erosion. Suggestions for further study, additional experiments, and modeling improvements are briefly described that would lead to increased understanding of the discharge plasma.

1) Measurements were made of the plasma potentials, ion energies, and charge states at different operating conditions. The next step might be to try and relate these measurements to erosion to the hollow cathode by including estimates for the sputtering capability of the ions. For example, based on the measured IEDFs and charge state data, determine which groups of ions are most likely responsible for cathode erosion[34].

2) A continued study of plasma potential oscillations using emissive/triple probes. In this research, remotely measured IEDFs were found to be largely affected by the time-varying plasma potential structures that were present in the plasma. While some progress was made using two emissive probes placed in the plasma, there is likely much more information to be gained by studying the plasma oscillations. Multiple probes placed at various locations could be used to determine relationships between possible waves in the plasma and/or dependencies of the potential oscillation frequencies and magnitudes.

3) The remotely located ESA_ExB is useful for determining ion energies and charge states. However, with the remotely located probes, there are challenges with determining the production regions of selected groups of ions with given energies and

charge states. In this research, the remote probes were moved to various positions and angles to try and determine the production locations of groups of ions. One idea for improving the measurements is to position the ESA_ExB over a wider range of zenith angles from 0 to 180 degrees to measure the energy and charge state of ions flowing in all directions from the plasma. Another idea is to add an isolating (or plasma shielding) tube to the entrance of the ESA to be able to look in to the plasma and measure the ion energies and charge states of local regions of the plasma.

4) One study performed during this research that showed promise was to introduce a second type of propellant into the primarily xenon plasma. A small amount of krypton was introduced at selected locations to look for the ion energies and charge states of the krypton ions compared to the xenon ions in the remotely located probes. The resulting energies and charge states of the krypton ions could give information about local plasma potentials and ion production rates. Similarly, effects of propellant introduction at different locations could be studied with regard to plasma potential and oscillation amplitude.

5) The simulation model created to examine the correlation of the direct and remote measurements could be improved by 1) including effects for charge exchange reactions in the plasma and downstream regions, 2) including a changing potential profile while tracking the particles through the simulation, 3) including doubly charged ion production as well and singly charged ion production, and 4) better understanding of the plasma potential and density variations with position and phase during oscillation cycles.

6 References

Electric Propulsion

[1] Wilbur, P.J., Jahn, R.G., and Curran, F.C., "Space Electric Propulsion Plasmas," IEEE Transactions on Plasma Science, Vol. 19, No. 6, pp. 1167-1179, December 1991.

[2] Jahn, R.G. and Choueiri, E.Y., "Electric Propulsion," Encyclopedia of Physical Science and Technology, Third Edition, Vol. 5, pp. 125-141, 2002.

[3] Brophy, J.R., "Ion Thruster Performance Model," NASA CR-174810, Colorado State University, Fort Collins, CO, December 1984.

[4] Wilbur, P.J., Rawlin, V.K., and Beattie, J.R., "Ion Thruster Development Trends and Status in the United States," Journal of Propulsion and Power, Vol. 14, No. 5, pp. 708-715, September-October 1998.

[5] Goebel, D.M., Wirz, R.E., and Katz, I., "Analytical Ion Thruster Discharge Performance Model," AIAA-2006-4486, 42nd Joint Propulsion Conference and Exhibit, Sacramento, CA, July 2006.

Ion Optics

[6] Farnell, C.C., "Performance and Lifetime Simulation of Ion Thruster Optics," Ph.D. Dissertation, Department of Mechanical Engineering, Colorado State University, 2007.

[7] Polk, J., Brophy, J., Shih, W., Beatty, J., Laufer, D.M., Wilbur, P., and Williams, J., "Large Carbon-Carbon Grids for High Power, High Specific Impulse Ion Thrusters," Space Technology and Applications International Forum Proceedings, Albuquerque, NM, February 2003.

Hollow Cathode Operation

[8] Polk, J., Marrese, C., Thornber, B., Dang, L., and Johnson, L., "Temperature Distributions in Hollow Cathode Emitters," AIAA-2004-4116, 40th Joint Propulsion Conference and Exhibit, Fort Lauderdale, FL, July 2004.

[9] Polk, J.E., Goebel, D.M., Watkins, R., Jameson, K., Yoneshige, L., Przybylowski, J., and Chu, L., "Characterization of Hollow Cathode Performance and Thermal Behavior," AIAA-2006-5150, 42nd Joint Propulsion Conference and Exhibit, Sacramento, CA, July 2006.

[10] Polk, J.E., "The Effect of Reactive Gases on Hollow Cathode Operation," AIAA-2006-5153, 42nd Joint Propulsion Conference and Exhibit, Sacramento, CA, July 2006.

Hollow Cathode Erosion

[11] Domonkos, M.T. and Williams, Jr., G.J., "Investigation of Keeper Erosion in the NSTAR Ion Thruster," IEPC-01-308, 27th International Electric Propulsion Conference, Pasadena, CA, October 2001.

[12] Williams, Jr., G.J., Domonkos, M.T., and Chavez, J.M., "Measurement of Doubly Charged Ions in Ion Thruster Plumes," IEPC-01-310, 27th International Electric Propulsion Conference, Pasadena, CA, October 2001.

[13] Vaughn, J.A., Schneider, T.A., Polk, J.E., Goebel, D.M., Ohlinger, W., and Hill, D.N., "NEXIS Reservoir Cathode 2000 Hour Proof-Of-Concept Test," AIAA-2004-4203, 40th Joint Propulsion Conference and Exhibit, Fort Lauderdale, FL, July 2004.

[14] Brophy, J.R. and Garner, C.E., "Tests of High Current Hollow Cathodes for Ion Engines," AIAA-88-2913, 24th Joint Propulsion Conference, Boston, MA, July 1988.

[15] Kamhawi, H., Soulas, G.C., Patterson, M.J., and Frandina, M.M., "NEXT Ion Engine 2000 hour Wear Test Plume and Erosion Results," AIAA-2004-3792, 40th Joint Propulsion Conference and Exhibit, Fort Lauderdale, FL, July 2004.

[16] Mikellides, I.G., Katz, I., Goebel, D.M., Jameson, K.K., and Polk, J.E., "The Partially-Ionized Gas and Associated Wear in Electron Sources for Ion Propulsion, II: Discharge Hollow Cathode," AIAA-2007-5192, 43rd Joint Propulsion Conference and Exhibit, Cincinnati, OH, July 2007.

[17] Friedly, V.J., "Hollow Cathode Operation at High Discharge Currents," NASA CR-185238, Colorado State University, Fort Collins, CO, April 1990.

Sputtering

[18] Yalin, A.P., Williams, J.D., Surla, V., Wolf, J., and Zoerb, K.A., "Azimuthal Differential Sputter Yields of Molybdenum by Low Energy Xe^+ Bombardment," AIAA-2006-4336, 42nd Joint Propulsion Conference and Exhibit, Sacramento, CA, July 2006.

[19] Doerner, R.P., Whyte, D.G., and Goebel, D.M., "Sputtering yield measurements during low energy xenon plasma bombardment," Journal of Applied Physics, Vol. 93, No. 9, pp. 5816-5823, 2003.

111

Cathode Erosion Mechanisms

[20] Williams, J.D. and Wilbur, P.J., "Electron Emission from a Hollow Cathode-Based Plasma Contactor," Journal of Spacecraft and Rockets, Vol. 29, No. 6, pp. 820-829, November-December 1992.

[21] Kameyama, I. and Wilbur, P.J., "Potential-Hill Model of High-Energy Ion Production near High-Current Hollow Cathodes," ISTS 98-a-2-17, 21st International Symposium on Space Technology and Science, Sonic City, Omiya, Japan, May 1998.

[22] Crofton, M.W. and Boyd, I.D., "Plume Measurement and Modeling Results for a Xenon Hollow Cathode," AIAA-2002-4103, 38th Joint Propulsion Conference and Exhibit, Indianapolis, IN, July 2002.

[23] Katz, I., Anderson, J.R., Goebel, D.M., Wirz, R., and Sengupta, A., "Plasma Generation Near an Ion Thruster Discharge Chamber Hollow Cathode," AIAA-2003-5161, 39th Joint Propulsion Conference and Exhibit, Huntsville, AL, July 2003.

[24] Hantzsche, E., "Theory of the expanding plasma of vacuum arcs," Journal of Physics D: Applied Physics, Vol. 24, No. 8, pp. 1339-1353, 1991.

[25] Kameyama, I., "Effects of Neutral Density on Energetic Ions Produced Near High-Current Hollow Cathodes," NASA CR-204154, Colorado State University, Fort Collins, CO, October 1997.

[26] Foster, J.E. and Patterson, M.J., "Characterization of downstream ion energy distributions from a high current hollow cathode in a ring cusp discharge chamber," AIAA-2003-4865, 39th Joint Propulsion Conference and Exhibit, Huntsville, AL, July 2003.

[27] Domonkos, M.T., Foster, J.E., Soulas, G.C., and Nakles, M., "Testing and Analysis of NEXT Ion Engine Discharge Cathode Assembly Wear," AIAA-2003-4864, 39th Joint Propulsion Conference and Exhibit, Huntsville, AL, July 2003.

[28] Herman, D.A. and Gallimore, A.D., "Discharge Chamber Plasma Potential Mapping of a 40-cm NEXT-type Ion Engine," AIAA-2005-4251, 41st Joint Propulsion Conference and Exhibit, Tucson, AZ, July 2005.

[29] Herman, D.A. and Gallimore, A.D., "Near Discharge Cathode Assembly Plasma Potential Measurements in a 30-cm NSTAR-type Ion Engine amidst Beam Extraction," AIAA-2004-3958, 40th Joint Propulsion Conference and Exhibit, Fort Lauderdale, FL, July 2004.

[30] Goebel, D.M., Jameson, K., Katz, I., and Mikellides, I.G., "Energetic Ion Production and Keeper Erosion in Hollow Cathode Discharges," IEPC-2005-266, 29th International Electric Propulsion Conference, Princeton, NJ, October-November 2005.

[31] Martin, R.H., Farnell, C.C., and Williams, J., "Direct and Remote Measurements of Plasma Properties nearby Hollow Cathodes," IEPC-2005-294, 29th International Electric Propulsion Conference, Princeton, NJ, October-November 2005.

[32] Katz, I., Mikellides, I.G., Goebel, D.M., Jameson, K.K., and Johnson, L.K., "Production of High Energy Ions Near an Ion Thruster Discharge Hollow Cathode," AIAA-2006-4485, 42nd Joint Propulsion Conference and Exhibit, Sacramento, CA, July 2006.

[33] Choueiri, E.Y., "Plasma oscillations in Hall thrusters," Physics of Plasmas, Vol. 8, No. 4, pp. 1411-1426, April 2001.

Experimental Setup - Prototype NSTAR Discharge Chamber

[34] Farnell, C.C. and Williams, J.D., "Measurement of Ion Energy Distributions Produced within an NSTAR Discharge Chamber," AIAA-2004-3432, 40th Joint Propulsion Conference and Exhibit, Fort Lauderdale, FL, July 2004.

[35] Rawlin, V.K., Sovey, J.S., Hamley, J.A., Bond, T.A., Matranga, M., and Stocky, J.F., "An Ion Propulsion System for NASA's Deep Space Missions," AIAA-1999-4612, 35th Joint Propulsion Conference and Exhibit, Los Angeles, CA, June 1999.

[36] Foster, J.E., Soulas, G.C., and Patterson, M.J., "Plume and Discharge Plasma Measurements of an NSTAR-type Ion Thruster," AIAA-200-3812, 36th Joint Propulsion Conference and Exhibit, Huntsville, AL, July 2000.

[37] Foster, J.E, "Ion and Electron Transport in an NSTAR-Derivative Ion Thruster," NASA TM-2001-210669-REV1, June 2001.

[38] Herman, D.A., McFarlane, D.S., and Gallimore, A.D., "Discharge Plasma Parameters of a 30-cm Ion Thruster Measured without Beam Extraction using a High-Speed Probe Positioning System," IEPC-03-0069, 28th International Electric Propulsion Conference, Toulouse, France, March 2003.

Remote Diagnostics – ESA and ExB Probes

[39] ESA Operating Manual, Model AC-901, Double Focusing Electrostatic Energy Analyzer, Comstock Inc., Oak Ridge, TN, 37830.

[40] Dahl, D.A., SIMION 3D Version 7.0, Idaho National Engineering and Environmental Laboratory, BECHTEL BWXT IDAHO, LLC, 2000.

[41] Vahrenkamp, R.P., "Measurement of Double Charged Ions in the Beam of a 30 cm Mercury Bombardment Thruster," AIAA-73-1057, 10th Electric Propulsion Conference, Lake Tahoe, NV, October-November 1973.

[42] Hofer, R.R. and Gallimore, A.D., "Ion Species Fractions in the Far-Field Plume of a High-Specific Impulse Hall Thruster," AIAA-2003-5001, 39th Joint Propulsion Conference and Exhibit, Huntsville, AL, July 2003.

Direct Diagnostics - Langmuir and Emissive Probes

[43] Beal, B.E., "Clustering of Hall Effect Thrusters for High-Power Electric Propulsion Applications," Ph.D. Dissertation, Department of Aerospace Engineering, University of Michigan, 2004.

[44] Herman, D.A. and Gallimore, A.D., "Discharge Chamber Plasma Structure of a 30-cm NSTAR-type Ion Engine," AIAA-2004-3794, 40th Joint Propulsion Conference and Exhibit, Fort Lauderdale, FL, July 2004.

[45] Goebel, D.M., Jameson, K.K., Watkins, R.M., Katz, I., and Mikellides, I.G., "Hollow cathode theory and experiment. I. Plasma characterization using fast miniature scanning probes," Journal of Applied Physics, 98, 113302, December 2005.

[46] Chen, S.L. and Sekiguchi, T., "Instantaneous Direct-Display System of Plasma Parameters by Means of Triple Probe," Journal of Applied Physics, Vol. 36, No. 8, pp. 2363-2375, August 1965.

[47] Beal, B.E., Gallimore, A.D., and Hargus, Jr., W.A., "Plasma properties downstream of a low-power Hall thruster," Physics of Plasmas, 12, 123503, December 2005.

[48] Diamant, K.D., "Plasma Measurement in a Resonant Cavity Hollow Cathode," AIAA-2006-5154, 42nd Joint Propulsion Conference and Exhibit, Sacramento, CA, July 2006.

[49] Smirnov, A., Raitses, Y., and Fisch, N.J., "Plasma measurements in a 100 W cylindrical Hall thruster," Journal of Applied Physics, Vol. 95, No. 5, pp. 2283-2292, March 2004.

[50] Goebel, D.M., Personal Communication, Jet Propulsion Laboratory, California Institute of Technology, Pasadena, CA, 91109, September 2006.

[51] Tilley, D.L., Gallimore, A.D., Kelly, A.J., and Jahn, R.G., "The adverse effect of perpendicular ion drift flow on cylindrical triple probe electron temperature measurements," Review of Scientific Instruments, Vol. 65, No. 3, pp. 678-681, March 1994.

114

Plasma Oscillations

[52] Farshi, E., Fukuyama, T., Matsukuma, M., and Kawai, Y., "Non-Maxwellian Shape of Electron Distribution Function in Ion Acoustic Turbulence," IEEE Transactions on Plasma Science, Vol. 29, No. 6, pp. 907-910, December 2001.

[53] Rognlien, T.D. and Self, S.A., "Ion-Acoustic Instability of a Two-Temperature, Collisional, Fully Ionized Plasma," Physical Review Letters, Vol. 27, No. 12, pp. 792-795, September 1971.

[54] Fitzgerald, D.J., "Plasma Fluctuations in Ion Thrusters Utilizing Hollow Cathodes," Ph.D. Dissertation, Department of Mechanical Engineering, Colorado State University, 1983.

[55] Tanaca, H., Hirose, A., and Koganei, M., "Ion-Wave Instabilities in Mercury-Vapor Plasama," Physical Review, Vol. 161, No. 1, pp. 94-101, September 1967.

7   Appendix A – Prototype NSTAR Magnetic Field

A two-dimensional map of the magnetic field inside the prototype NSTAR discharge chamber was completed. The magnetic field was measured in a single plane using a 2-axis magnetic field probe that was positioned throughout the interior of the discharge chamber using an x-y positioning stage. Measurements were made so that comparisons between the prototype chamber and an actual NSTAR discharge chamber could be performed.

The magnetic field setup is shown in Figure 7.1 with the probe positioned on the discharge chamber centerline. The magnetic field is generated in the chamber using three samarium cobalt magnet rings. The first ring was located near the exit of the source (where the ion optics would be located on an actual NSTAR ion engine) at one end of the cylindrical sidewall section, the second was placed at the intersection of the cylindrical and conical anode sections, and the third behind the cathode on the back plate. The probe was used to measure the magnetic field in both the axial (B_z) and radial directions (B_r). The directional measurements were then combined to obtain the magnitude of the magnetic field at each location (i.e., $B = (B_z^2 + B_r^2)^{0.5}$). The pseudo-screen grid and cathode/keeper assemblies were removed to enable measurements throughout the interior of the discharge chamber. The slot cut in the conical sidewall section was positioned to be in the plane where the magnetic field was measured. This allowed the probe to be pushed through the sidewall at these locations to measure the field over a uniform rectangular region.

116
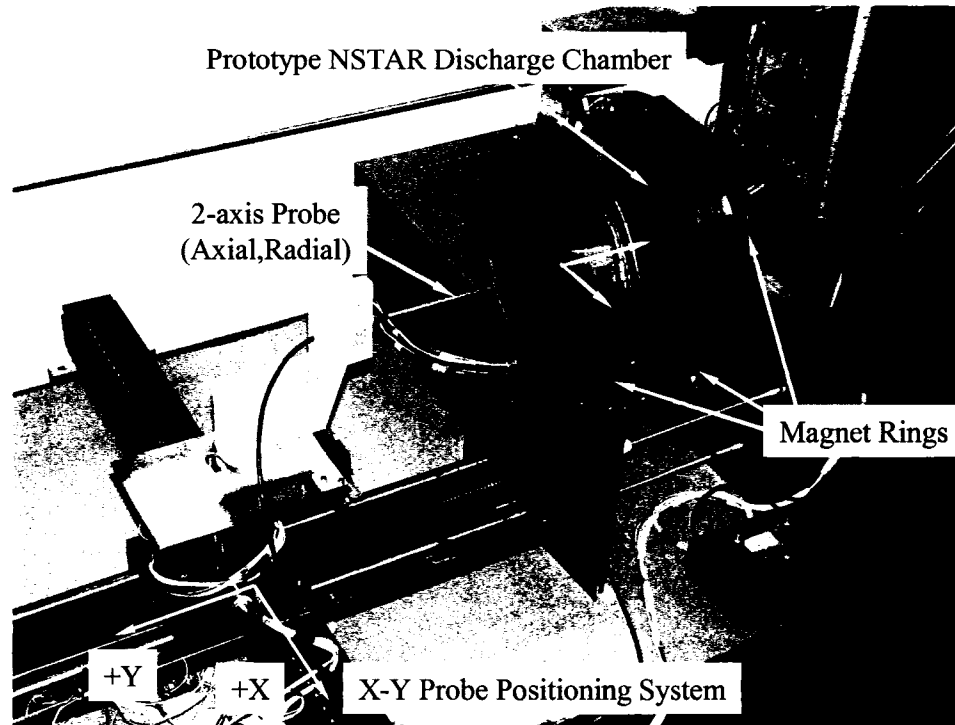
Figure 7.1 Experimental setup showing the prototype NSTAR discharge chamber and the magnetic field probe mounted on an x-y positioning system.

Figure 7.2 shows the measured constant magnitude magnetic field lines and Figure 7.3 shows selected magnetic field lines within the discharge chamber region. An outline of the prototype NSTAR chamber is also shown for reference to the locations of the chamber walls and magnet rings. The magnetic field was found to be symmetric about the centerline by measuring the field in a few select locations, and so the mapped field measured on one side was mirrored on the opposite side to show the entire chamber. The field was measured axially from the back of the chamber (0 cm) out to about 7 cm beyond where the pseudo-screen grid would be placed. In the radial direction, the field was measured from the centerline out to about 14 cm.

As expected, the magnetic field strength was highest near the back (near cathode) magnet ring which consisted of stacks of three magnets. The stacks of three magnets each were placed directly onto an annular iron (4330 steel) pole piece. The pole piece is

117

similar (but not identical) to the one used on the flight NSTAR thrusters, which serves to increase the magnetic field strength near the cathode. The magnetic field was also significant near the other two magnet rings located at axial positions of 12 and 23 cm from the back wall. The first magnetic field contour to close was the one corresponding to ~20 Gauss, which is believed to be in reasonable agreement to measurements made on NSTAR flight and EM model thrusters. For most of the volume within the discharge chamber, the magnetic field strength was about 5 to 30 Gauss. At the cathode orifice location, the field strength was found to be about 80 to 85 Gauss, which is near the values measured in flight and EM model NSTAR thrusters.
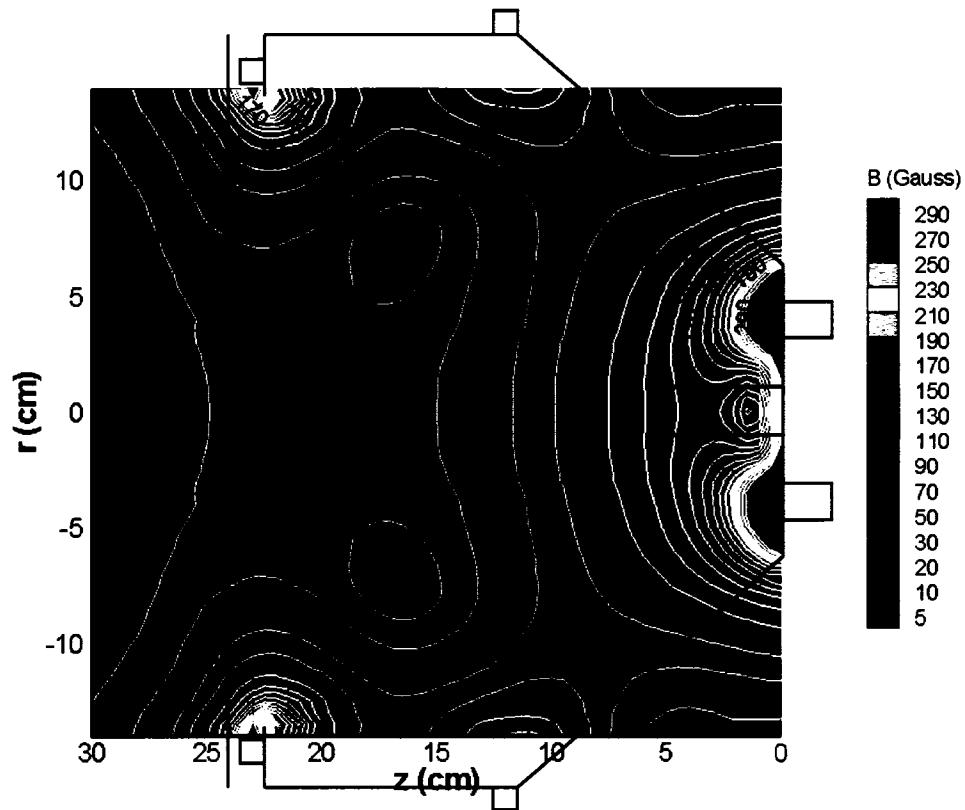

Figure 7.2 Constant magnitude magnetic field lines inside the prototype NSTAR discharge chamber. Contours of magnetic field strength 290 Gauss and above are colored red.

118
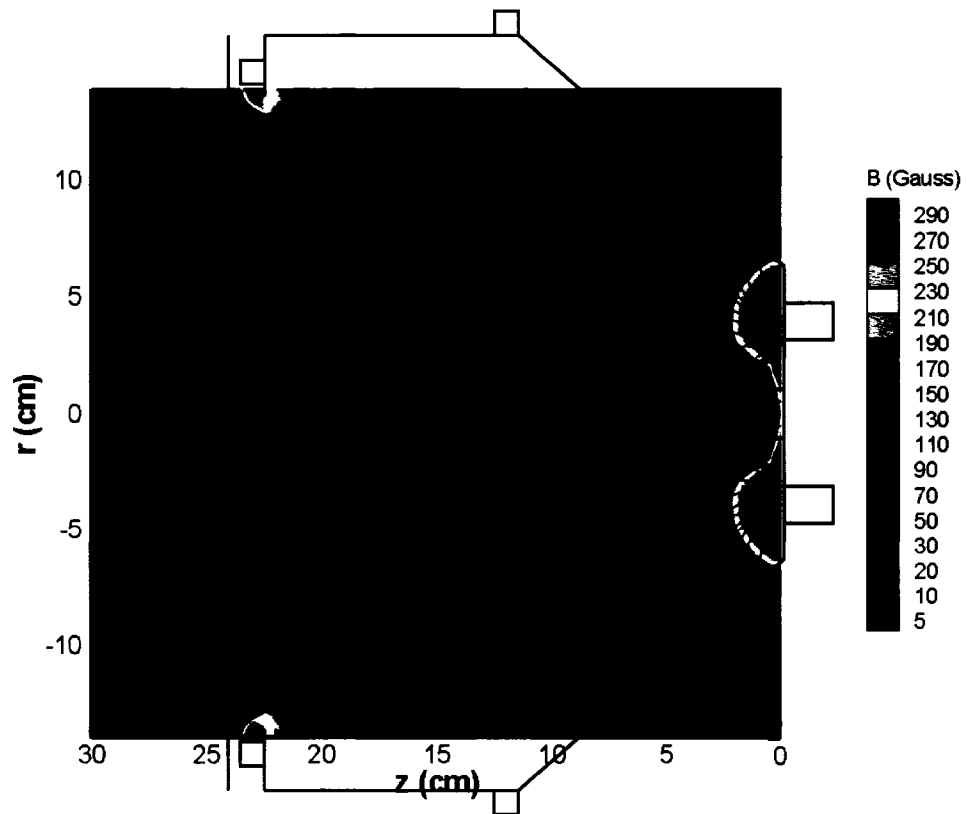
Figure 7.3 Selected magnetic field lines inside the prototype NSTAR discharge chamber. Contours of magnetic field strength 290 Gauss and above are colored red.

119

8 Appendix B – Electrostatic Analyzer (ESA) Equations

The Comstock model AC-901 electrostatic analyzer (ESA) can be used to measure ion energies[39]. The ESA consists of two spherical sector plates fabricated in a 160° arc, as shown in Figure 8.1. At each end of the arc, the ESA has a collimator to limit the field of view of the device. Both collimators are comprised of a set of two disks with 2 mm holes aligned with each other and separated by 1 cm to allow for very narrow solid angle acceptance of ions moving toward the detector. The collector electrode is located downstream of the exit collimator.
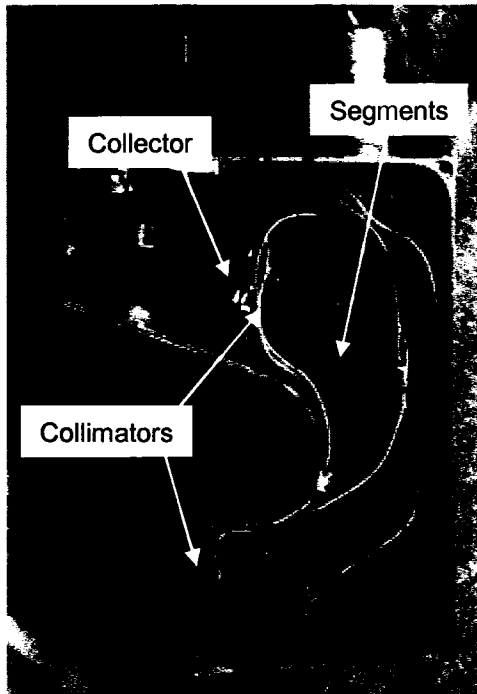


Figure 8.1a Picture of the ESA with the top cover removed.
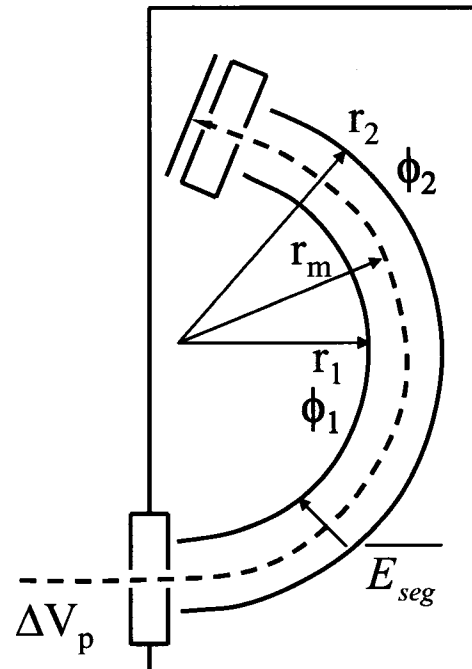
Figure 8.1b Diagram of the ESA.

120

8.1 Governing Equations

The electrostatic analyzer is designed to separate ions according to their energy to charge ratio (E/z). This is done by applying voltage biases to the two spherical segments so that the ions feel an electrostatic force according to Eq. 8.1:

$$\overline{F} = z \cdot q \cdot \left| \overline{E}_{seg} \right|$$

Eq. 8.1

Where F is the force, z is the charge state, q is the electronic charge, and E_{seg} is the electric field in the center of the two spherical segments. The bias on the outer segment, ϕ_2, is more positive than the bias on the inner segment, ϕ_1, for ion measurement. For an ion to properly pass through the ESA to the collector plate, the ion must feel a force so that the path is a circle with a circumference r_m:

$$\overline{F} = \frac{m \cdot \overline{v}^2}{r_m}$$

Eq. 8.2

Where m is the mass of the ion, v is the velocity of the ion, and r_m is the mean radius of the segments. These forces must be nearly equal for the ion to pass through the ESA to the collector plate:

$$z \cdot q \cdot \left| \overline{E}_{seg} \right| = \frac{m \cdot v^2}{r_m}$$

Eq. 8.3

If the ion velocity is too low, the ion will drift toward the inner segment and not pass through to the collector. On the other hand, if the ion velocity is too high, the ion will drift toward the outer segment and not pass through to the collector.

121

The velocity of the ion entering the ESA (neglecting initial thermal velocities), can be described in terms of ion energy by Eq. 8.4:

$$E = z \cdot q \cdot \Delta V_p = \frac{1}{2} \cdot m \cdot v^2 \quad \text{or} \quad v = \sqrt{\frac{2 \cdot z \cdot q \cdot \Delta V_p}{m}} \qquad \text{Eq. 8.4}$$

Where E is the ion energy and ΔV_p is the potential difference between the ion creation point in the plasma and the entrance collimator of the ESA.

The electric field, E_{seg}, can be described by Eq. 8.5:

$$\overline{E}_{seg} = -\nabla \phi = -\frac{\partial \phi}{\partial r} \hat{r} \qquad \text{Eq. 8.5}$$

From the Laplacian in spherical coordinates (only r direction variation):

$$\frac{1}{r^2} \cdot \frac{d}{dr}\left(r^2 \cdot \frac{d\phi}{dr}\right) = 0 \quad \text{or} \quad \frac{\partial \phi}{\partial r} = \frac{C}{r^2} \qquad \text{Eq. 8.6}$$

Integrating this equation from r_1 to r_2 yields the constant, C:

$$\Delta \phi = \phi_2 - \phi_1 = C \cdot \left(\frac{1}{r_1} - \frac{1}{r_2}\right) \quad \text{or} \quad C = \frac{\Delta \phi}{\left(\frac{1}{r_1} - \frac{1}{r_2}\right)} \qquad \text{Eq. 8.7}$$

Now, the equation for the electric field in spherical coordinates is:

$$\overline{E}_{seg} = -\frac{C}{r_m^2} = \frac{-\Delta \phi}{r_m^2 \cdot \left(\frac{1}{r_1} - \frac{1}{r_2}\right)} \qquad \text{Eq. 8.8}$$

Substituting Eq. 8.8 for the electric field and Eq. 8.4 for the velocity of the ion in terms of energy into the force balance equation, Eq. 8.3, yields:

$$z \cdot q \cdot \frac{\Delta \phi}{r_m^2 \cdot \left(\frac{1}{r_1} - \frac{1}{r_2}\right)} = \frac{m}{r_m} \cdot \left(\sqrt{\frac{2 \cdot z \cdot q \cdot \Delta V_p}{m}}\right)^2 \qquad \text{Eq. 8.9}$$

122

Then, solving Eq. 8.9 for ΔV_p gives the relation:

$$\Delta V_p = \frac{\Delta \phi}{\frac{r_2}{r_1} - \frac{r_1}{r_2}} = 2.254 \cdot \Delta \phi \qquad \text{Eq. 8.10}$$

Where the value 2.254 comes from the radius values $r_1 = 3.25$ cm and $r_2 = 4.05$ cm for the Comstock model AC-901 ESA.

It is important to note that the charge state, z, and mass, m, cancel out of the equations. This means that the ESA does not differentiate between different ion species. Also, the ESA detects only the energy to charge ratio, E/z, so a singly charged ion and a doubly charged ion going through a potential ΔV_p will be measured at the same $\Delta \phi$. This can be seen by rearranging the force balance equation. The electric field necessary to measure a singly charged ion (z = 1) is given by:

$$\overline{E}_s = \frac{m \cdot v_s^{\,2}}{z \cdot q \cdot r_m} = \frac{m \cdot v_s^{\,2}}{q \cdot r_m} \qquad \text{Eq. 8.11}$$

Where v_s is the velocity of a singly charged ion going through a potential ΔV_p. The equation for the doubly charged ion is similar to the singly charged ion except for the charge state (z = 2) and velocity. The velocity of the doubly charged ion is:

$$v_d = \sqrt{\frac{2 \cdot z \cdot q \cdot \Delta V_p}{m}} = \sqrt{z} \cdot v_s = \sqrt{2} \cdot v_s \qquad \text{Eq. 8.12}$$

Then, the electric field necessary to measure a doubly charged ion is:

$$\overline{E}_d = \frac{m \cdot v_d^{\,2}}{z \cdot q \cdot r_m} = \frac{m \cdot (\sqrt{2} \cdot v_s)^2}{2 \cdot q \cdot r_m} = \overline{E}_s \qquad \text{Eq. 8.13}$$

This shows that the ESA will measure the energy to charge ratio, E/z, instead of the ion energy, E, for ions coming from a plasma through a potential difference ΔV_p.

123

8.2 Constant Transmission Mode and Variable Transmission Mode

In the constant transmission mode (Figure 8.2), a constant ΔV is applied to the segments and the entrance and exit collimators are swept with respect to the plasma to yield the ion energy distribution function (IEDF). This is generally the preferred method in which to operate rather than the variable transmission mode. In the variable transmission mode (or sector field sweep mode, Figure 8.3), the entrance and exit collimators are biased to a constant value (usually ground) and the spherical segment potentials are swept to obtain the ion energy distribution function.
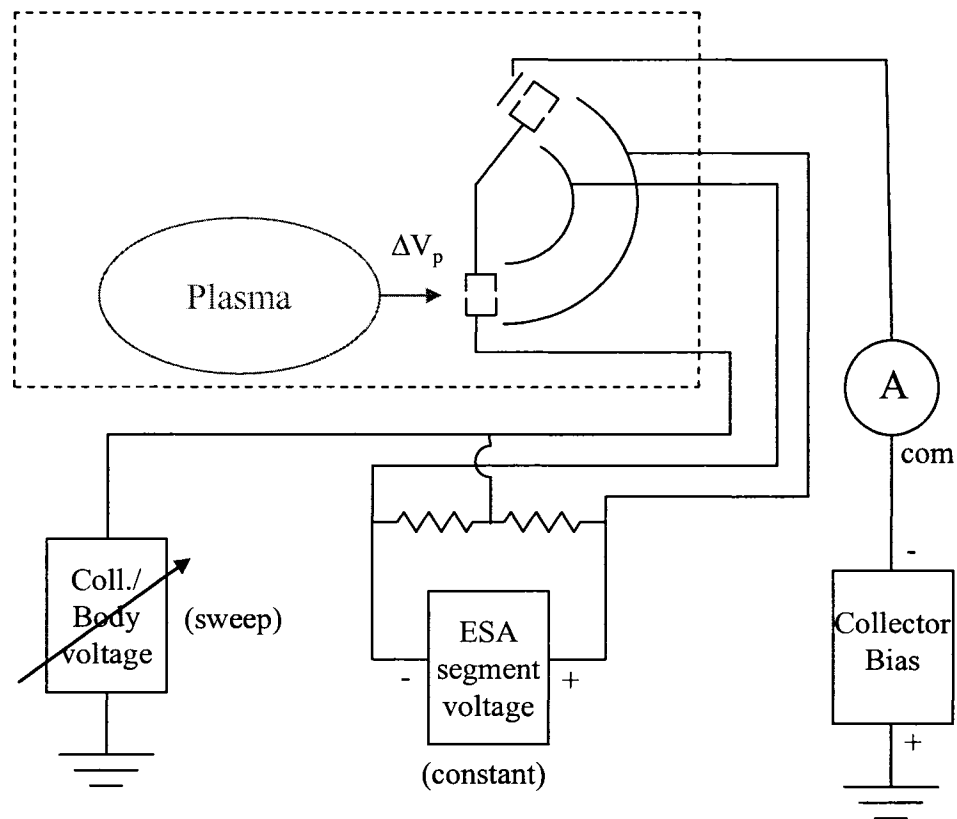

Figure 8.2   ESA bias setup for the constant transmission energy mode. The voltage difference between the segments is held constant while the collimator voltage is swept to obtain the ion energy distribution function.

124
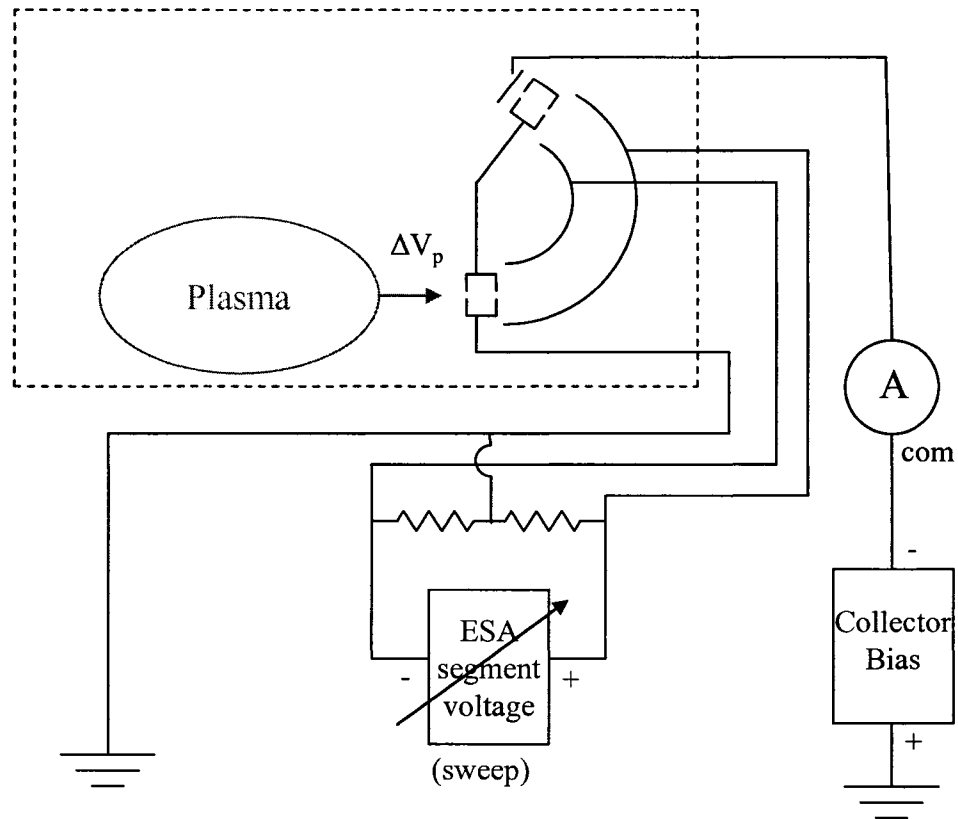
Figure 8.3 ESA bias setup for the variable transmission energy mode. The voltage difference between the segments is swept while the collimator voltage is held constant (typically ground).

The reason the constant transmission mode is preferred is that the energy spread, ΔE, of ions that are able to pass through the ESA is constant. While selecting for an energy, E (actually E/z), the actual ion energies that are able to pass through the ESA is E +/- $\Delta E/2$. The ΔE is determined from the $\Delta \phi$ applied to the spherical segments as well as the collimation geometry of the probe. One equation for the energy spread through the ESA is given by Eq. 8.14[39]:

$$\Delta E_{FWHM} = \frac{\omega}{(R \cdot (1 - \cos \Phi) + \delta \cdot \sin \Phi)} \cdot E \qquad \text{Eq. 8.14}$$

Where ΔE_{FWHM} is the energy full width at one-half maximum, E is the pass energy of the ions, ω is the aperture size (~ 0.2 cm), Φ is the angle range of the ESA (160 degrees), R

125

is the mean sphere radius (3.6 cm), and δ is the separation distance from the segments to the exit collimator (1.07 cm). Since the geometry of the ESA is constant, a larger segment bias, $\Delta\phi$, results in a larger pass energy, E, and therefore a larger energy spread of ions, ΔE, can pass through the segments to the collector plate.

In the constant transmission mode, the segment bias difference, $\Delta\phi$, (and therefore ΔE) is held constant. So the ion current magnitude measured at a particular energy is directly comparable to the ion current magnitude measured at a different energy.

On the other hand, in the variable transmission mode, $\Delta\phi$ is varied to measure the ion energy distribution function. This means that the accepted energy spread varies and ion current magnitudes to the probe will not be comparable unless a correction is applied. Ions with higher energies will appear to have larger current magnitudes as a result of the larger energy acceptance range relative to the desired target energy.

Figure 8.4 shows the effect of using the variable transmission mode instead of the preferred constant transmission mode. The ESA was positioned to look at a prototype NSTAR discharge chamber at a 90 degree angle relative to the cathode centerline. The traces have been normalized to the peak value in the distribution. The trace taken in the constant transmission mode shows an energetic tail extending from the main ion group whereas the trace taken in the variable transmission mode shows a large group in the 30 to 60 eV energy range. The ion current magnitudes from the variable transmission mode are misleading and should be corrected so that ions of different energies are directly comparable. Or, the same mode of operation and applied voltage biases should be used if comparisons are to be made between measured distribution functions.

126

Condition 2b
Prototype NSTAR chamber
$J_D = 8.3$ A
$V_D = 24.9$ V
6.1 sccm Xe
Angle = 90°
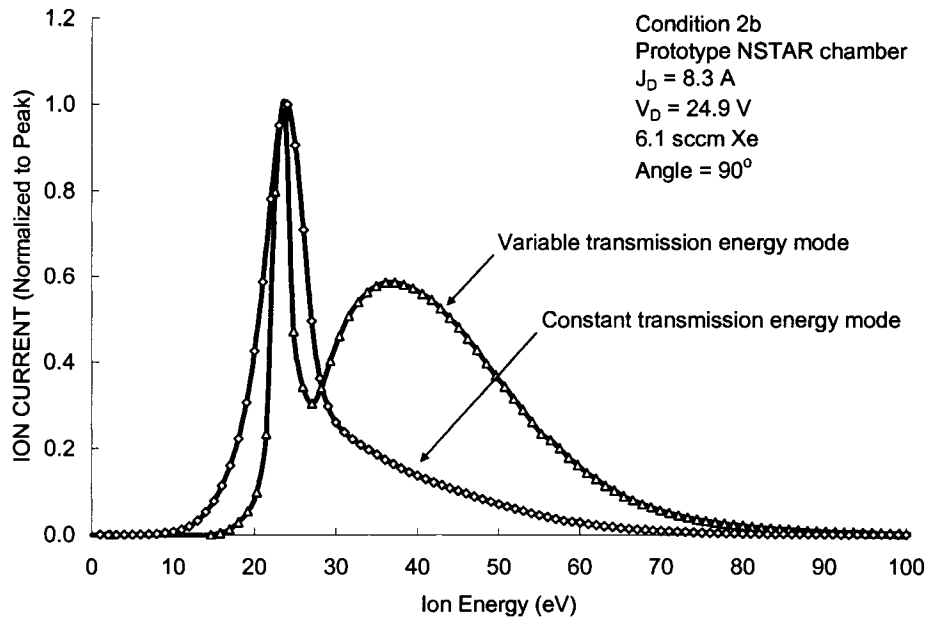
Figure 8.4 ESA measurements using the constant and variable transmission modes. Note how ion current magnitudes can be directly compared to ions of different energies in the constant transmission mode but not in the variable transmission mode.

The effects of the different transmission modes can also be seen by using a program called SIMION 3D 7.0^{40}. This program allows the user to input virtual models to investigate how ions are affected by electrode potentials and magnetic poles. The geometry of the ESA was input into the program as shown in Figure 8.5.

Figure 8.5a The ESA geometry in SIMION 3D 7.0. Electrode potentials are applied to simulate the electric fields seen by the ions.
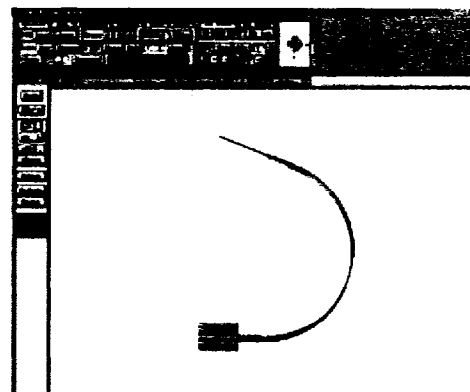
Figure 8.5b Top view of the ESA in the SIMION program. The black lines are ions that are "flown" through the probe to investigate the ESA operation.

127

Figure 8.6 shows results from the SIMION 3D 7.0 modeling. The plot shows the spread of ion energies that were able to pass through the ESA to the collector versus the segment potential difference. As expected, the energy spread of ions that were able to pass through the segments increased as the segment potential difference was increased. In practice, it is desirable to be able to compare ion current magnitudes for different energy ions. This is the case for the constant transmission mode but not the case for the variable transmission mode. However, since the energy acceptance range changes uniformly with $\Delta\phi$ in the variable transmission mode, it may be possible to apply a correction to the data in order to better compare ion current magnitudes at different energies.
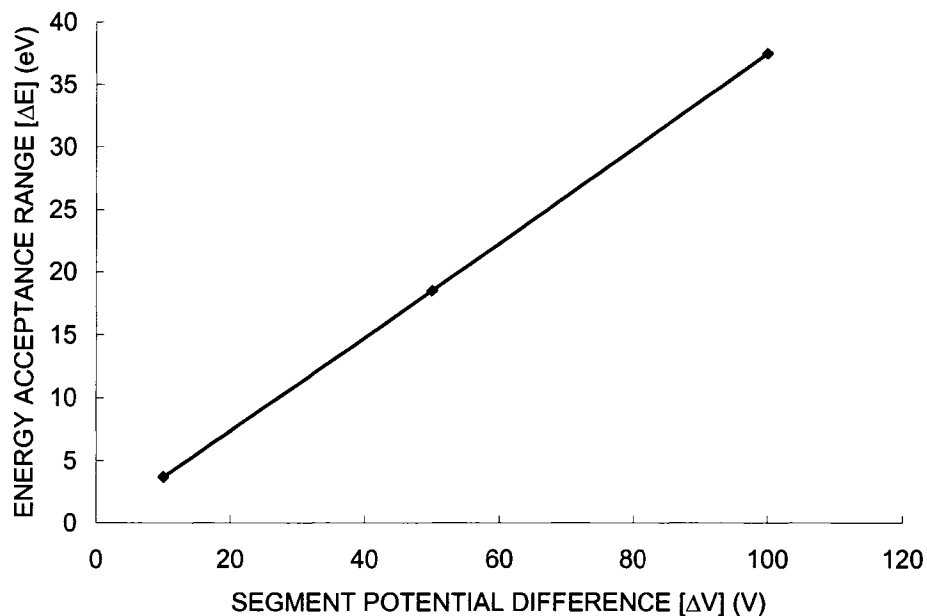
Figure 8.6 ESA modeling results from SIMION 3D 7.0. The energy spread of ions that were able to pass through the segments to the collector increased as the segment potential difference was increased.

128

9 Appendix C – ExB Probe Equations

The ExB probe (or Wein filter) has the ability to measure the charge state of ions due to the use of magnetic fields in addition to electric fields[41,42]. The ExB probe schematic is shown in Figure 9.1.
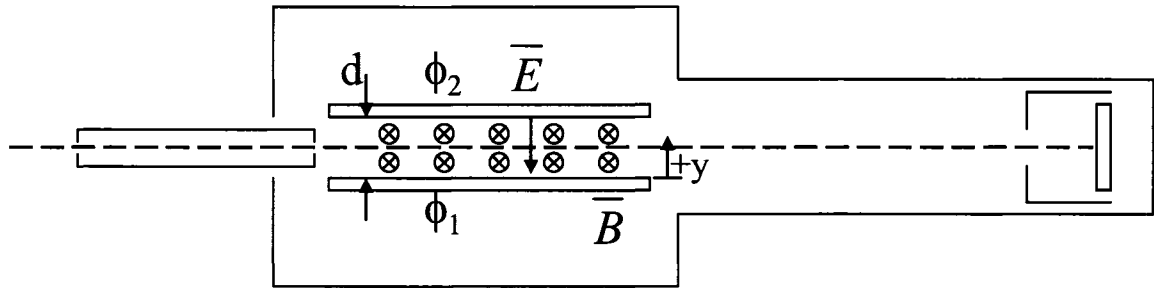

Figure 9.1 ExB probe schematic showing the electric field and magnetic field separation section. The amount of direction change the ion undergoes depends on its entrance energy and the applied electric and magnetic field strengths.

Ions that are able to pass through the entrance collimator will then enter a separation region where they feel a force from both electric and magnetic fields according to the Lorentz force equation:

$$\overline{F} = q \cdot (\overline{E} + \overline{v} \times \overline{B}) \qquad \text{Eq. 9.1}$$

Where F is the force on the ion, q is the electronic charge, E is the electric field strength, v is the ion velocity, and B is the magnetic field strength. In order to pass through the probe to the collector plate, the net force on the ions must be near zero so that the ions are not pushed off the drift axis. Setting the force equal to zero and rearranging Eq. 9.1 yields:

$$\overline{E} = -\overline{v} \times \overline{B} \qquad \text{Eq. 9.2}$$

129

The equation for the ion velocity entering the ExB probe is given by Eq. 9.3 (neglecting

initial thermal velocities):

$$v = \sqrt{\frac{2 \cdot z \cdot q \cdot \Delta V_p}{m}}$$

Eq. 9.3

Where ΔV_p is the potential difference between the ion creation point in the plasma and

the entrance collimator of the ExB and m is the mass of the ion species. The equation for

the electric field comes from the Laplacian in Cartesian coordinates (y direction only,

symmetry in x and z directions):

$$\frac{\partial^2 \phi}{\partial y^2} = 0 \qquad \text{or} \qquad \frac{\partial \phi}{\partial y} = C$$

Eq. 9.4

Integrating this equation from y equals 0 to d gives:

$$C = \frac{\phi_2 - \phi_1}{d} = \frac{\Delta \phi}{d}$$

Eq. 9.5

Where ϕ_2 and ϕ_1 are the plate voltages and d is the distance between the plates.

Then, the electric field is simply:

$$\overline{E} = -\nabla \phi = -\frac{\partial \phi}{\partial y} = -C = -\frac{\Delta \phi}{d}$$

Eq. 9.6

Now, the velocity equation (Eq. 9.3) and electric field equation (Eq. 9.6) can be

substituted into the force balance equation (Eq. 9.2). The resulting equation for the ions

that are measured by the probe is:

$$\Delta V_P = \frac{m \cdot \Delta \phi^2}{2 \cdot z \cdot q \cdot d^2 \cdot B^2}$$

Eq. 9.7

Where ΔV_p is the potential difference between the ion creation point in the plasma and

the entrance collimator of the ExB in V, m is the mass of the ion species in kg, $\Delta \phi$ is the

130

voltage difference between the plates in V, z is the charge of the ion (1, 2, etc), q is the electronic charge in Coulombs, d is the separation distance between the plates in meters, and B is the magnetic field strength in Gauss.

When taking measurements, the plate voltage difference, $\Delta\phi$, is swept while the plate separation distance and the magnetic field are held constant. The magnetic field, B, is produced using a permanent magnet. Each ion will be separated according to the mass, m, charge state, z, and the potential difference between the ion creation point in the plasma and the entrance collimator of the ExB, ΔV_p.

131